SESSION III

WORKSHOP ON MATERIALS ISSUES IN LOW-EMISSION BOILERS AND HIGH EFFICIENCY COAL-FIRED CYCLES

SUMMARY OF WORKSHOP ON MATERIALS ISSUES IN LOW EMISSION BOILERS AND HIGH EFFICIENCY COAL-FIRED CYCLES

The agenda for the workshop is included in Appendix A. The purpose of the workshop was to review with experts in the field the materials issues associated with two of the primary coal power systems being developed by the DOE Office of Fossil Energy. The DOE-FE Advanced Power Systems Program includes natural gas-based and coal-based power systems. Major activities in the natural gas-based power systems area include the Advanced Turbine Systems (ATS) Program, the Fuel Cells Program, and Hybrid Cycles. The coal-based power systems projects include the Low Emissions Boiler Systems (LEBS) Program, the High-Performance Power Systems Program (HIPPS), the Integrated (Coal) Gasification Combined-Cycle Program, and the Fluidized-Bed Combustion Program. This workshop focused on the materials issues associated with the LEBS and HIPPS technologies.

The workshop was organized around presentations by DOE sponsor representatives and LEBS and HIPPS contractor representatives. The three LEBS contractors, ABB Combustion Engineering, Babcock & Wilcox (B&W), and D. B. Riley, and the two HIPPS contractors, United Technologies Research Center (UTRC) and Foster Wheeler, were represented in the workshop through presentations by personnel from the respective companies. In addition, representatives of organizations providing support to these companies in addressing materials challenges for the LEBS and HIPPS systems also made presentations. These presentations provided the stimulus for discussions on the materials issues and in establishing the direction for future activities on the AR&TD Materials Program.

The objectives of the LEBS Program are to develop, by 2000, systems that will achieve 42-45 percent net efficiencies (HHV basis) in power generation with significantly reduced emissions and costs compared to current pulverized coal-fired plants that meet New Source Performance Standards (NSPS). The LEBS Program includes three different design concepts developed by the three contractors. ABB Combustion Engineering is pursuing the Kalina cycle. This cycles uses an ammonia-water working fluid that has an extended boiling range and permits more efficient heat transfer than occurs with a single working fluid, such as water. Both B&W and D. B. Riley have adopted supercritical steam (Rankine) cycles with double reheat, operating at a steam pressure of 31.5 MPa (4500 psi) and main and reheat temperatures of 593°C (1100°F). Low-NO_x burners will be used in all of these plants.

There appeared to be consensus among the workshop participants that the critical components of the LEBS systems, particularly for the B&W and D. B. Riley concepts, included superheater tubing and headers, and high- and low- pressure reheater tubing and headers. The production of steam at 1100°F can result in metal wall temperatures of 1200°F. Critical piping in these systems are the main steam piping with an internal diameter of ten inches and wall thickness of 2 to 3 inches, high pressure reheat piping with an internal diameter of 20 inches and wall thickness of 1 to 2 inches, and low pressure reheat piping with an internal diameter of 30 inches and a wall thickness up to 1 inch. Performance criteria of the materials for these system elements are ASME certification by 2000, sufficient allowable stresses at design temperatures, that they be fabricable and manufacturable, provide a lifetime (mechanical properties, primarily creep, and corrosion resistance) of at least 20 years, and that they be available at competitive prices. The use of low-NO_x burners may result in the need for additional corrosion protection because the substoichiometric oxygen environments obtained near waterwalls has resulted in sulfidation attack not usually associated with combustion units.

The major materials issues include furnace wall sulfidation, fatigue and cracking, and superheater and reheater fuel ash corrosion. The use of new alloys will require demonstration of their long-term metallurgical stability and fabricability. There are, of course, numerous considerations in the determination and selection of the materials to use in these high-performance plants. It appears possible to build and meet the required performance criteria of these LEBS systems with commercially available materials. However, these systems have operating conditions that push the limits of performance of available materials and improvements in conventional alloys and development of new alloys are needed. A general conclusion of the workshop was that high-strength ferritic steels should be exploited to the maximum extent possible to take advantage of their performance characteristics, fabricability and availability, and attractive costs. The continued development of low-cost superalloys is appropriate. Improvements in corrosion (primarily fire-side) resistance continues to be a need. If sufficient data are developed to meet the engineering design requirements and to build needed confidence in them, oxide-dispersion-strengthened (ODS) ferritic alloys could have a major impact on future supercritical plant construction.

Based on the deliberations of the participants in this workshop, the AR&TD Materials Program appears to be properly focused on the most important of materials issues associated with advanced coal-fired power generation systems such as LEBS. The Program activities include work on advanced ferritic and austenitic steels, fire-side corrosion in coal-fired power generation plants, and the development of ODS alloys. The Program has had ongoing for several years the development of advanced austenitic alloys that will meet the performance criteria of even more advanced plants operating at 1200°F and 5000 psi steam conditions. Based on data obtained to date, the ORNL-developed iron aluminide alloys appear to be quite capable of providing the required corrosion resistance in low-NO_x burner systems. These alloys may be used as protective surfaces, which can be applied by a variety of conventional coating techniques.

The objectives of the HIPPS Program are to develop, by 2006, a coal-based power generation system that will achieve superior emissions performance at efficiencies of 50 percent or greater and to provide electricity at a cost of at least 10 percent less that current coal-fired plants that meet New Source Performance Standards (NSPS). The HIPPS plants are indirectly-fired (coal) units that use air as the working fluid for a gas turbine and employ a steam bottoming cycle to achieve maximum efficiency. Two contractor teams, the UTRC team and the Foster Wheeler team, are taking different approaches to the development of HIPPS. The UTRC plant integrates a gas-turbine cycle into a coal-fired plant by heating clean air in a high-temperature air furnace (HITAF). Natural gas firing may be required to heat the air to the requisite turbine inlet temperature. Foster Wheeler is developing an all-coal-fired HIPPS system. A pyrolyzer converts coal to fuel gas and char. The fuel gas is delivered to the gas turbine combustor and natural gas augmentation is not required. The char is burned in the HITAF.

The most critical of the materials challenges for HIPPS was clearly determined to be the ceramics for the air heater. Several materials are being evaluated for the application including sintered α-SiC (Carborundum's Hexoloy), sintered β-SiC (Coors), siliconized SiC (Saint Gobain/Norton), SiC particulate reinforced alumina (DuPont Lanxide), and SiC fiber-reinforced SiC (DuPont). Silicon-based ceramics generally have been favored because of their superior mechanical properties and superior heat transfer characteristics. Availability at reasonable cost and reliability are outstanding issues associated with all of the ceramic candidates. These high-temperature HIPPS plants will achieve temperatures that result in slag formation. The acidity or basicity of slags can be critical to degradation of ceramic materials. Generally, an acidic slag will be more aggressive toward basic ceramics and vice versa through an acid-base neutralization reaction. Also, formation of low-melting silicates, aluminosilicates, etc., can result in accelerated corrosion of silicon-based ceramics. A preferred, although usually not feasible, approach would be to select ceramics and coal types to ensure compatibility in the slagging environment. Numerous test activities are underway to identify the ceramic materials with the best combination of properties to minimize compromise in selection.

The AR&TD Materials Program focus on structural ceramic composites is for heat exchanger applications such as that required in the air heaters or air furnace for HIPPS. That work is directed toward continuous fiber reinforced SiC, which, as noted, is one of the prime candidates for HIPPS. The Program is comprehensive in addressing all issues associated with the use of SiC-based ceramics in these demanding applications, including fabrication/processing, mechanical properties, corrosion, nondestructive evaluation, and fracture mechanics.

SESSION IV

NEW ALLOYS

DEVELOPMENT OF ODS-Fe_3Al ALLOYS

I. G. Wright, B. A. Pint, P. F. Tortorelli, and C. G. McKamey

Oak Ridge National Laboratory
Oak Ridge, Tennessee, U.S.A.

SUMMARY

The overall goal of this program is to develop an oxide dispersion-strengthened (ODS) version of Fe_3Al that has sufficient creep strength and resistance to oxidation at temperatures in the range 1000 to 1200°C to be suitable for application as heat exchanger tubing in advanced power generation cycles. The main areas being addressed are: (a) alloy processing to achieve the desired alloy grain size and shape, and (b) optimization of the oxidation behavior to provide increased service life compared to semi-commercial ODS-FeCrAl alloys intended for the same applications. The recent studies have focused on mechanically-alloyed powder from a commercial alloy vendor. These starting alloy powders were very clean in terms of oxygen content compared to ORNL-produced powders, but contained similar levels of carbon picked up during the milling process. The specific environment used in milling the powder appears to exert a considerable influence on the post-consolidation recrystallization behavior of the alloy. A milling environment which produced powder particles having a high surface carbon content resulted in a consolidated alloy which readily recrystallized, whereas powder with a low surface carbon level after milling resulted in no recrystallization even at 1380°C. A feature of these alloys was the appearance of voids or porosity after the recrystallization anneal, as had been found with ORNL-produced alloys. Adjustment of the recrystallization parameters did not reveal any range of conditions where recrystallization could be accomplished without the formation of voids. Initial creep tests of specimens of the recrystallized alloys indicated a significant increase in creep strength compared to cast or wrought Fe_3Al, but the specimens failed prematurely by a mechanism that involved brittle fracture of one of the two grains in the test cross section, followed by ductile fracture of the remaining grain. The reasons for this behavior are not yet understood. The cyclic oxidation kinetics of ODS-Fe_3Al alloys made from commercially-produced powder indicated a decrease in the tendency for scale spallation at 1100 and 1200°C compared to equivalent ORNL-produced alloys. The overall oxidation rate at 1100°C in terms of total oxygen consumption as a function of time was essentially the same as for a semi-commercial ODS-FeCrAl alloy. Hence, this improvement indicates an increase in the oxidation-limited lifetime compared to both ODS-Fe_3Al alloys prepared at ORNL, and to the ODS-FeCrAl alloy.

INTRODUCTION

Interest in increasing the efficiency of coal-fired power plants has led to the examination of alternatives to the steam boiler-Rankine cycle systems, for which increases in efficiency have been limited by the slow progress in improving the ability to handle steam at temperatures much in excess of 565°C (1050°F). Indirect-firing of gas turbines in open or closed cycles is one approach to linking the higher efficiencies possible via the Brayton cycle with coal as the fuel. Current programs involving indirectly-fired gas turbine cycles are aimed at high cycle efficiencies, of the order of 47 percent based on the higher heating value (HHV) of the fuel, and involve open cycle systems in which air is heated to 760°C (1400°F) in a metallic heat exchanger, followed by further heating to 982°C (1800°F) in a natural gas-fired ceramic heat exchanger [1-3]. A variant of this approach is where part of the coal is pyrolyzed to produce the fuel gas used to fire the final heat exchanger or the turbine; in that case the air entering the turbine is heated to 1288°C (2350°F).

Successful implementation of indirectly-fired cycle technologies will require the development of a durable coal-fired heat exchanger capable of heating the working fluid to very high temperatures, in addition to adapting a gas turbine for this particular duty. The ferritic ODS alloys based on Fe-Cr-Al have the potential for application at higher temperatures than the modified conventionally-strengthened alloys in which the strengthening mechanisms degrade as the precipitated phases become less stable with increasing temperature. Oxide dispersion-strengthened alloys can provide creep strength up to approximately 90 percent of the alloy melting temperature (which is ≈1480°C for FeCrAls). A heat exchanger of harp design, made from 4 m long, 2.5 cm diam. ODS-FeCrAl tubes, was recently shown to be capable of heating air to 1100°C in a closed-cycle demonstration plant [4]. Compared to ODS-FeCrAl alloys, ODS-Fe_3Al has potential advantages of lower cost, lower density, and superior oxidation and sulfidation resistance, provided that similar gains in creep strength can be realized through the ODS process.

ALLOY PREPARATION

Yttria-containing Fe_3Al alloy powder was prepared by the PM-ODS Werkstoffe division of Metallwerk Plansee (PM), using high-energy ball milling, from prealloyed Fe_3Al powder made by argon-atomization by Homogeneous Metals (HM). The chemical analysis of the starting powder is shown in Table 1; it was spherical in shape, and had a mean particle size of 75 μm (range 30 to 200 μm). The milling parameters used by PM were based on those used in the commercial production of its PM2000 alloy (Y_2O_3-dispersion-strengthened FeCrAl). The main difference was that three different milling environments (cover gas plus process control agents [PCAs]) were employed (Routes A, B, and C in Table 1). After milling, the powder particle size ranged up to 480 μm for powder from Route C, whereas the use of PCAs resulted in smaller powder particle sizes with, for instance, the powder from Route A having a maximum particle size of 200 μm.

The bulk chemical analyses of the milled powders, shown in Table 1, indicate that the powder processed by Route C had picked up a significantly lower level of oxygen than had the other two powders. In contrast, the Route A powder exhibited significantly higher levels of nitrogen, carbon, and hydrogen than the other powders. The pickup of nitrogen, hydrogen and carbon was similar for the powders from Routes B and C, with the Route C powder showing slightly lower levels.

Table 1. Chemical Analyses of Fe_3Al Powders (wt %)

Element	As-Received		Route A	Route B	Route C
	HM	PM			
Fe	Bal.	79.6			
Al	16.3	18.20 (Bal.)			
Cr	2.4	2.18			
Zr	20 ppm	26 ppm			
O (total)	60 ppm	110 ppm	1,800 ppm	1,900 ppm	1,400 ppm
O (from Y_2O_3)			1,025 ppm	1,053 ppm	1,080 ppm
O bal.			775 ppm	847 ppm	320 ppm
O pickup			*665 ppm*	*737 ppm*	*210 ppm*
N	18 ppm	7 ppm	1,264 ppm	145 ppm	88 ppm
N pickup			*1257 ppm*	*138 ppm*	*81 ppm*
H		16 ppm	115 ppm	40 ppm	29 ppm
C		24 ppm	667 ppm	360 ppm	303 ppm
C pickup			*643 ppm*	*336 ppm*	*279 ppm*
O/Al			*0.010*	*0.010*	*0.008*
Fe/Al			*4.37*	*4.37*	*4.37*
C/Fe			*0.009*	*0.0005*	*0.0004*
C/Al			*0.004*	*0.002*	*0.002*
C/O			*0.37*	*0.19*	*0.22*

Auger analysis of the surfaces of the as-milled powders indicated that the main difference was the carbon content. As shown in Table 2, the C/Fe, C/Al, and C/O ratios were greatest for powder milled by Route B. Comparison with the bulk analyses in Table 1 suggests that the powder particle surfaces were enriched in aluminum oxide and carbon. The presence of the surface oxide was expected; the surface carbon enrichment is presumed to result largely from interaction of the powder particles with the ball surfaces during milling.

Samples of each powder were canned in mild steel, hot degassed, and consolidated into bar by extrusion (9:1 ratio) at 1050°C following preheating for 45 min. The flow stresses measured during extrusion ranged from 810 to 850 Pa. After extrusion, all the samples exhibited a submicron size grain structure. The microhardness values (HV10) for these structures were 486, 413, and 399 kg/mm^2, for powder A, B, and C, respectively. The chemical compositions of the consolidated alloys are shown in Table 3. Compared to the composition of the starting powder, some loss of aluminum is evident, with the greatest loss observed for Powder A (PMWY-1) which also showed the largest pickup of oxygen. The oxygen levels in PMWY-2 and -3 remained essentially the same as in the as-milled powders, but PMWY-2 showed an increase in nitrogen content after consolidation of the order of 900 wppm. The carbon levels of all three alloys were essentially unchanged after consolidation.

Table 2. Auger Analyses of As-Milled Powders

Sample	Auger Analysis (%)				Relative Counts				
	C	O	Fe	Al	O/Al	Fe/Al	C/Fe	C/Al	C/O
A1	7.8	35.7	31.47	25.03	7.13	1.58	0.23	0.36	0.05
A2	9.11	36.11	31.17	23.61	7.65	1.66	0.27	0.44	0.06
B1	19.2	29.64	30.3	20.87	7.10	1.83	0.58	1.05	0.15
B2	21.2	31.49	28.19	19.1	8.25	1.86	0.68	1.27	0.15
C1	14.5	32.99	29.04	23.49	7.02	1.55	0.45	0.70	0.10
C2	12.4	31.73	29.86	26.04	6.09	1.44	0.38	0.54	0.09

RECRYSTALLIZATION

The initial attempt to recrystallize the consolidated alloys used the same conditions as for PM2000, which involved annealing at 1380°C for 1 hr. Two of the alloys, PMWY-1 and 2, exhibited a very large, elongated grain structure, whereas alloy PMWY-3 showed no signs of recrystallization. The recrystallized alloys also exhibited a significant amount of porosity which appeared to be associated with the recrystallization anneal, since the as-extruded alloys were pore-free, as was alloy PMWY-3 after the anneal.

Porosity similar to that observed in the alloys PMWY-1 and -2 has been observed in other ODS alloys [5-7]. The extent and size of the pores apparently depends not only on powder processing parameters, but also varies among alloys processed by the same route [8]. The source of the porosity has been attributed to gas bubbles resulting from argon adsorbed on the original powder particles, but pores were still found when hydrogen was used as the cover gas during the milling step [5]. One model discounts the effects of gas from dissolved or bonded oxygen and carbon or nitrogen, and suggests a more likely cause is void condensation from stress-induced vacancy migration, with oxide shell growth around the pore walls by reduction of entrapped water vapor by the oxygen-active elements in the alloy [6]. Another model suggests that the voids result from plastic deformation by hydrogen liberated by the reduction of adsorbed water vapor (or hydroxides) on the original powder particle surfaces [7]. The source of the adsorbed gas is the original gas atomization process and/or the milling process; the relative importance of these sources is unclear.

Based on reported observations that such porosity in ODS alloys is usually absent or is smaller at lower temperatures [7], samples of the alloys were annealed at various combinations of

Table 3. Chemical Compositions of Extruded Alloys (wt %)

Element	PMWY-1 (Powder A)	PMWY-2 (Powder B)	PMWY-3 (Powder C)
Fe	81.68	81.45	81.54
Al	14.67	15.36	15.43
Cr	2.61	2.33	2.33
Y	0.38	0.39	0.40
Zr	<100 ppm	<100 ppm	<100 ppm
O (total)	3,232 ppm	2,073 ppm	1,452 ppm
O (Y_2O_3)	1,025 ppm	1,053 ppm	1,080 ppm
O bal.	2,207 ppm	1,020 ppm	372 ppm
Overall O pickup	*2,097 ppm*	*910 ppm*	*262 ppm*
N	968 ppm	1,024 ppm	44 ppm
C	600 ppm	400 ppm	300 ppm
B	<3 ppm	<3 ppm	<3 ppm
Cu	0.01	0.01	0.01
Mn	0.04	0.03	0.02
Ni	0.05	0.03	0.03
P	0.008	0.008	0.008
Si	0.04	0.03	0.04
Ti	0.01	<0.01	<0.01
Y	0.38	0.39	0.40
(Y_2O_3	0.48	0.50	0.51)
S	22 ppm	20 ppm	16 ppm

temperature and time to observe the recrystallization behavior and tendency to develop porosity. As mentioned above, Alloy PMWY-3 did not recrystallize under any of treatments used (up to 1hr at 1380°C). Alloy PMWY-2 did not recrystallize below 1200°C, and Alloy PMWY-1 did not recrystallize below 1300°C; the fine-grained microstructure of Alloy PMWY-1after annealing at 1300°C for 2 hr. is shown in Fig. 1. The microstructures of Alloy PMWY-2 after annealing for 2 hr at 1200, 1250, and 1300°C are illustrated in Figs. 2-4 and show that, while recrystallization is essentially complete after 2 hr at 1200°C, small areas of what appeared to be unrecrystallized grains persisted, even at 1300°C. These areas appeared as elongated dark-colored streaks in longitudinal cross sections (Fig. 2a), and as dark patches in transverse sections (Fig. 2b). With increasing temperature, the number and size of these areas tended to decrease, although one or two patches were still visible in typical transverse sections after 2 hr at 1300°C (Fig. 4b). Also evident in Figs. 2-4, especially in transveres sections, is the porosity that developed upon annealing, and which increased with increasing time and temperature.

The hardness of the alloys decreased on the order of 75-100 kg/mm^2 following the recrystallization anneal, and progressively decreased with increasing annealing temperature and time.

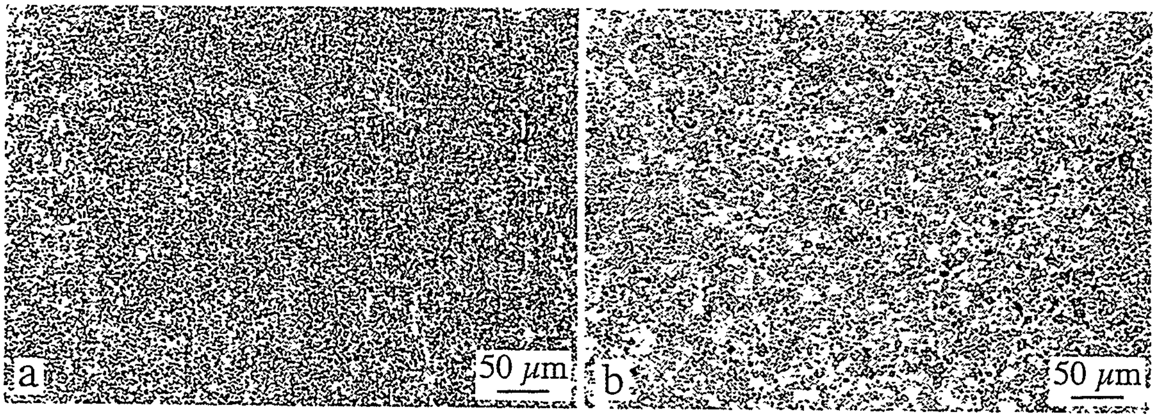

Fig. 1. Cross sections of Alloy PMWY-1 showing essentially no recrystallization after annealing for 2 hr at 1300°C: (a) longitudinal section, (b) transverse section.

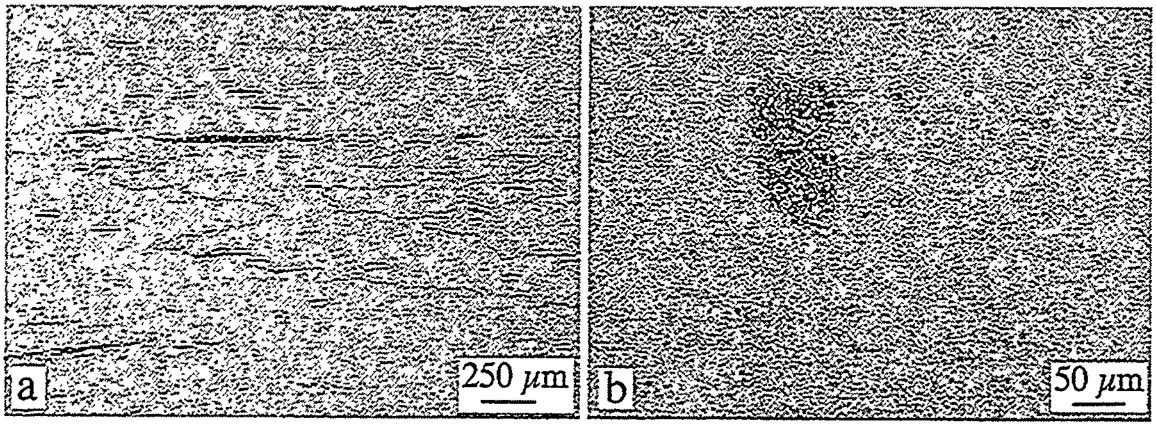

Fig. 2. Cross sections of Alloy PMWY-2 after annealing for 2 hr at 1200°C: (a) longitudinal, (b) transverse.

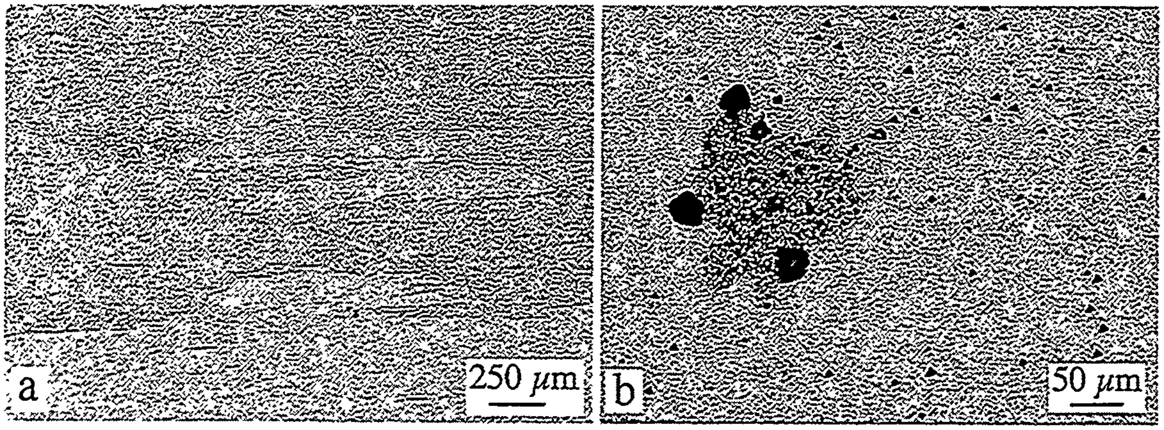

Fig. 3. Cross sections of Alloy PMWY-2 after annealing for 2 hr at 1250°C: (a) longitudinal, (b) transverse.

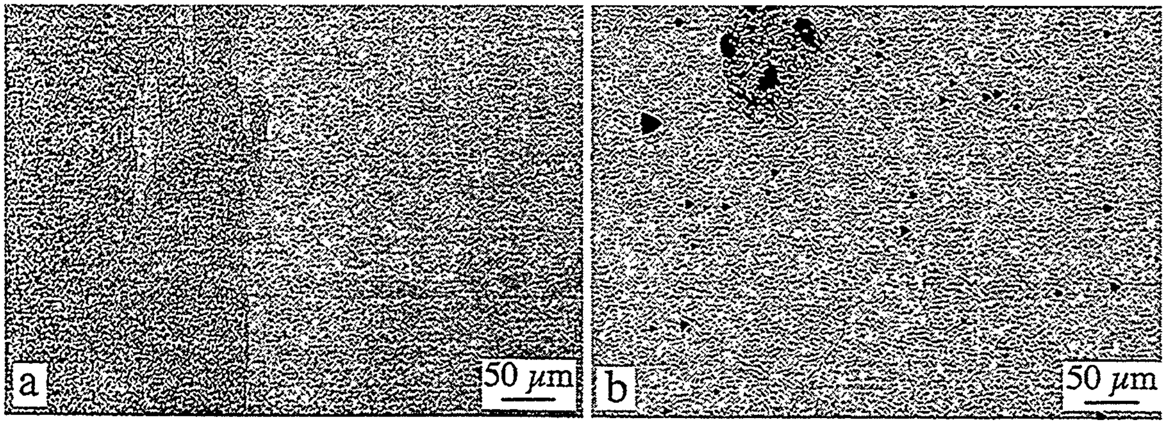

Fig. 4. Cross sections of Alloy PMWY-2 after annealing for 2 hr at 1300°C: (a) longitudinal, (b) transverse.

CREEP TESTS

Round creep-rupture specimens with a gage diameter of approximately 3 mm and a gage length of 17.8 mm were machined from bars of alloy PMWY-2 that had been recrystallized at 1300°C. Two initial creep rupture tests were performed in air. The first test, at 980°C and 48 MPa, failed in 68.35 hr with a final elongation of 1.7% and a minimum creep rate of 0.01%/hr. The next test at 1075°C at the same stress resulted in a creep-life of 8.3 hr, with a final elongation of 3.1% and a minimum creep rate of 0.04%/hr. The curves of life-versus-elongation are shown in Fig. 5. Both specimens exhibited low minimum creep rates when compared to precipitation-strengthened Fe_3Al-based alloys [9], at a higher temperature than possible with these alloys. The results of these two tests are compared with binary Fe_3Al, the precipitation-strengthened Fe_3Al-based FA-180 alloy, and two stainless steels in Fig. 6.

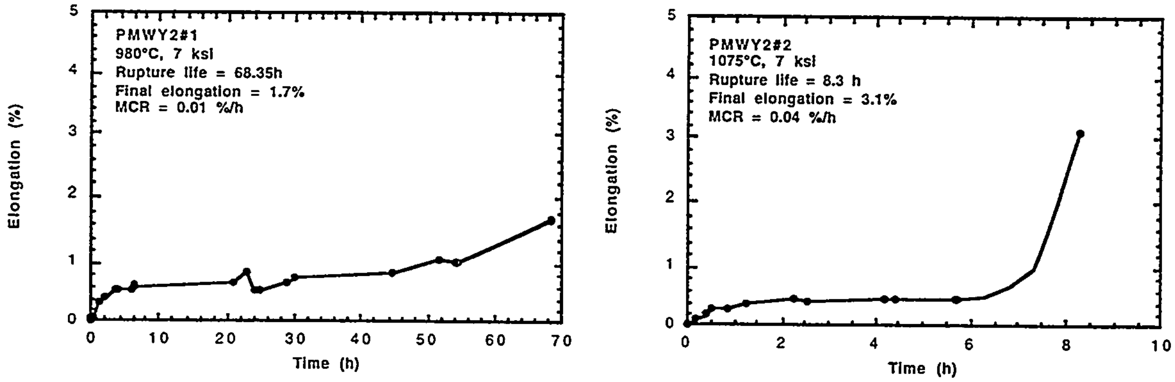

Fig. 5. Creep-rupture curves for PMWY-2 alloy tested at a stress of 48 MPa at (a) 980°C and (b) 1075°C in air.

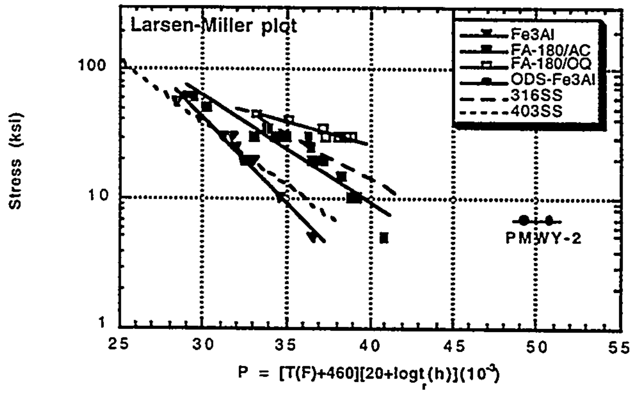

Fig. 6. Larson-Miller plot to compare creep performance of PMWY-2 with Fe_3Al, alloy FA-180 and two stainless steels.

Examination of the specimens after testing indicated that the mode of failure was not uniform, as illustrated in the scanning electron microscopy (SEM) secondary electron images in Fig. 7. Figure 8a shows that over half of the fracture surface of the 1075°C specimen exhibited had a brittle, transgranular appearance with dimples and pores characteristic of microvoid coalescence. There were also long stringer-like features which appeared more ductile and possibly contained particles (Fig. 8b). High magnification examination of the area of brittle fracture showed the presence of oxides (assumed to be the Y_2O_3 dispersion) and small pores (visible as black dots in Fig. 8c). However, there was no obvious origin of the crack in the area of either specimen that had experienced brittle fracture. Further creep testing was suspended until the cause of the brittle failure was found.

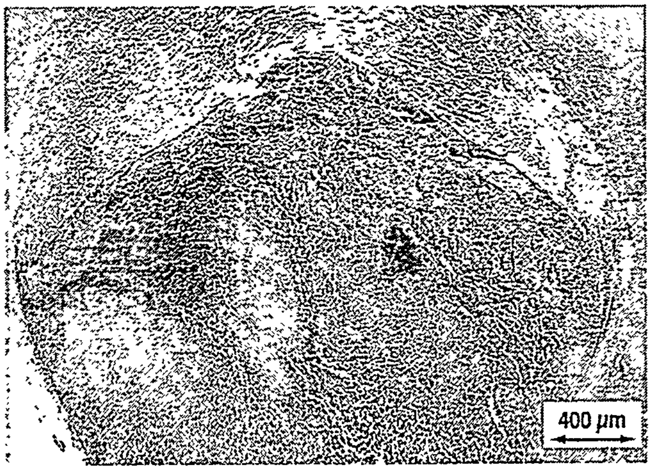

Fig. 7. SEM image of fracture face of specimen tested at 1075°C showing the non-uniform nature of the creep rupture.

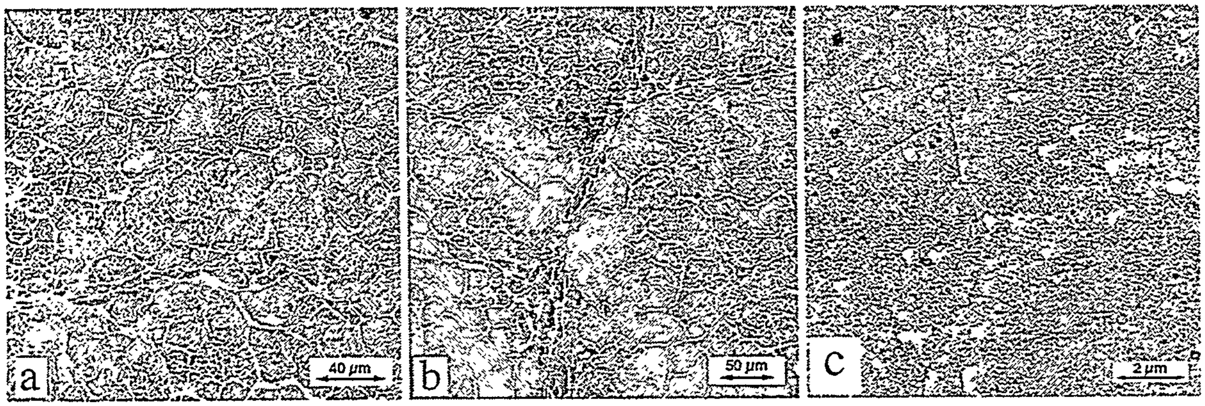

Fig. 8. SEM images showing typical features of the more brittle regions of the creep rupture surfaces of PMWY-2: (a) microvoids in specimen tested at 980°C, (b) stringer in specimen tested at 980°C, (c) cavities, oxide particles, and needle-like phase in specimen tested at 1075°C.

Figure 9 is an optical micrograph showing the creep rupture in the short-transverse direction parallel to the extrusion direction from the specimen tested at 1075°C. Approximately half of the specimen cross section that fractured transgranularly in a brittle manner apparently corresponded to one of the two grains that constituted the cross section of the gauge length (Fig. 9a), The roughly one-third of the specimen that had begun to neck down corresponded to the other main grain in the essentially bi-crystal specimen, and contained a large number of creep cavities and evidence of cavity growth and coalescence near the fracture (Fig. 9b). A light etch of the specimen indicated the possible existence of several elongated grains of up to 200 μm in width in the part of the specimen that had necked and elongated (Fig. 9b). Whereas the cross section of the gage length away from the fracture contained basically two visible grains running the length of the specimen, near the center of the section was a stringer about 3 mm long consisting of what appeared to be finer, unrecrystallized grains and inclusions; this region did not appear to play any part in the specimen failure. Also visible in the necked area of the specimens were enlarged voids (or creep cavities) which had been distorted by the necking, and a phase with a needle-like morphology characteristic of a carbide phase such as Fe_3AlC [10] visible in Fig. 8c..

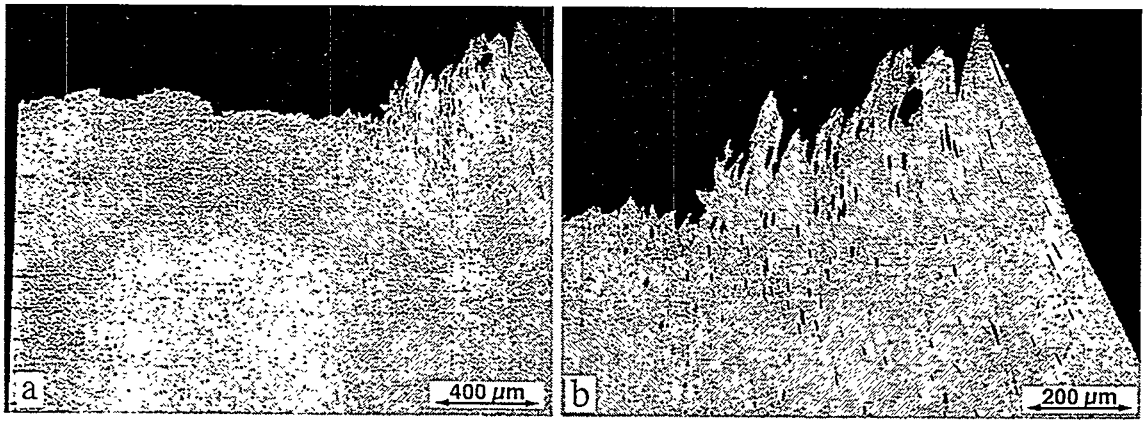

Fig. 9a. Cross section of fracture face of specimen tested at 1075°C, showing: (a) complete fracture section, and (b) enlarged view of necked region.

Reexamination of specimens used in the 1300°C recrystallization experiments indicated areas in one specimen of alloy PMWY-2 which exhibited internal cracks, as shown in Figs. 10a and b. The appearance of these cracks suggested a crystallographic preference, and that they probably occurred after the annealing treatment. No such cracks were observed in any of the specimens annealed at temperatures from 1150°C to 1250°C, or at 1380°C. This examination is continuing.

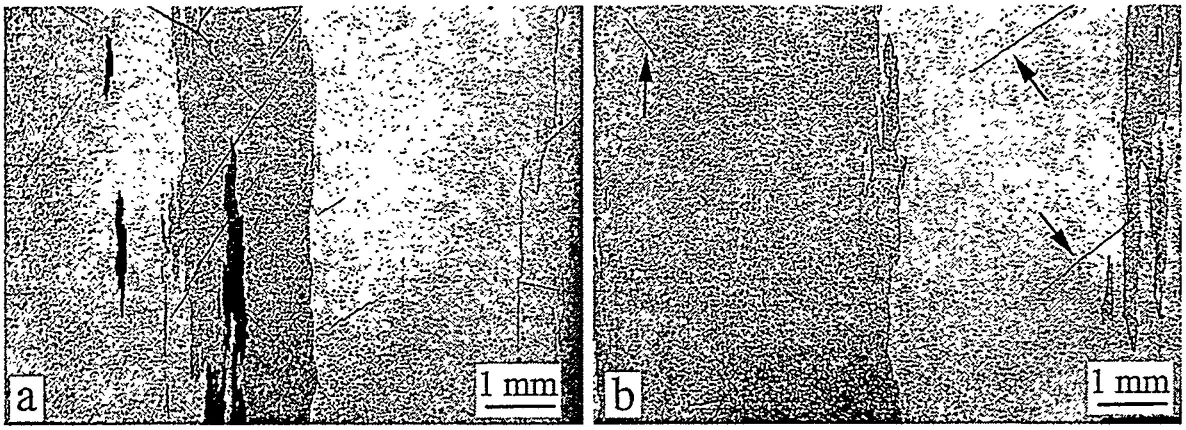

Fig. 10. Cracking in Alloy PMWY-2 annealed at 1300°C for (a) 1hr and (b) 2 hr.

OXIDATION LIFETIME TESTS

Data for use in estimating the high-temperature oxidation lifetimes of a recrystallized alloy (PMWY-2) and non-recrystallized alloy (PMWY-3) were generated by means of thermal cycling tests using specimens exposed in individual, lidded alumina crucibles in air in a muffle furnace. The exposure temperature was 1100°C, and each thermal cycle lasted for 100 hr. The specimen weight changes in this test are compared in Fig. 11a with data for an earlier version of this alloy (FAS3Y) made at ORNL [11], and for three commercial ODS FeCrAl alloys (Kanthal APM, MA956, ODM-751). The most obvious result is the large reduction in scale spallation for the PMWY alloys compared to FAS3Y, although there still appears to be a tendency to some spallation at times longer than 1,200 hr. The reasons for this improvement are not immediately clear; the PMWY specimens will be examined when the exposures are completed. Despite the tendency to some scale spallation, the overall weight change due to oxygen uptake (aluminum consumption), shown in Fig. 11a, was very similar for the PMWY alloys and the ODS-FeCrAl alloys. The fact that the kinetics for each PMWY alloy corresponded to a single near-parabolic rate suggested that any scale spallation that occurred did not affect the rate-controlling scale layer, at least within the sensitivity of the test method.

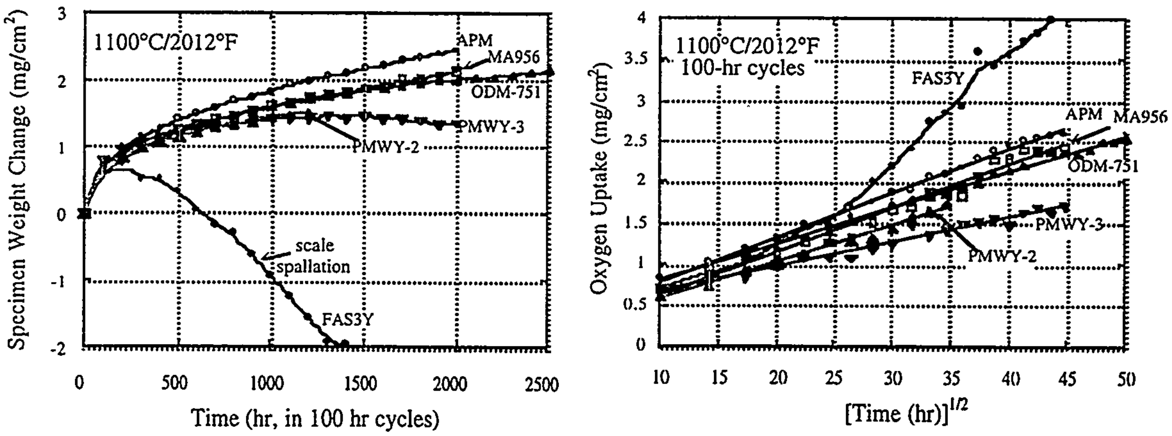

Fig. 11. Oxidation kinetics at 1100°C: (a) specimen weight gains, (b) parabolic oxidation plots

These new kinetic data were used to calculate the expected oxidation-limited lifetime of a 2.5 mm thick tube wall (following a procedure described previously [11]), with the result shown in Fig. 12. Whereas the scale spallation behavior of the FAS3Y alloy resulted in an oxidation lifetime at 1100°C equivalent to the commercial ODS-FeCrAl alloys despite its larger reservoir of aluminum (15.8 vs 4.5 to 5.5 weight percent), the reduced level of scale spallation from the PMWY alloys allowed the benefit of the larger aluminum reservoir to be realized. The projected oxidation-limited lifetime at 1100°C for the PMWY alloys ranges up to 234 x 10^6 hr, compared to 0.5 to 2.6 x 10^6 hr for the commercial ODS-FeCrAl alloys.

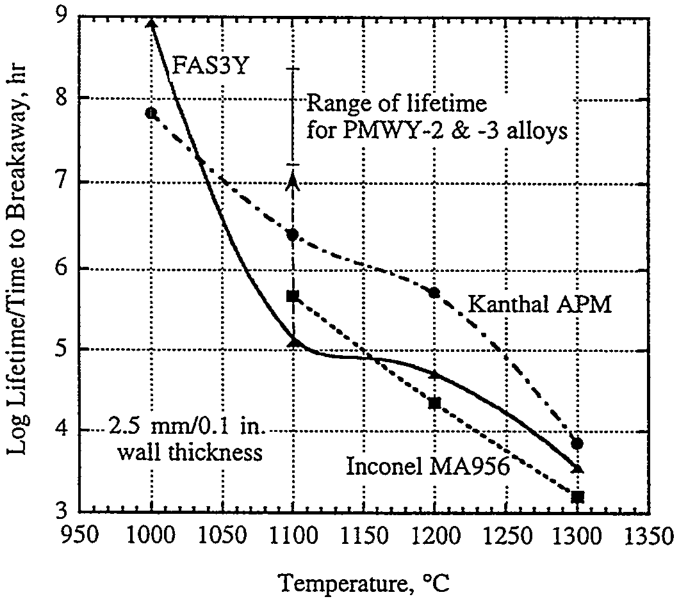

Fig. 12. Estimated oxidation-limited lifetimes for ODS alloys (2.5 mm wall thickness), with data for new ODS-Fe_3Al alloys indicated at 1100°C

CONCLUSIONS

The large, high aspect ratio grain structure desired in ODS alloys for good high-temperature creep strength has been achieved in yttria-strengthened Fe_3Al, with specimens exhibiting grains several centimeters long. The annealing treatment used to recrystallize the alloys also resulted in the formation of porosity in the alloy, which must be minimized in order to maximize the mechanical performance of the alloy. Initial creep tests at relatively high temperatures indicated good promise, but premature failure of the first specimens by a partially brittle mode prevented realization of the full potential of the grain structure. The cause of the brittle behavior is the subject of investigation, and was not obviously linked to pre-existing defects. The oxidation-limited lifetime at 1100°C in air for the alloys derived from commercially-processed alloy powder was significantly longer than for similar ORNL-processed alloys, due to a reduced tendency to scale spallation. The oxidation data for the ODS-Fe_3Al also suggest a longer life at 1100°C than competing commercial ODS-FeCrAl alloys.

ACKNOWLEDGMENTS

This research was sponsored by the Fossil Energy Advanced Research and Technology Development (AR&TD) Materials Program, U. S. Department of Energy, under contract DE-AC05-84OR21400 with Lockheed Martin Energy Research, Inc. Mr. H. F. Longmire was responsible for the metallographic preparation of the specimens, and Mr. C. A. Carmichael performed the creep tests.

REFERENCES

1. J. M. Klara,"HIPPS: beyond state-of-the-art, Part I," *Power Engineering*, 12, 37-39 (1993).
2. J. M. Klara, "HIPPS can compete with conventional PC systems: Part II," *Power Engineering*, 13, 20-23 (1994).
3. F. L. Robson, J. Ruby, and D. J. Seery, "Repowering with High-Performance Power Plant Systems (HIPPS)," Proc. Pittsburgh Coal Conf. (Sep. 1996), pp. 162-167.
4. Q. J. Mabbutt, The British Gas Closed Cycle Demonstrator-Final Year Report, British Gas Report (1995).
5. W. Lengauer, P. Ettmayer, D. Sporer, and G. Korbe, "Pore Formation in P/M Ferritic ODS Superalloys During High-Temperature Heat Treatment I. Considerations and Experimental Starting Points," Powder Metallurgy Intl., 22 (2), 19-22 (1990).

6. D. Sporer, W. Lengauer, P. Ettmayer, and G. Korbe, "Pore Formation in P/M Ferritic ODS Superalloys During High-Temperature Heat Treatment II. Thermodynamic Considerations and Conclusions," Powder Metallurgy Intl., 23 (3), 162-165 (1991).

7. B. Heine, R. Kirchheim, U. Stolz, and H. Fischmeister, "Studies on Pores Caused by Annealing ODS-Iron-Base Superalloys," Powder Metallurgy Intl., 24 (3), 158-163 (1992).

8. Q. J. Mabbutt, British Gas plc., private communication with I. G. Wright, 1996.

9. C. G. McKamey and P. J. Maziasz, "Effect of Heat Treatment Temperature on Creep-Rupture Properties of Fe_3Al-Based Alloys," Processing, Properties, and Applications of Iron Aluminides, Eds. J. H. Schneibel and M. A. Crimp, TMS, Warrendale, PA (1994), pp. 147-158.

10. M. Palm, and G. Indin, "Experimental Determination of Phase Equilibria in the Fe-Al-C System," Intermetallics, 3, 443-454 (1995).

11. I. G. Wright, B. A. Pint, E. K. Ohriner, and P. F. Tortorelli, "ODS Iron Aluminides," Proc. Tenth Ann. Conf. on Fossil Energy Materials, ORNL Report No. ORNL/FMP-96/1, CONF-9605167 (1996), pp. 359-371.(1996), pp. 359-371.

Iron Aluminide Weld Overlay Coatings for Boiler Tube Protection in Coal-Fired Low NOx Boilers

S.W. Banovic, J.N. DuPont, and A.R. Marder

Energy Research Center
Lehigh University
Bethlehem, PA 18015

ABSTRACT

Iron aluminide weld overlay coatings are currently being considered for enhanced sulfidation resistance in coal-fired low NOx boilers. The use of these materials is currently limited due to hydrogen cracking susceptibility, which generally increases with an increase in aluminum concentration of the deposit. The overall objective of this program is to attain an optimum aluminum content with good weldability and improved sulfidation resistance with respect to conventional materials presently in use. Research has been initiated using Gas Tungsten Arc Welding (GTAW) in order to achieve this end. Under different sets of GTAW parameters (wire feed speed, current), both single and multiple pass overlays were produced. Characterization of all weldments was conducted using light optical microscopy, scanning electron microscopy, and electron probe microanalysis. Resultant deposits exhibited a wide range of aluminum contents (5 - 43 wt%). It was found that the GTAW overlays with aluminum contents above ~10 wt% resulted in cracked coatings. Preliminary corrosion experiments of 5 to 10 wt% Al cast alloys in relatively simple H_2/H_2S gas mixtures exhibited corrosion rates lower than 304 stainless steel.

INTRODUCTION

To comply with clean air regulations, fossil fired boilers are being retrofitted to reduce NOx emissions[1-3]. The design principle is to delay the mixing of fuel and air to create a low temperature, fuel-rich flame which will suppress the NOx formation in a substoichiometric combustion gas[2]. In conventional burners, sulfur from the fuel is generally oxidized to form SO_2 and SO_3, which are generally non-corrosive at furnace wall temperatures. However, with newer low NOx burners, H_2S is now generated and protective oxide scales are often replaced by less protective sulfide scales. In order to protect the existing tubes from accelerated sulfidation attack, stainless steel and superalloy weld overlay coatings are typically used. These alloys are expensive and form a brittle interfacial layer which is often susceptible to cracking under thermal cycling conditions. In contrast, iron aluminide alloys with aluminum contents above ~10 wt% Al possess excellent sulfidation resistance in very aggressive environments [6-9] and form no brittle interface between the substrate and coating. However, the aluminum content of the overlay is limited due to hydrogen cracking susceptibility, which generally increases with an increase in the aluminum concentration [10-12]. Previous research on iron aluminides utilized gases which were very aggressive and may not be indicative of low NOx boiler conditions [2-4]. Therefore, research has been initiated to evaluate weldable coatings, i.e. lower aluminum overlays, in environments more representative of low NOx boilers. The overall objective of this work is to study various iron aluminum weld overlay compositions and relate their processing and microstructure to properties which are critical in low NO_x boiler environments: weldability, sulfidation. These results will be compared with other weld overlay candidates being considered.

EXPERIMENTAL PROCEDURE

Overlay samples were produced using Gas Tungsten Arc Welding (GTAW) conducted in a fully automated welding research laboratory. The wire feed speed and current were varied to produce different aluminum concentrations within the deposits. Pre-heat and post-weld heat treatments were not conducted on the GTAW overlays, but an interpass temperature was maintained between 300-350°C for the multiple pass welds. A dye penetrant technique was used to assess cracking of the overlays.

Cast Fe-Al alloys with varying aluminum contents, based upon the preliminary GTAW weldability studies, were produced at Oak Ridge National Laboratories by arc-melting high purity components under argon and drop casting into a water cooled copper mold. Obtaining bulk specimens eliminated the timely task of removing samples from the weld material, as well as eliminating the aluminum-poor region near the substrate that could negatively influence the corrosion behavior [13].

Sulfidation corrosion behavior was characterized by use of a thermogravimetric balance that measured weight gain as a function of time. Samples with dimensions 10mm x 12mm x 3mm were cut from the cast Fe-Al alloys. Samples were ground to 600 grit with silicon carbide papers, ultrasonically cleaned, and weighed to the nearest mg before being placed in the balance. Samples were heated at a rate of 50°C/min and isothermally held at 600°C for 50 hr in a mixed gas consisting of 0.1% H_2S - 3.0% H_2 - bal Ar (by volume). The oxygen partial pressure, as determined by a solid-state oxygen cell, was 10^{-28} atm, and the sulfur partial pressure was estimated to be 10^{-9} atm. Samples were then cooled to room temperature at a rate of 20°C/min before removal from the chamber.

Samples for microstructural analysis were removed using an abrasive cut-off wheel and cross-sections mounted in cold-setting epoxy. Metallographic samples were polished through 0.04μm colloidal silica and etched with a solution of 60ml methanol, 40ml nitric acid, and 20ml hydrochloric acid. Microstructural characterization was performed with both light optical microscopy (LOM) and scanning-electron microscopy (SEM). Qualitative and quantitative compositional information was obtained via energy dispersive spectroscopy (EDS) and wavelength dispersive spectrometry (WDS), respectively. WDS was conducted on a JEOL 733 SuperProbe using an accelerating voltage and probe current of 15kV and 15nA, respectively. K_α x-ray lines were analyzed and counts converted to weight percentages using a ϕ (ρz) correction scheme.

RESULTS and DISCUSSION

Weldability

Figure 1 shows the sample matrix of single weld pass overlays produced by GTAW. To obtain a wide range of aluminum contents in the overlay, wire feed speeds were varied between 10 and 65 mm/sec at current levels of 250, 275, and 300A. Single pass overlays were first deposited to ensure that the microstructure and compositions of the overlays were not complicated by overlapping passes. Samples were assessed as crack/no crack using a dye penetration technique. For those that were cracked, the number of cracks that occurred are located to the right of the symbols in Figure 1, with M signifying more than 15 cracks in the sample. The numbers to the left of the symbols denote the amount of aluminum in the deposit (in wt%) as measured using EPMA. Below ~10 wt% Al the overlays did not crack, while those just above this value had very few cracks. While two different types of microstructures were observed (see reference [14]), cracking was not controlled by any type of microstructural feature. Overlay compositions on either side of the crack/no crack boundary exhibited reproducible cracking tendencies.

Based upon the single pass results, a second experimental matrix was conducted to produce multiple pass weld overlays using similar parameters, Figure 2. As found for the single pass welds, the cracking results were again related to the aluminum concentration of the overlays. Due to the 50% overlap of adjacent passes, the aluminum contents of the multiple pass welds were higher than that of the corresponding single pass overlays prepared at identical processing parameters. Electron microprobe traces through the overlay, conducted parallel to the coating-substrate interface, showed that the weldement was relatively homogeneous on a macroscopic scale at these processing parameters, Figure 3. Large columnar grains were found for all samples, with cracks occurring in both intergranular and transgranular modes.

The combination of high wire feed speed and low current produced cracked overlays for both sets of deposits. This processing scheme results in high aluminum in the overlay due to the larger volume of Al being added to the system, as well as reduced mixing between the two constituents [15]. During deposition, current flowing through the arc is the main source of heat that melts the base metal and filler wire. While in the liquid state, mixing occurs to produce an alloy of the two elements with a composition dependant upon the volume of

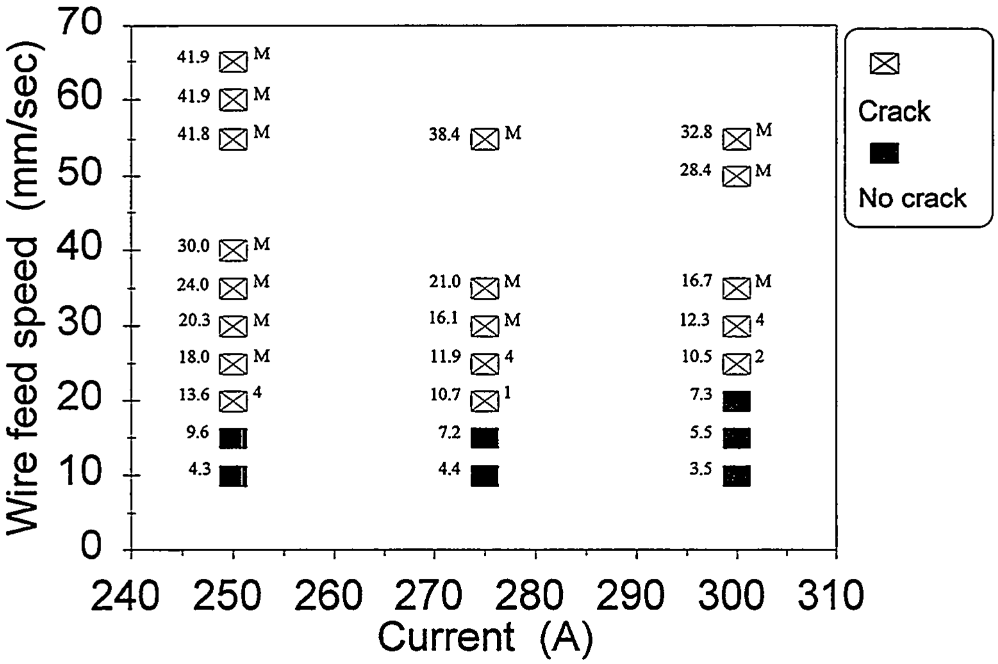

Figure 1: Sample matrix of single weld pass overlays produced by GTAW. Each box represents an overlay deposited at that processing condition and was subsequently labeled as cracked or no crack. Numbers to the right of the cracked data points signifies the number of cracks that occurred, with M being more than 15. The numbers to the left denote the wt% of aluminum in the deposit.

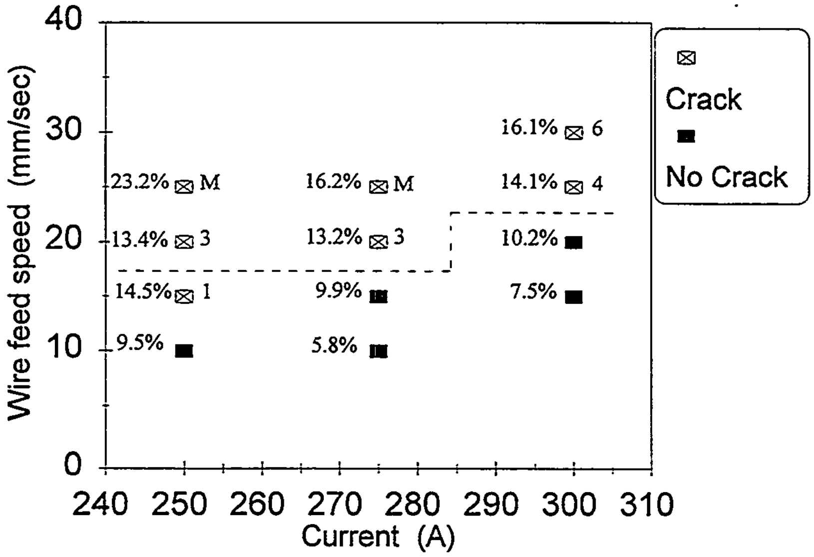

Figure 2: Sample matrix of multiple pass weld overlays. The symbols correspond to those in Figure 1. The crack/no crack boundary for the single weld pass overlays is represented by the dashed line.

each material that was melted. For a fixed wire feed speed, decreasing the current results in a smaller volume of melted substrate that can mix with the melted wire, thus leading to higher aluminum concentrations in the overlay. Conversely, for a fixed current, increasing the wire feed speed allows for more melted aluminum to mix with the base metal, again resulting in higher aluminum contents. The decrease in mixing through out the weld can be better illustrated by the electron microprobe traces, perpendicular to the coating-substrate interface, through the single weld bead and partially mixed zone (PMZ), Figure 4. It is also believed that this decrease in mixing contributed to the formation of the dendritic structure found at the higher aluminum weight percentages.

The higher aluminum content overlays have previously been found to be more susceptible to hydrogen-induced (cold) cracking [10,11]. During the welding process, stresses are formed in the substrate that place the weldement in tension after solidifying. The stresses, in addition to the available hydrogen from the atmosphere, were seen to cause cracking soon after solidification, as well as days after depositing the overlays. In order to assess the reliability of the small scale plate results, deposition of ≤ 10 wt% Al overlays onto large scale panels using the GMAW are planned in future experiments.

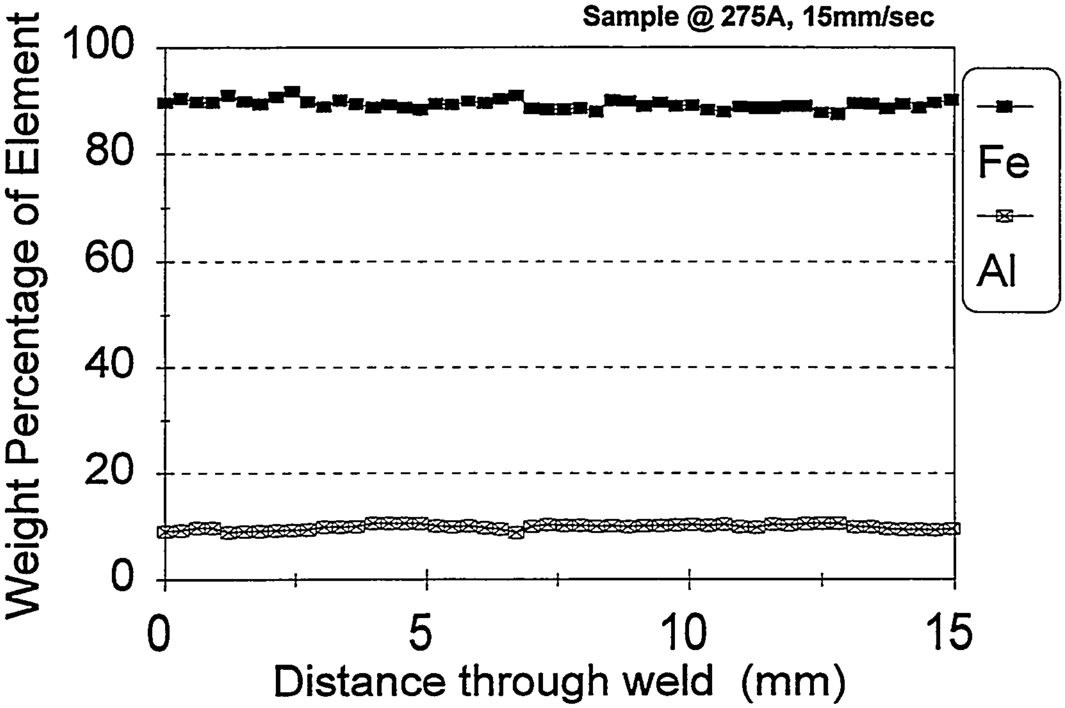

Figure 3: Electron microprobe trace parallel to the coating-substrate interface for a multiple pass weld overlay showing a relatively homogeneous composition on a macroscopic level.

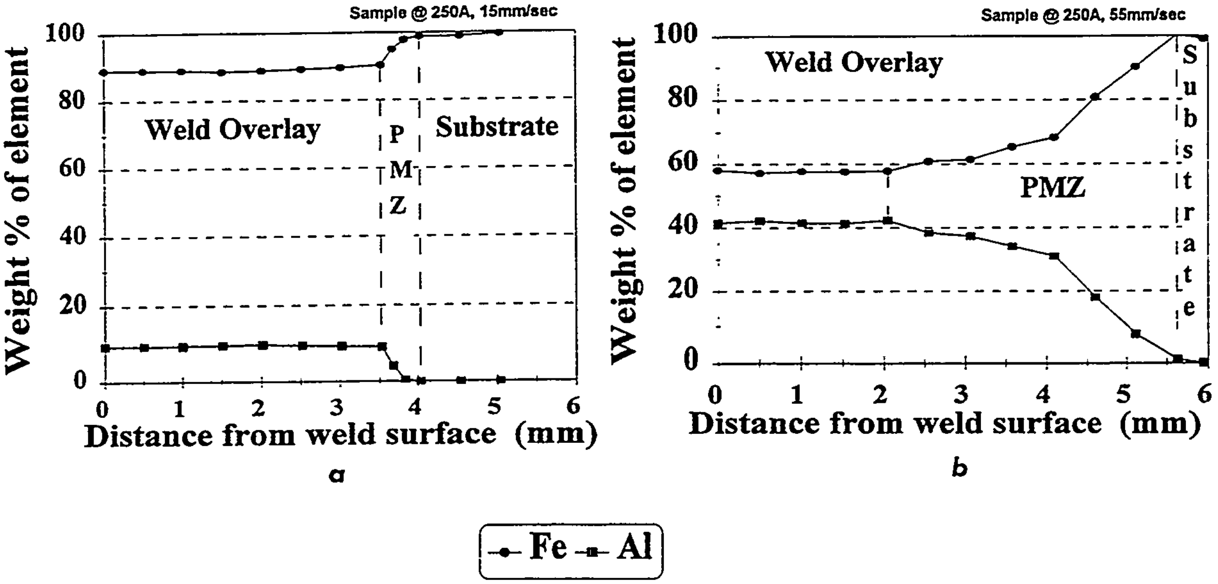

Figure 4: Electron microprobe trace perpendicular to the coating-substrate interface showing a) high level of mixing in a low aluminum content overlay and b) low level of mixing in a high aluminum content overlay.

Corrosion Resistance

The work of Tortorelli et. al [13,16] showed that the oxidation/sulfidation resistance of iron aluminide weld overlay coatings could be explained on the basis of what was known from previous studies of bulk samples of similar compositions. Therefore, cast Fe-Al alloys, with aluminum contents beneath the crack/no crack boundary of Figure 1 (5, 7.5, and 10 wt% Al), were used for preliminary corrosion studies. In addition, by using the cast alloys, the aluminum-poor region near the coating-substrate interface, as seen in Figure 4b, was eliminated. Prior research [13] demonstrated that the corrosion products more readily form on the face closer to the substrate of weld overlay corrosion samples due to the inhomogeneous composition in this area. If this Al depleted region is not throughly removed, the corrosion behavior may be negatively influenced.

The corrosion environment chosen was generally less *aggressive* than those presently found in the literature [5-9,13,16], in terms of gas composition and temperature, so as to be more representative of boiler conditions[2-4]. Previous work on binary Fe-Al alloys showed that up to ~750°C, at least 10 wt% ($\geq$ 18 at%) is needed for good sulfidation resistance [5-8]. However, these studies had either higher temperatures or partial pressure of sulfur than the conditions selected here. The simple gas mixture for these studies should promote the formation of iron sulfide and aluminum oxide at the partial pressures and temperatures denoted [1,17]. After an understanding of the kinetics of this simple gas, multiple component gases will be used to further evaluate the corrosion resistance of the alloys.

The weight changes for the alloys tested are shown in Figure 5. The 5 wt% alloy was the only one to displayed a significant weight gain among the Fe-Al alloys, which nearly tripled that of the other two tested. The linear kinetic rate for this alloy (k_l = 3.22 x 10^{-4} mg cm^{-2} min^{-1}) was less than those previously reported [5] for similar alloys in more aggressive conditions (k_l = 7.1 x 10^{-2} mg cm^{-2} min^{-1}). The 7.5 and 10 wt% alloys had negligible weight gain, especially when compared to the 1008 and 304SS alloys.

The weight gain measurements can be collaborated with SEM micrographs of the sample surfaces, Figure 6. The decrease in corrosive product can be seen as the aluminum content increases in the alloy. The 5 wt% sample has a scale that completely covered the surface. EDS techniques detected iron and sulfur. The scale morphology, consistent with previous research [5,17], in addition to the EDS spectra, suggests this is an iron sulfide scale. An aluminum peak was not present in the spectra indicating that the iron sulfide scale is either a few microns thick, since the interaction volume is ~ 1 μm with these SEM parameters [18], or very little aluminum is present in the product. The 7.5 wt% alloy had few, large iron sulfide particles on the surface (Figure 6b), with the presence of an aluminum peak in the EDS spectra. The 10 wt% alloy was devoid of any large particles (Figure 6c) and the spectra showed all three peaks (Fe, Al, and S). Due to limitations of the EDS system, oxygen could not be detected to determine if the formation of any oxides occurred.

With the promising corrosion resistance of the low Al content alloys in the simple gas presented here, future investigation into the influence of more severe gas compositions and higher temperatures on the corrosion behavior of these alloys is planned.

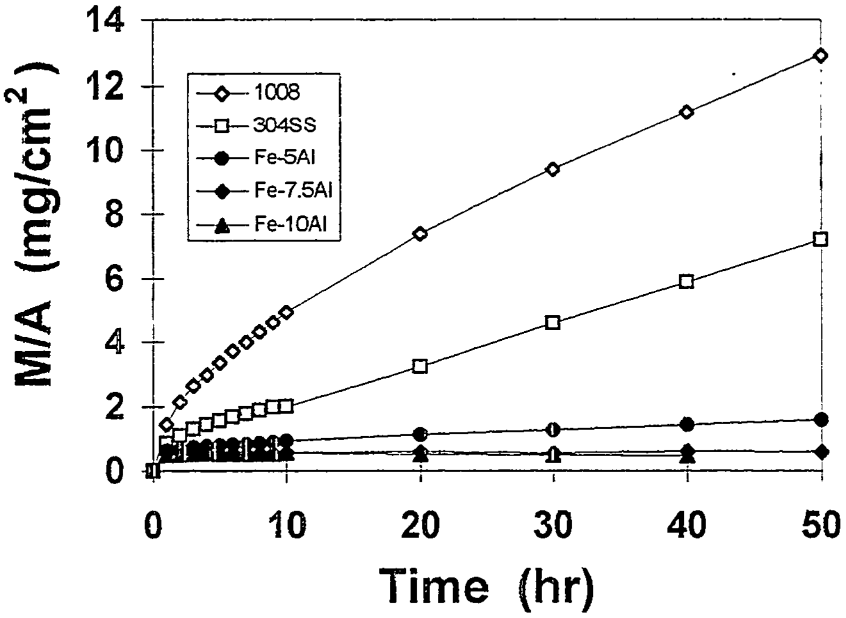

Figure 5: Weight change versus time for commercial and cast Fe-Al alloys exposed to 0.1%H2S - 3.0%H2 - bal Ar at 600°C for 50 hr.

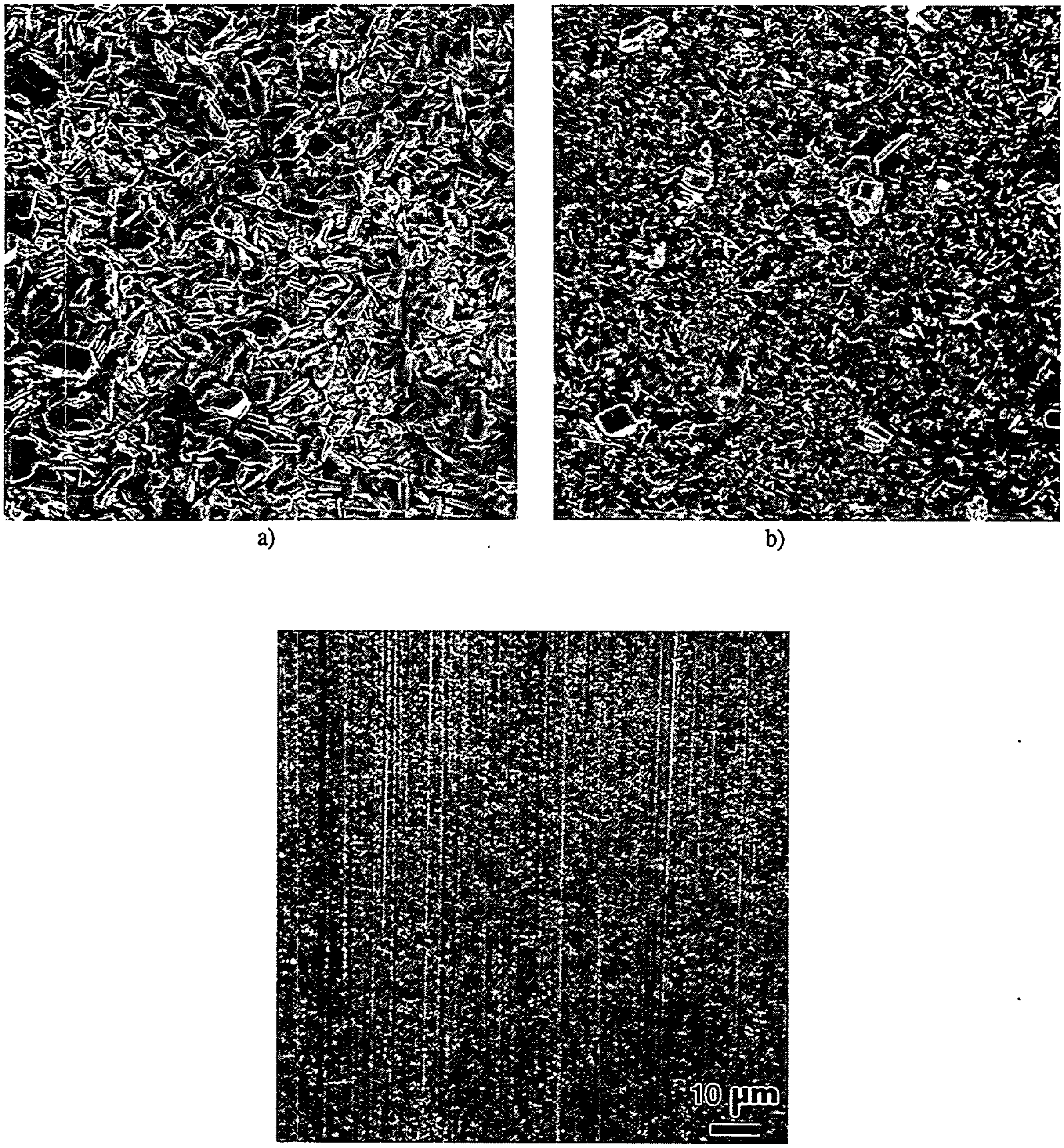

a)

b)

c)

Figure 6: SEM micrographs showing the corroded surface of a) the 5 wt% Al alloy, b) the 7.5 wt% Al alloy, and c) the 10 wt% Al alloy.

SUMMARY

This goal of this research is to find a compositional window in which weldable Fe-Al coatings can be deposited and perform well in environments indicative of low NOx boilers. Initial weldability studies have shown that below 10 wt% Al, sound overlays coatings can be produced without a pre- or post weld heat treatment using GTAW. Preliminary corrosion studies of alloys near this compositional boundary show promise in environments, while less aggressive than typically seen in the literature, indicative of boiler conditions.

FUTURE WORK

Future work will include installation of a co-extruded Fe-Al alloy tube, currently being prepared at ORNL, into an actual low NOx boiler to provide information on the corrosion resistance of Fe-Al alloys in real boiler environments. Weld overlays with ≤ 10 wt% Al will be deposited onto large-scale boiler tube panels using GMAW to correlate the weldability results of the small scale plates to actual large-scale panels. The influence of gas composition, aluminum content (5.0 to 12.5 wt% Al), and temperature on the corrosion behavior of Fe-Al alloys will be investigated in detail.

ACKNOWLEDGMENTS

This research was sponsored by the Fossil Energy Advanced Research and Technology Development (AR&TD) Materials Program, US Department of Energy, under contract DE-AC05-96OR22464 with Lockheed Martin Energy Research Corporation. The authors wish to thank V.K. Sikka from ORNL for the Fe-Al cast alloys used in corrosion testing.

REFERENCES

1. Stringer, J. 1990. In High Temperature Oxidation and Sulphidation Processes, ed. J.D. Embury, Pergamon Press, Toronto, Ontario, pp. 257-75.
2. Chou, S.F, Daniel, P.L., Blazewicz, A.J., and Dudek, R.F. Hydrogen Sulfide Corrosion in Low NOx Combustion Systems, presented to the Metallurgical Society of AIME, Detroit, Michigan, Sept 17-19, 1984, Babcock & Wilcox report # RDTPA 84-12.
3. Urich, J.A. and Kramer, E. Designing Solutions for Low NOx Related Waterwall Corrosion. In *1996 Internaitional Joint Power Generation Conference, Vol 1*, pp.25-9, ASME, EC-Vol. 4/FACT-Vol. 21.
4. Gabrielson, J.E. and Kramer, E.D. Measurement of Reducing Gases Formed in Low NOx Combustion. In *1996 International Joint Power Generation Conference, Vol 1*, pp.19-23, ASME, EC-Vol. 4/FACT-Vol. 21.
5. Strafford, K.N. and Manifold, R. 1969. The Scaling Behavior of an Iron-5% Aluminum Alloy in Sulfur Vapor, Oxidation of Metals, 1 (2), pp. 221-40.

6. Strafford, K.N. and Manifold, R. 1972. The Effects of Aluminum Alloying Additions on the Sulfidation Behavior of Iron, Oxidation of Metals, 5 (2), pp. 85-112.
7. Patnaik, P.C. and Smeltzer, W.W. 1985. Journal of the Electrochemical Society, 132, pp 1226-32.
8. Smith, P.J. and Smeltzer, W.W. 1987. Oxidation of Metals, 28, pp. 291-7.
9. DeVan, J.H. and Tortorelli, P.F. 1992. High Temperature Corrosion of Iron Aluminides, Corrosion 92, Paper 127.
10. Maziasz, P.J., Goodwin, G.M., Liu, C.T., and David, S.A. 1992. Effects of Minor Alloying Elements on the Welding Behavior of FeAl Alloys for Structural and Weld-Overlay Cladding Applications, Scripta Metallurgica et Materialia, 27 (12), pp. 1835-40.
11. David, S.A., Horton, J.A., McKamey, C.G. Zacharia, T., and Reed, R.W. 1989. Welding of Iron Aluminides, Welding Journal, Sept, pp. 372s-81s.
12. Fasching, A.A., Ash, D.I., Edwards, G.R., and David, S.A. 1995. Hydrogen Cracking Behavior in an Iron Aluminide Alloy Weldment, Scripta Metallurgica et Materialia, 32 (3), pp. 389-94.
13. Tortorelli, P.F., DeVan, J.H., Goodwin, G.M., and Howell, M., "High Temperature Corrosion Resistance of Weld Overlay Coatings of Iron Aluminide", pp. 203-12 in *Elevated Temperature Coatings: Science and Technology I*, Rosemont, IL, Oct 3-6, 1994, TMS, Warrendale, PA, 1994.
14. S.W. Banovic, J.N. DuPont, and A.R. Marder, *Processing and Structure of Insitu Fe-Al Alloys Produced by Gas Tungsten Arc Welding*, ORNL/Sub/95-SU604/01, Martin Marietta Energy Systems, Inc., Oak Ridge Natl. Lab., February 1997.
15. DuPont, J.N. and Marder, A.R. 1996. Dilution in Single Pass Arc Welds, Metallurgical and Materials Transactions B, 27B, pp.481-9.
16. Tortorelli, P.F., Goodwin, G.M., Howell, M., and DeVan, J.H., "Weld-Overlay Iron-Aluminide Coatings for Use in High Temperature Oxidizing/Sulfidizing Environments", pp. 585-90 in *Heat-Resistant Materials II*, Gatlinburg, TN, Sept 11-14, 1995, ASM, Materials Park, OH, 1995
17. DeVan, J.H., Hsu, H.S., and Howell, M., *Sulfidation/Oxidation Properties of Iron-Based Alloys Containing Niobium and Aluminum*, ORNL/TM-11176, Martin Marietta Energy Systems, Inc., Oak Ridge Natl. Lab., May 1989.
18. Goldstein, J.I., et. al. Scanning Electron Microscopy and X-Ray Microanalysis, 2nd Edition, pp. 87-90, Plenum Press, New York, New York, 1992.

CORROSION PERFORMANCE OF IRON ALUMINIDES IN FOSSIL ENERGY ENVIRONMENTS*

K. Natesan
Energy Technology Division
Argonne National Laboratory
Argonne, IL 60439

ABSTRACT

Corrosion of metallic structural materials in complex gas environments of coal gasification and combustion is a potential problem. The corrosion process is dictated by concentrations of two key constituents: sulfur as H_2S or SO_2 and chlorine as HCl. This paper presents a comprehensive review of the current status of the corrosion performance of alumina scales that are thermally grown on Fe-base alloys, including iron aluminides, in multicomponent gas environments of typical coal-conversion systems. Mechanisms of scale development/breakdown, performance envelopes for long-term usage of these materials, approaches to modifying the surfaces of engineering alloys by cladding or coating them with intermetallics, and in-service experience with these materials are emphasized. The results are compared with the performance of chromia-forming alloys in similar environments. The paper also discusses the available information on corrosion performance of alloys whose surfaces were enriched with Al by the electrospark deposition process or by weld overlay techniques.

INTRODUCTION

New structural materials based on Fe-Al intermetallic alloys are being developed for application in process industries and power generation systems. In the Fe-Al system, the alloys of interest are Fe_3Al and FeAl. In general, other elements are added to these alloys to improve their mechanical and/or corrosion properties in differing environments. Corrosion resistance is generally imparted to structural alloys by in-situ development of chromia, alumina, or silica scales on the alloy surface. The slower the growth rate of the oxide, the better the oxidation resistance of the alloy. In this vein, alumina scales, with inherently slower growth rates, can offer substantial advantages over chromia scales, especially in single-oxidant environments. The oxide scales also act as barriers to the transport of corrosion-accelerating reactants such as S, Cl, and alkalis, and they retard the scaling kinetics of the underlying substrate alloys when they are exposed to multioxidant environments. The oxidation resistance of iron aluminides depends on the formation of a chemically stable Al_2O_3 surface layer upon exposure to an oxidizing environment. Studies of the phase stability in the Fe-Al-O system demonstrate that Al_2O_3 will form on the Fe aluminide class of alloys even at relatively low pO_2. The Al levels present in Fe aluminides are well in excess of the critical concentration needed for the formation of a continuous alumina scale on the surface. However, at lower temperatures, transient Fe oxides will be present and the thermodynamically stable alumina can develop a continuous scale only over long exposure times.

---

*Work supported by the U.S. Department of Energy, Office of Fossil Energy, Advanced Research and Technology Development Materials Program, Work Breakdown Structure Element ANL–4, under Contract W–31–109–Eng–38.

CHARACTERISTICS OF ALUMINA SCALES

The only thermodynamically stable solid oxide in the Al-O system is Al_2O_3 (melting point 2072°C). Various structural forms of the oxide are possible and the stability of different oxide forms is dictated by temperature. While Cr_2O_3 normally exhibits p-type electrical behavior in which Cr is mobile, alumina exhibits more complex electrical properties whereby either Al or O may be mobile. Based on the bulk self-diffusion data in polycrystalline material depicted in Fig. 1, the rate of Cr_2O_3 scale formation would be expected to exceed the rate of Al_2O_3 scale formation by more than six orders of magnitude at temperatures <1200°C, assuming growth is controlled by cation diffusion in each case. Extrapolation of the diffusion data to lower temperatures indicates that below ≈1275°C, the rate of anion diffusion will exceed the rate of cation diffusion. Below ≈900°C, the alumina is generally formed as γ-Al_2O_3 and the corrosion protection of this alumina is not well established.[1]

A comparative analysis of growth rates of Cr_2O_3 and Al_2O_3 scales was made by Hindam and Whittle.[2] The scaling-rate constants shown in Fig. 2 as a function of temperature indicate significant scatter in the data for chromia scale formed in different alloys and less scatter for formation of alumina. However, the results show that the scaling rates for alumina are at least a few orders of magnitude lower than for chromia, especially at lower temperatures. One concern is that the alumina scaling rate is so low that transient oxides of Fe, Ni, and Cr may be present in the corrosion-product scale for a long period of exposure and thus the benefit of slow-growing alumina for corrosion protection may not be realized in practice.

Oxygen partial pressure appears to have little influence on the rate of Al_2O_3 scale formation,[3] but impurities may dope the oxide and influence its growth characteristics,[4] permit formation of spinel oxides, and play a vital role in the mechanical behavior of Al-rich oxide scale. The rate of S diffusion through Al_2O_3 can be 1 to 4 orders of magnitude greater than the rate of O diffusion, depending on oxide grain size (see Fig. 3), but may be 1.5 to 4.5 orders of magnitude lower than the rate of S diffusion through Cr_2O_3.[5] In both oxides, however, the partial pressures of S_2 and O_2 will determine whether sulfidation is induced and scale breakdown occurs.[6]

OXIDATION BEHAVIOR OF AL-CONTAINING ALLOYS

In Ni-Al, Fe-Al, and Co-Al binary alloys, an Al content in excess of 10 wt.% is normally needed to support formation of a surface Al_2O_3 scale.[7] The presence of Cr reduces the amount of Al required to form Al_2O_3 (to 3-5 wt.%).[8] Chromium minimizes internal oxidation of Al by acting as an oxygen getter,[9] but when it is present in high concentrations (>25 wt.% in Fe-Cr-Al alloys), ductility and workability of the

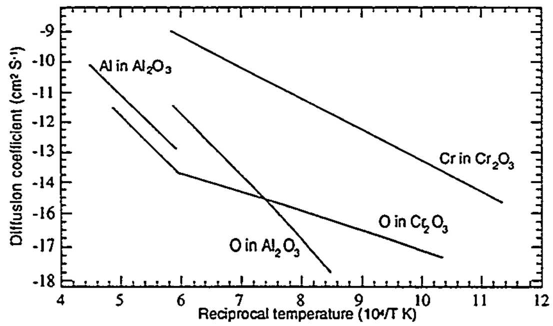

Figure 1. Self-diffusion data in chromia and alumina.

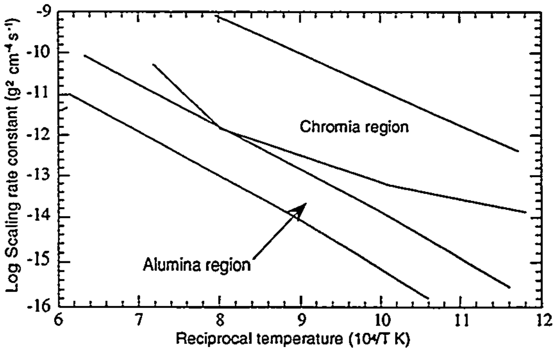

Figure 2. Rate constants for formation of alumina and chromia scales (based on data from Ref. 2)

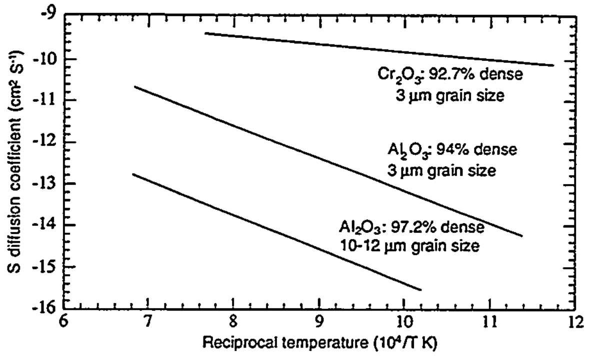

Figure 3. Rates of sulfur diffusion in alumina and chromia (based on data from Ref. 5).

alloy are impaired.[10] The commercially available structural alloys that form alumina scale generally also contain a fairly high concentration of Cr. In these alloys, the Cr-Al ratio appears to dictate the scaling kinetics and long-term mechanical integrity of the scale. A combination of good mechanical properties and oxidation resistance is generally obtained by optimizing the alloy chemistry. A Cr content of 20 wt.% or more is necessary to support alumina scale formation with only 5 wt.% Al. In the case of structural alloys, sufficient Ni in the alloy ensures austenite stability (providing creep strength), while maximizing the Fe content reduces cost. Alloy grain size is important in quaternary Fe-Cr-Ni-Al alloys in promoting alumina formation unless a second phase is present.[11]

Mechanical stability or the lack of it is a well-known problem associated with alumina scales. Scales composed of alumina commonly exhibit mechanical instability, e.g., cracking, spallation, and delamination, which poses a serious drawback in the application of Al_2O_3-forming alloys. The growth of a surface scale under isothermal or thermal-cycling conditions inevitably results in the generation of stress.[12] Compressive stresses will accumulate in a scale until some critical point is reached at which relief of stress must occur. If adhesion is poor, as it may be in many thermally grown Al_2O_3 scales, localized scale buckling may result in tensile fracture. The loss of corrosion resistance depends on the level of applied stress and also on the initial level of stress in the scale and the amount of deformation that can be accommodated. The area of metal surface exposed by scale cracking and the ability of the alloy to reform a protective scale will influence the rate of alloy degradation.

To examine the adhesion of thermally grown scales to the substrate, Natesan et al.[13] applied a tensile pull to separate the scale from the substrate. The technique they used involves attaching an epoxy-coated pin to the scale surface at a temperature sufficient to cure the epoxy. The pin is subsequently separated from the sample at room temperature by applying a tensile load. The surfaces of pulled pins are subsequently examined to assess whether the debonding occurred in the scale itself or at the scale/metal interface. The strength of the epoxy, and hence the maximum strength measurable by this procedure, was ≈71 MPa. If the applied load and pin area of contact are known, the stresses needed to pull the scale from the substrate can be calculated. The results obtained indicate a substantial scatter in the data from oxidized specimens. It is believed that for many samples (especially, for those prone to oxide spallation), voids or variations in the topography of the oxide layer result in an incomplete bond between the oxide and the epoxy-coated pin. Furthermore, in some of the samples, separation between the pin and the oxide occurred in the oxide itself rather than at the oxide/alloy interface.

Several iron aluminide alloys (see Table 1 for compositions) were used in this study. Alloy FA 186 is a ternary alloy that contains Fe, Cr, and Al and is considered a base alloy. Alloy FA 129 is designed to exhibit high ductility at room temperature while retaining its strength at high temperatures, whereas FAL is designed for improved oxidation resistance through addition of Zr. Alloy FAS is designed to resist sulfidation, and FAX is designed for improved resistance in aqueous environments by deliberate addition of Mo. Figure 4 shows the maximum stress endured by the scales on the alloys oxidized at 800, 1000, and 1200°C. The results show a peak in maximum stress value for specimens of FAS, FA 186, and FA 129 exposed at 1000°C. On the other hand, maximum stress values for FAL and FAX specimens are almost independent of exposure temperature. The adhesion test results from FAL and FAX also indicate that even with a wide variation in oxide layer thickness (resulting from oxidation for 100 h at 800-1200°C), the tensile stress needed to pull the sample from the substrate is fairly independent of oxide thickness. The difference in stress values for FAL and FAX must be due to differences in the chemistry in the scale and in the scale/alloy interface, which are directly influenced by the initial composition of the substrate alloy. The results also show that Zr (in FAL) and Nb (in FA 129) additions have a similar effect at 1000 and 1200°C, where α-Al_2O_3 will be the stable oxide in the scale. A comparison of the results obtained from these two alloys after 800°C oxidation indicates that addition of Zr, rather than Nb, may stabilize the alumina scale (i.e., minimize the transient oxides) on the alloy surface.

Table 1. Nominal chemical composition (in wt.%) of alloys cited in this paper

Material	C	Cr	Ni	Mn	Si	Mo	Al	Fe	Other
304	0.08	18.3	8.1	1.5	0.27	0.27	-	Bal[a]	-
316	0.05	17.4	13.8	1.5	0.73	2.2	-	Bal	-
310	0.07	25.0	18.7	1.21	0.64	0.002	-	Bal	-
800	0.08	20.1	31.7	0.96	0.24	0.30	0.39	Bal	Ti 0.31
GE 1541	-	15.2	-	0.001	0.07	-	4.95	Bal	Y 0.7
RV 8413	-	18.5	0.06	0.001	0.025	-	5.91	Bal	Hf 0.5
HR 160	0.05	28.0	Bal	0.5	2.75	–	–	4.0	Co 27.0
Alloy 556	0.10	22.0	20.0	1.5	0.4	3.0	-	Bal	Co 20.0, W 2.5
253 MA	0.10	20.7	10.9	0.3	1.8	-	–	Bal	Ce 0.03
FA 186	-	2.2	-	-	-	-	15.9	Bal	-
FAS	-	2.2	-	-	-	-	15.9	Bal	B 0.01
FA129	-	5.5	-	-	-	-	15.9	Bal	Nb 1.0, C 0.05
FAL	-	5.5	-	-	-	-	15.9	Bal	Zr 0.1, B 0.05
FAX	-	5.5	-	-	-	-	15.9	Bal	Nb 1.0, Mo 1.0, Zr 0.15, B 0.04
Fe-25Cr-20Ni	-	24.8	19.9	<0.01	<0.01	-	0.01	Bal	-
Fe-25Cr-6Al	-	24.6	<0.01	<0.01	<0.01	-	5.9	Bal	-
Fe-12Al	-	-	-	-	-	-	12.0	Bal	-
Fe_3Al	-	-	-	-	-	-	13.9	Bal	-
FeAl	-	-	-	-	-	-	34.0	Bal	-

[a] Indicates balance.

CORROSION IN MULTIOXIDANT ENVIRONMENTS

Protection of Fe aluminides from corrosion and environmental effects that arise from reaction with multicomponent gases and condensed products is best afforded either by formation of stable surface oxides (in this case, alumina) that are slow growing, sound, and adherent to the substrate, or by deposition of coatings that contain or develop oxides with similar characteristics. This is especially true for application of the intermetallics in integrated combined-cycle coal-gasification, low-NO_x systems, and pulverized-coal-fired and fluidized-bed combustion systems, and in gas turbine environments that are of interest in the development of fossil energy systems. In coal-gasification and low-NO_x systems, and in the first stage of magnetohydrodynamic systems, the gas environment is characterized by low pO_2 and moderate-to-high S partial pressure (pS_2), and the S is present as H_2S.[14] In combustion atmospheres and gas turbine environments, pO_2 is generally high and pS_2 is low, and the sulfur is present as SO_2. However, if combustion occurs near metal surfaces, e.g., in a bubbling fluidized bed, the local environment can be reducing and is dictated by the S sorbent equilibria, which are determined by stability fields of the $CaO/CaSO_4$-phase equilibrium.[14]

Extensive studies have been conducted on the corrosion performance of alumina-forming alloys in O/S mixed-gas environments.[15-19] Thermogravimetric studies on oxidation of Fe-base alloys with differing Al concentrations and Fe aluminide alloys showed that a minimum Al level of 12 wt.% is needed to develop a continuous alumina scale that is resistant to sulfur attack. A detailed comparison has been made of the corrosion performance of alumina- and chromia-forming alloys exposed to O/S mixed-gas environments. Weight change data, summarized in Fig. 5, show accelerated corrosion for chromia-forming alloys such as high-purity Fe-25Cr-20Ni and 310 stainless steel. Data for the Fe-25Cr-20Ni alloy show that Cr concentration at the high level of 25 wt.% does not improve sulfidation resistance of the alloy, which develops a scale (consisting of a mixture of Fe and Cr sulfide) at a very high growth rate. In fact, the presence of Ni leads to the formation of the $Ni\text{-}Ni_3S_2$ eutectic if the test is run for a longer time. The composition of this ternary alloy is similar to the base composition of the commercially available Type 310 stainless steel and its behavior is similar.[15] Alloys containing Cr and Al (RV 8413, GE 1541, and Fe-25Cr-6Al), which form alumina scale in single-oxidant environments, also exhibit significant corrosion in O/S environments.

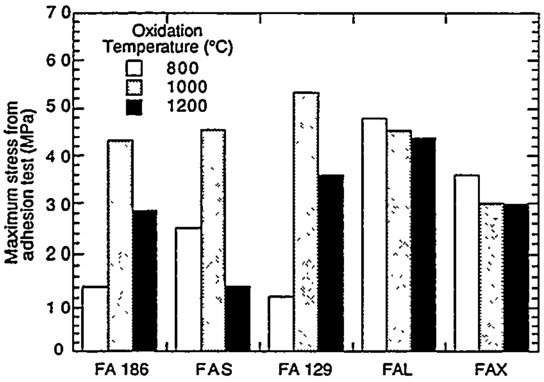

Figure 4. Maximum stress needed to pull scale from substrate for oxides that developed on several Fe-Al alloys oxidized at different temperatures (from Ref. 13)

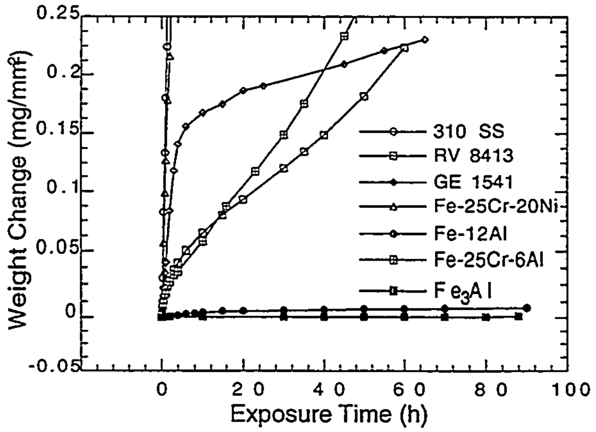

Figure 5. Weight change data for several chromia- and alumina-forming alloys tested in O/S environment with $pO_2 = 4.1 \times 10^{-18}$ and $pS_2 = 9.4 \times 10^{-7}$ atm at 875°C.

An addition of 6 wt.% Al to the Fe-25Cr alloy seems to reduce the corrosion rate somewhat but the external scale consists of Fe sulfide, which is not expected to offer protection against breakaway corrosion. The alloys GE 1541 and RV 8413 are Fe-based alloys with moderate Cr content and ≈5-6 wt.% Al. Corrosion performance of these alloys is not adequate for service in H_2S-containing environments. The binary Fe-12 wt.% Al alloy and Fe_3Al (with 13.9 wt.% Al) exhibit superior corrosion resistance in O/S mixed-gas atmospheres. The scales on these alloys were Al oxide and contained little S. The results indicate that a critical Al content in excess of 12 wt.%, which is present in Fe aluminides, is needed for alumina formation on the alloy surface in environments typical of coal conversion systems.

SURFACE ENRICHMENT WITH Al FOR CORROSION RESISTANCE

Even though the corrosion resistance of Fe-base alloys with high Al content is significant in environments that are prevalent in fossil energy systems, the use of these alloys as structural materials at elevated temperatures is very limited because of their inadequate strength properties and fabrication difficulties. Several approaches have been examined to enrich the surface regions of conventional structural alloys with Al that can form alumina scale during service, thereby offering improved corrosion protection. A promising approach for Al enrichment is the weld overlay process, in which claddings of high Al contents are produced by electrospark-deposition (ESD) and by gas tungsten arc and gas metal arc techniques. The ESD process is a microwelding technique that uses short-duration, high-current electrical pulses to deposit an electrode material on a metallic substrate. A principal advantage of the ESD process is that the overlay is fused to the metal surface with low heat input while the bulk substrate material remains at ambient temperature. This eliminates thermal distortion or changes in the metallurgical structure of the substrate. Because the overlay is alloyed with the surface, i.e., metallurgically bonded, it is inherently more resistant to damage and spalling than the mechanically bonded coatings produced by most other low–heat–input processes (such as detonation–gun, plasma–spray, and electrochemical plating). The use of welding to produce Fe aluminide layers leads to a loss of selected elements by vaporization and significant mixing of the filler metal and substrate alloys (dilution) during deposition. Because the substrates contain essentially no Al, the concentration of this element in the overlay is generally much lower than it is in the welding rod/wire used to produce the overlay.

Performance in Simulated Gasification Atmospheres

Several specimens with Al-enriched surfaces, applied on Type 316 stainless steel and Alloy 800 substrate alloys by the ESD process, were tested in simulated gasification environments that contained H_2S with or without HCl. In the first experiment, performance of the ESD coatings (which included Fe_3Al with differing bond coats of refractory metals and/or noble metals) was compared with that of uncoated austenitic alloys.[16] Figure 6 shows corrosion loss data obtained for specimens tested for 1000 h at 650°C in gas mixtures where $pO_2 = 1.2 \times 10^{-23}$, $pS_2 = 5.2 \times 10^{-10}$, $pCl_2 = 9.4 \times 10^{-17}$, and $pHCl = 2.1 \times 10^{-3}$ atm. All of the Fe aluminide coatings were resistant to sulfidation and chloride attack, whereas the base alloys were susceptible to general corrosion and pitting attack, especially in the HCl-containing environment. The weight change data and extensive microscopic analyses of tested specimens showed that the bond coats themselves do not significantly influence the corrosion process.

Further evaluation of Fe aluminide coatings was conducted with a Type 316 stainless steel substrate coated with either Fe_3Al or FeAl welding rod.[17] Coatings made with FeAl welding rod contained much more Al than those made with Fe_3Al welding rod. Type 316 stainless steel specimens with and without coatings and several commercial high-Cr alloys were exposed to O/S mixed-gas environments for up to 728 h

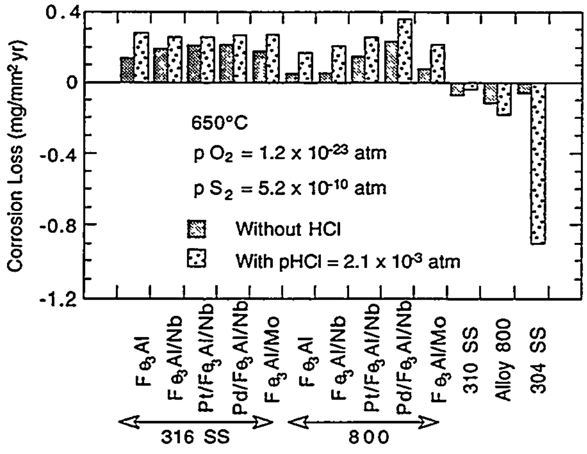

Figure 6. Corrosion loss data for several iron aluminide coatings and uncoated austenitic alloys after exposure in gas mixtures containing H_2S with and without HCl.

and periodically retrieved to measure weight changes at intermediate exposure times. Figure 7 shows weight change data for Alloy 800 and Type 316 stainless steel and for Fe_3Al- or FeAl-coated Type 316 stainless steel as a function of exposure time at 650°C to simulated gasification environments with or without HCl. The uncoated alloys exhibited some general corrosion and significant sulfidation and localized pitting corrosion. Weight gains and scaling rates were much lower for the aluminide-coated specimens than for the uncoated Type 316 stainless steel and Alloy 800.

Figure 8 shows similar weight change data for several commercial high-Cr alloys exposed together with FeAl-coated Type 316 stainless steel in O/S mixed-gas environments with and without HCl. The corrosion performance of the FeAl-coated specimen is comparable to or better than those of most other materials tested. Further, the cost of materials such as HR 160 and Alloy 556, which exhibit corrosion rates similar to FeAl layered specimen, will be a factor of 5 to 10 times higher than the FeAl coated specimen. Figure 9 shows corrosion loss data for several of these alloys and coatings calculated by parabolic kinetics.

Performance in Simulated Combustion Atmospheres

Specimens with Al-enriched surfaces, applied on Type 316 stainless steel and Alloy 800 substrate alloys by the ESD process, were also tested in simulated combustion environments that contained SO_2 with or without HCl. Specimens were tested for ≈900 h at 650°C in gas mixtures with $pO_2 = 6.7 \times 10^{-3}$, $pS_2 = 1.5 \times 10^{-35}$, $pCl_2 = 3.6 \times 10^{-4}$, and $pHCl = 1.7 \times 10^{-3}$ atm. Figure 10 shows weight change data for Alloy 800 and Type 316 stainless steel and for Fe_3Al- or FeAl-coated Type 316 stainless steel as a function of exposure time at 650°C to simulated combustion environments with or without HCl. In the absence of HCl, the uncoated alloys developed scales of (Fe, Cr) oxide or Fe oxide and tended to crack and spall, as evidenced by weight loss in Fig. 10. However, the absolute value for weight change after 900 h of exposure was <0.02 mg/mm^2. The aluminide-coated alloys showed a small weight gain due to the development of a thin, adherent alumina scale. In the presence of HCl, both the uncoated and coated alloys showed substantial weight loss at 650°C. The attack was most notable in the Fe_3Al-coated alloy, less notable in the uncoated alloys, and least notable in the FeAl-coated alloy. The primary cause for the increased corrosion of Fe_3Al-coated alloys seems to be a low concentration of Al in the coating that resulted from dilution of the deposit layer with substrate ßconstituents. Even though Fe_3Al contained ≈14 wt.% Al, the coated alloy contained <8 wt.% Al after fabrication. The results also indicate that a threshold Al concentration of >12 wt.% is necessary to improve the corrosion resistance of structural alloys.

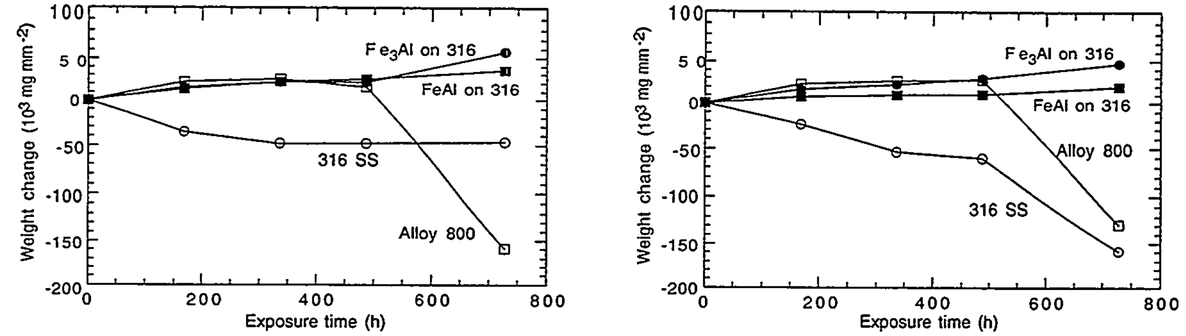

Figure 7. Weight change data for Type 316 stainless steel, Alloy 800, and Fe_3Al- and FeAl-coated Type 316 stainless steel after exposure in O/S mixed gas of composition $pO_2 = 1.2 \times 10^{-23}$ and $pS_2 = 5.2 \times 10^{-10}$ atm at 650°C (left) without HCl and (right) with $pHCl = 2.1 \times 10^{-3}$ atm.

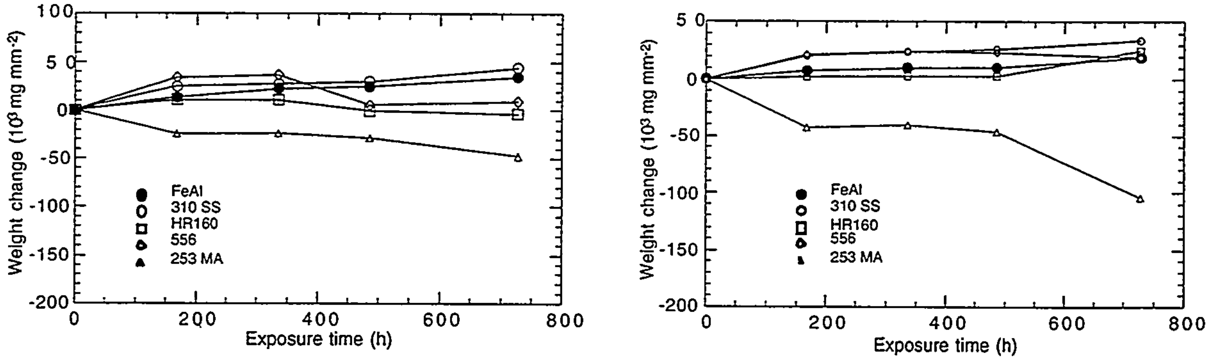

Figure 8. Weight change data for several commercial alloys and FeAl-coated Type 316 stainless steel after exposure in O/S mixed gas of composition $pO_2 = 1.2 \times 10^{-23}$ and $pS_2 = 5.2 \times 10^{-10}$ atm at 650°C (left) without HCl and (right) with $pHCl = 2.1 \times 10^{-3}$ atm.

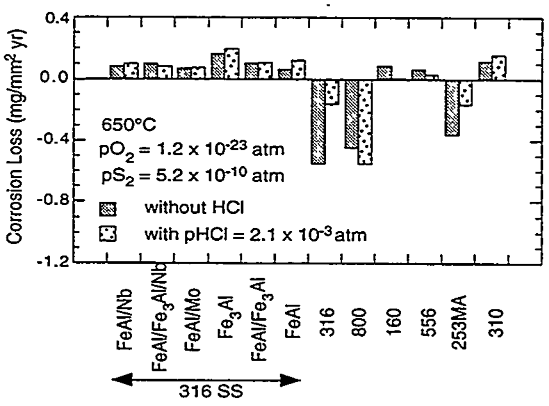

Figure 9. Corrosion loss data for iron aluminide coatings on Type 316 stainless steel and several uncoated high-Cr alloys after exposure in gas mixtures containing H_2S with and without HCl.

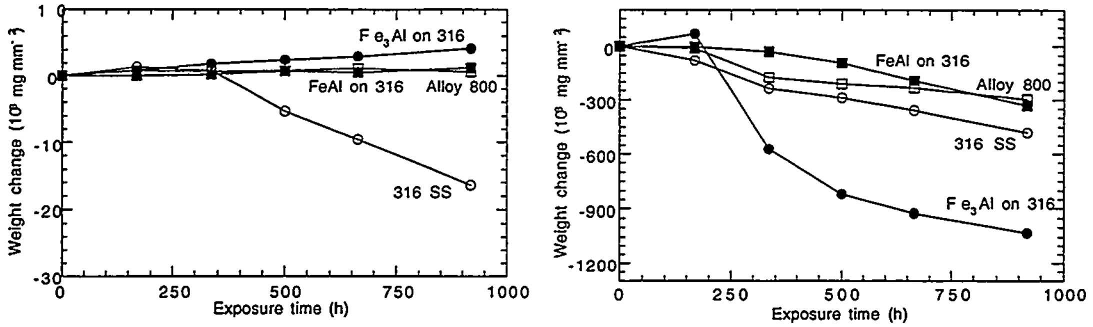

Figure 10. Weight change data for Type 316 stainless steel, Alloy 800, and Fe_3Al- and FeAl-coated Type 316 stainless steel after exposure in O/S mixed gas of composition $pO_2 = 6.7 \times 10^{-3}$ and $pS_2 = 1.5 \times 10^{-35}$ atm at 650°C (left) without HCl and (right) with $pHCl = 1.7 \times 10^{-3}$ atm.

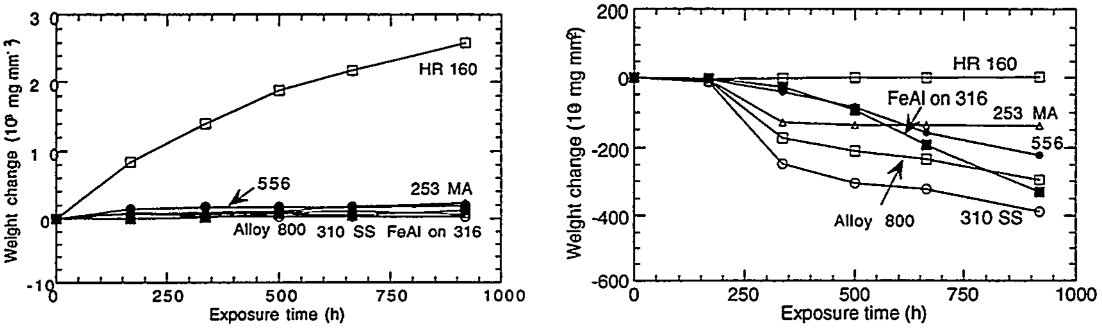

Figure 11. Weight change data for several commercial alloys and FeAl-coated Type 316 stainless steel after exposure in O/S mixed gas of composition $pO_2 = 6.7 \times 10^{-3}$ and $pS_2 = 1.5 \times 10^{-35}$ atm at 650°C (left) without HCl and (right) with $pHCl = 1.7 \times 10^{-3}$ atm.

Figure 11 shows similar weight change data for several commercial high-Cr alloys exposed together with FeAl-coated Type 316 stainless steel in simulated combustion environments with and without HCl. In the absence of HCl, all the alloys except HR 160 exhibited negligible weight gains and the scales were predominantly Cr_2O_3. HR 160 is the only alloy among those tested which contains ≈38 wt.% Ni and it is not known whether the higher Ni content of this alloy had contributed to higher oxidation in the alloy. However, the oxidation rate is still negligibly small. In the presence of HCl in the environment, all the alloys except HR 160 exhibited substantial weight loss during the 900 h exposure. HR 160 contains 2.75 wt% Si, which upon oxidation at the chromia/alloy interface, may act as a second barrier against cation migration outward and Cl penetration inward, resulting in negligible corrosive attack. MA 253, which contains 1.8 wt.% Si, exhibited weight loss for ≈300 h, beyond which the loss was negligible. Other chromia-forming alloys such as 310 stainless steel, Alloy 556, and Alloy 800 continued to lose weight during the 900 h exposure. The FeAl-coated Type 316 stainless steel, even though forming alumina scale, was found susceptible to corrosion in the HCl-containing combustion atmosphere and the rate was slightly higher than that of Alloy 556. Detailed microstructural and X-ray analyses of the corrosion-product layers from several of the tested specimens are in progress to evaluate the role of chlorine in the corrosion performance of these materials.

SUMMARY

Fe aluminides are being developed as structural materials and as cladding/overlay for conventional engineering materials. The present paper addresses the chemical compatibility aspects of these materials in environments relevant to fossil energy systems. The raw gas environments that arise from gasification and combustion of coal have chemical compositions that are widely different in pO_2 and pS_2. In addition, presence of Cl in the gas as HCl, which is determined by the Cl content of the coal feedstock, can exacerbate the corrosion process. In single-oxidant environments, such as air and low-pO_2, the oxidation rates for these alloys are significantly lower than those for chromia-forming commercial alloys. However, the mechanical integrity of the alumina scales and the reformation characteristics are key to adequate protection in long-term service. In S-containing environments, Fe aluminides offer superior corrosion resistance. Experimental data on binary Fe-Al alloys showed that a threshold Al concentration of at least 12 wt.% is needed to minimize corrosion in these environments. Further, surface enrichment of conventional structural alloys with Al-enriched surfaces produced by electrospark deposition improved corrosion resistance in simulated coal conversion environments that contained S and/or Cl. Data are presented on the performance envelope for use of these materials in S-containing environments. In Cl-containing environments, pitting-type corrosion is the dominant mode of attack on Fe aluminides but, if S is present along with Cl in gasification atmospheres, the corrosion rate seems to be determined by sulfidation rather than by Cl. On the other hand, Cl seems to have a stronger degrading effect on corrosion of these materials. Additional work is needed to establish the threshold Cl levels in the environment beyond which corrosion of aluminides and alumina-forming alloys is accelerated at different exposure temperatures.

ACKNOWLEDGMENTS

D. L. Rink assisted in the corrosion tests and microstructural analysis of exposed specimens. This work was supported by the U.S. Department of Energy, Office of Fossil Energy, Advanced Research and Special Technologies Materials Program, Work Breakdown Structure Element ANL–4, under Contract W–31–109–Eng–38.

REFERENCES

1. G. C. Wood and F. H. Stott, in High Temperature Corrosion, ed. R. A. Rapp, NACE, Houston, TX, 1983.
2. H. Hindam and D. P. Whittle, Oxid. Met. 18, 245, 1982.
3. T. A. Ramanarayanan, M. Raghavan, and R. Petrovic-Luton, Trans. Jap. Inst. Met. 34, 199, 1983.
4. P. A. Lessing and R. S. Gordon, J. Mater. Sci. 12, 2291, 1977.
5. J. B. Wagner, Defects and Transport on Oxides, p. 283, Plenum, New York, 1973.
6. P. A. Mari, J. M. Chaix, and J. P. Larpin, Oxid. Met. 17, 315, 1982.
7. G. N. Irving, J. Stringer, and D. P. Whittle, Oxid. Met. 9, 427, 1975.
8. G. R. Wallwork and A. Z. Hed, Oxid. Met. 3, 171, 1971.
9. G. C. Wood and M. G. Hobby, Proc. 3rd Int. Cong. on Metallic Corrosion, Moscow, p. 102, 1966.
10. C. S. Wukusick and J. F. Collins, Mat. Sci. Stand., 637, 1964.
11. D. Delaunay and A. M. Huntz, J. Mater. Sci. 18, 189, 1983.
12. I. Pfeiffer, Z. Metallkunde, 53, 309, 1962.
13. K. Natesan, K. Klug, D. Renusch, B. W. Veal, and M. Grimsditch, Microstructural and Mechanical Characterization of Alumina Scales Thermally Developed on Iron Aluminide Alloys, Argonne National Laboratory Report ANL/FE-96/01, 1996.
14. K. Natesan and P. F. Tortorelli, Proc. Intl. Symp. on Nickel and Iron Aluminides: Processing, Properties, and Applications, ASM International, p. 265, 1997.

15. K. Natesan, in Proc. 7th Annual Conf. Fossil Energy Materials, ORNL/FMP-93/1, p. 249, 1993.

16. K. Natesan and W. D. Cho, in Proc. 8th Annual Conf. Fossil Energy Materials, ORNL/FMP-94/1, p. 227, 1994.

17. K. Natesan and R. N. Johnson, in Proc. 2nd Int. Conf. Heat-Resistant Materials, K. Natesan, P. Ganesan, and G. Lai, eds., p. 591, ASM International, Materials Park, OH, 1995.

18. P. F. Tortorelli and J. H. DeVan, Mater. Sci. and Eng., A153, 573, 1992.

19. K. Natesan, Materials at High Temperatures, 11, 36, 1993.

THE MICROSTRUCTURE AND MECHANICAL RELIABILITY OF ALUMINA SCALES AND COATINGS

K. B. Alexander, K. Prüßner, and P. F. Tortorelli

Oak Ridge National Laboratory
P. O. Box 2008
Oak Ridge, Tennessee 37831-6376

ABSTRACT

Alumina scales on iron-aluminides (Fe_3Al-based) and NiCrAl-based alloys were characterized in order to develop the knowledge to control the oxidation performance of alloys by controlling the microstructure and microchemistry of their scales. Plasma-deposited amorphous alumina coatings on iron-aluminides were used to study phase transformations, transport processes in the scales and sulfur segregation to the scale/metal interface. It was found, that during heat treatment in the absence of oxidation, amorphous coatings first transform to γ-Al_2O_3 and eventually α-Al_2O_3 nucleates at the scale/metal interface. Sulfur from the Zr-free alloy segregates to the scale/metal interface during heat treatment. Thermally-grown scales on Zr-doped iron-aluminides were compared to those formed after oxidation of a specimen with an alumina coating. Microstructural and gravimetric results showed that the primarily amorphous alumina coating promoted the nucleation and growth of metastable alumina phases, which resulted in more rapid oxidation. The thermally-grown oxide was found on top of the coating. The NiCrAl-based alloys formed columnar alumina scales underneath a layer of mixed oxides. Segregation of alloying elements like Y, Hf and Ta was found at both oxide grain boundaries and scale/metal interfaces.

INTRODUCTION

In many high-temperature fossil energy systems, corrosion and deleterious reactions with gases and condensable products in the operating environment often compromise materials performance. The presence of a stable surface oxide can effectively protect the materials from these reactions if the oxides are slow-growing, dense and adherent to the substrate. However, the various factors which control the scale/coating integrity and adherence are not fully understood. Of fundamental interest is the microstructure and microchemistry of the metal/oxide interface as well as oxide/oxide grain boundaries in the scale itself. In alumina scales, segregation of sulfur to the scale/metal interface was found to be detrimental to the oxidation performance, however the presence of reactive elements (RE) such as Y or Zr in the alloy can mitigate the effects of sulfur and thus improve the scale adherence.[1-5] Reactive elements segregate to the oxide/metal interface and scale grain boundaries and modify the growth mechanisms and the microstructure.[6,7]

The Oak Ridge National Laboratory (ORNL) research described in this paper is being conducted in collaboration with work sponsored by the Department of Energy's Office of Fossil Energy at Argonne National Laboratory (ANL) and Lawrence Berkeley National Laboratory (LBNL) as well as in concert with on-going interactions that are part of the Office of Basic Energy Sciences' Center of Excellence for the Synthesis and Processing of Advanced Materials. The Center of Excellence on Mechanically Reliable Surface Oxides and Coatings includes participants from ORNL, ANL, LBNL, Idaho National Engineering Laboratory (INEL) and Lawrence Livermore National Laboratory (LLNL).

This report will discuss work on the oxidation of iron aluminides, with and without alumina coatings, as well as recent work on the oxidation and segregation behavior of NiCrAl-based alloys. Iron-aluminides (Fe_3Al-type) are known to have good oxidation resistance, if the protective alumina scale can be maintained. It has been shown that small amounts of zirconium significantly reduce the oxidation rate and improve scale adherence in short-term tests at 1000°C.[8,9] Zirconium-containing alloys form unconvoluted, uniform oxide scales with no evidence of spallation during thermal cycling, whereas a significant amount of spallation is observed after thermal cycling of a Zr-free alloy.[8,9] The influence of an applied coating on the oxidation behavior of the alloy should allow the operative transport mechanisms during oxidation to be better examined. The deposition of a plasma-synthesized alumina coating prior to oxidation promoted the growth of metastable aluminas and thus increased the oxidation rate.[10] Both coated and uncoated specimens have needle-like surface morphologies.[10]

Unlike iron-aluminides, NiCrAl-based alloys can result in complex oxide scales with mixed oxides formed in the initial oxidation stages and an alumina layer underneath.[12,13] NiCrAl-based alloys of different compositions, including a commercial superalloy as well as two model alloys were part of the study. Such alloys allow extension of the present work on alumina scales and coatings on Fe-based alloys to a class of Ni-based alloys that are of direct relevance to advanced turbine systems.

EXPERIMENTAL PROCEDURES

The alloys used for the iron aluminide studies were FAL (Fe-28 at. % Al-5 at. % Cr-0.1 at. % Zr + 0.05 at. B) and FA186 (Fe-28 at. % Al-5 at. % Cr), prepared by arc melting and casting. The bulk alloy sulfur content was ~ 40 ppm for both alloys. These alloys were rolled to a final thickness of between 0.8 and 1.3 mm and rectangular specimens (typically 12 x 10 mm) were prepared from these sheets for coating and oxidation studies.

Oxidation experiments of coated or uncoated iron-aluminides were performed under isothermal and cyclic conditions for 96 h at 1000°C in static air. Gravimetric data were recorded during the cyclic oxidation by exposing coupons in individual pre-annealed alumina crucibles to a series of 24-h exposures. Heat treatments of deposited alumina coatings were performed for 0.5 and 2 h in He at 1000°C.

Alumina coatings on iron aluminides were deposited using a magnetically-filtered cathodic-arc plasma-synthesis process.[13] During the deposition process, the substrate was pulse-biased to a high ion energy (2 kV) in the initial phase of the deposition process to provide atomic mixing of the substrate and film at the interface. A substantially lower energy (0.2 kV) was used to deposit the remaining thickness of the coating.

Three NiCrAl-based alloys of different compositions (commercial superalloy René N5 (from General Electric Aircraft Engines), and ytrrium-doped ternary alloys with similar (NCA-S) as well as higher Cr and Al contents (NCA-H) - Table 1), which form complex oxide scales, were examined after isothermal oxidation in air at 1200°C for 100 h.

Table 1: Composition of NiCrAl-alloys (at %; except S in ppm)

at %	Ni	Cr	Al	Fe	Ta	Hf	W	Re	Si	Co	Mo	Y	Zr	S*	C
Rene N5	64.9	7.8	13.9	0.1	2.1	0.05	1.6	1.0	0.15	7.3	0.9	0.003	0.003	4	0.25
NCA-S	80.1	7.2	12.5	0.01					0.14			0.012		18	0.05
NCA-H	71.2	9.9	18.8	0.01					0.02			0.041		16	0.04

* sulfur contents in ppm

For all experiments, scanning electron microscopy (SEM) was performed on oxidized or heat treated coupons as well as on polished cross-sections through the scale and/or coatings. Field emission gun transmission electron microscopy/scanning transmission electron microscopy (FEG-TEM/STEM) of cross-sectional and plan-view specimens were used for the microstructural characterization of the scales. Energy dispersive x-ray spectroscopy (EDS) with high spatial resolution (1-2 nm probe) was used for the STEM studies of interfacial segregation.

RESULTS AND DISCUSSION

I. Oxidation Studies on Iron-Aluminides

1. Microstructure of Plasma-Deposited Alumina Coatings, As-Deposited

Plasma-deposited alumina coatings which were subsequently used for oxidation and segregation studies of iron-aluminides were primarily amorphous in the as-deposited state (as determined by x-ray diffraction). Auger Electron Spectroscopy (AES) and Rutherford Backscattering (RBS) analyses showed that the films are slightly cation-deficient Al_2O_3.[14] Cross-sectional TEM showed that most coatings had two distinctly different layers: an inner layer which exhibits contrast features perpendicular to the interface and an outer layer, which is featureless (Fig. 1).

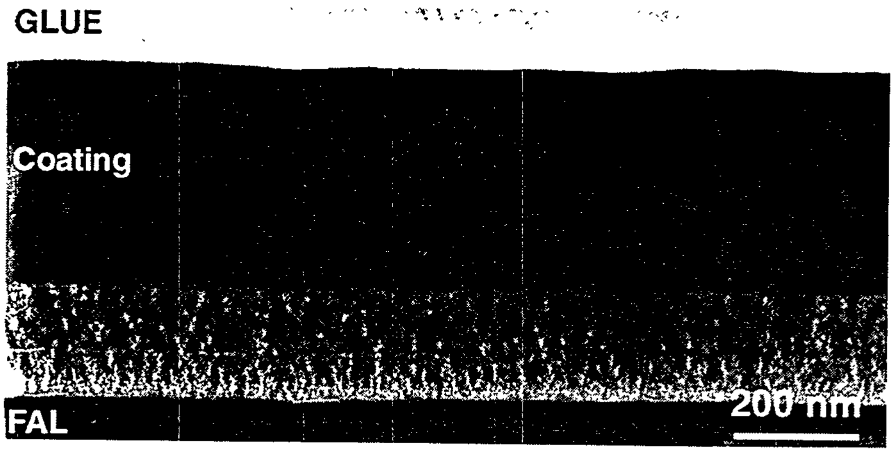

Fig. 1. TEM image of the structure of an as-deposited alumina coating (~ 0.7 μm thick).

The featureless portion was found by selected area diffraction (SAD) to be fully amorphous, whereas some fine-grained γ-Al_2O_3 was found in the inner part of the scale. The difference between the two regions was assumed to correlate with the change in pulse-biasing of the substrate from 2 kV to 0.2 kV during deposition. However, not all the coatings had these two layers. Further investigation of deposition parameter/structure correlations are underway.

2. Microstructural Development and Segregation During Heat Treatment of Alumina Coatings

Previous experiments concerning the segregation of sulfur to the scale/metal interface have only addressed segregation to interfaces between thermally-grown α-Al_2O_3 and an alloy.[3,4,15,16] Since α-Al_2O_3 grows by inward diffusion, the interface is not static but moving into the metal during oxidation. Therefore diffusion of sulfur to the interface and migration of the interface in the opposite direction are counter-processes. In this study, alumina coatings (0.2 and 0.8 µm thick), plasma-deposited on FA 186, were used to study the segregation of sulfur to a static scale/alloy interface (in the absence of thermal oxidation) and thereby isolate the effect.[16] As-deposited alumina coatings were heat treated in a He-atmosphere at 1000°C (for 0.5 or 2 h) in order to crystallize the initially amorphous coating, while preventing the growth of a thermal oxide scale (if thermal oxidation occurs, oxide needles can clearly be seen on the coating surface by SEM, and this was not observed).

SEM imaging revealed that although the scale/gas interface remained smooth during crystallization, the scale/metal interface showed imprints of distinct oxide grains with associated cracks and cavities as shown in Fig. 2a. The 0.8 µm coating developed a network of cracks and spalled in several areas. The 0.2 µm coating didn't develop these large through-coating cracks. It can be concluded that for the 0.8 µm coating the critical scale thickness for accomodation of thermal and growth/transformation stresses was exceeded.

TEM investigations showed that the heat treatment resulted in the transformation of the coating to metastable alumina (γ-Al_2O_3 and θ-Al_2O_3) and eventually to the nucleation of α-Al_2O_3 at the scale/metal interface (Fig. 3). During the transformation to the metastable aluminas, both interfaces remained fairly flat. The formation of α-Al_2O_3 on the other hand, resulted in roughening of the scale/metal interface. The grains visible as imprints in the top-down SEM images (Fig. 2) could be correlated to faceted grains of α-Al_2O_3 which grew into the alloy. Cavities were formed next to the α-Al_2O_3 (Fig. 3b). Therefore considerable material transport seems to be associated with the phase transformation to α-Al_2O_3 although no thermal oxide growth occurs.

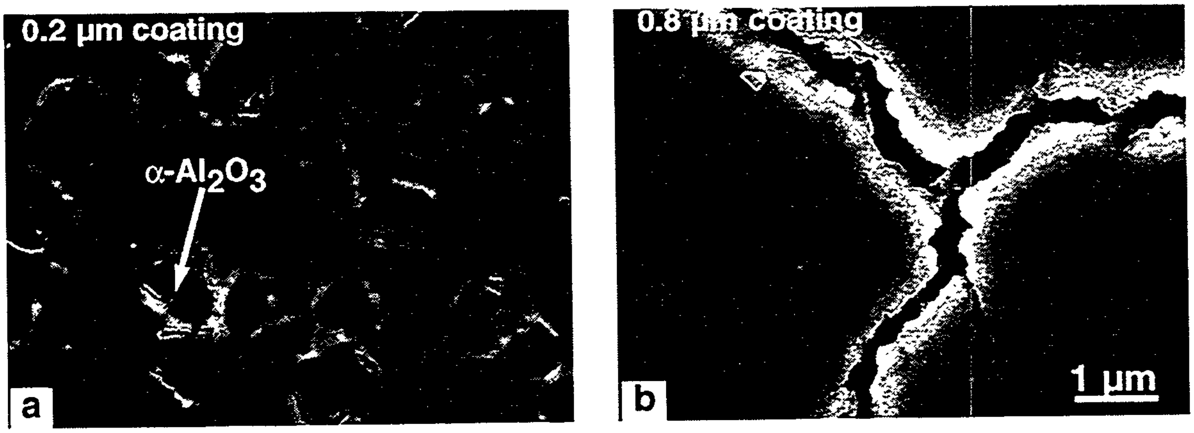

Fig. 2. SEM plan-views of the heat-treated coatings after 2 h in He at 1000°C. (a) 0.2 µm coating, revealing the scale/metal interface (b) 0.8 µm coating, revealing the gas/scale interface.

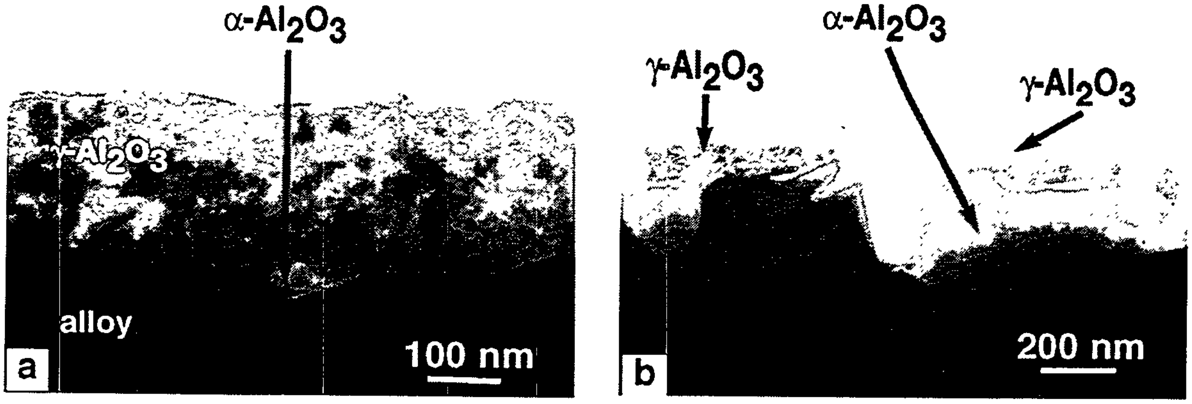

Fig. 3. (a) and (b) TEM cross-sections through heat-treated 0.2 μm thick coating after 2 h in He at 1000°C.

Studies with Auger electron spectroscopy (AES) on FA186/alumina coating interfaces that were freshly exposed by an in-situ scratch-technique, showed that sulfur segregated to the oxide/metal interface during the heat treatment.[16] The sulfur coverage of the interface increased with increasing annealing time and varied in different regions of the specimen. In order to study the correlation between different interface structures and the sulfur level at the interface, high spatial resolution EDS analysis of TEM cross sections was used. Segregation of sulfur was found at α-Al_2O_3/alloy interfaces as well as at γ-Al_2O_3/alloy interfaces (Fig. 4). No interfacial voids were observed in these areas. Quantification of these data is complicated by the roughness of the γ-Al_2O_3/alloy interface (in contrast to the facetted α-Al_2O_3/alloy interface) which made edge-on orientation of the interface impossible. Further analysis is underway to determine if the interfacial sulfur coverage is different for the two microstructures.

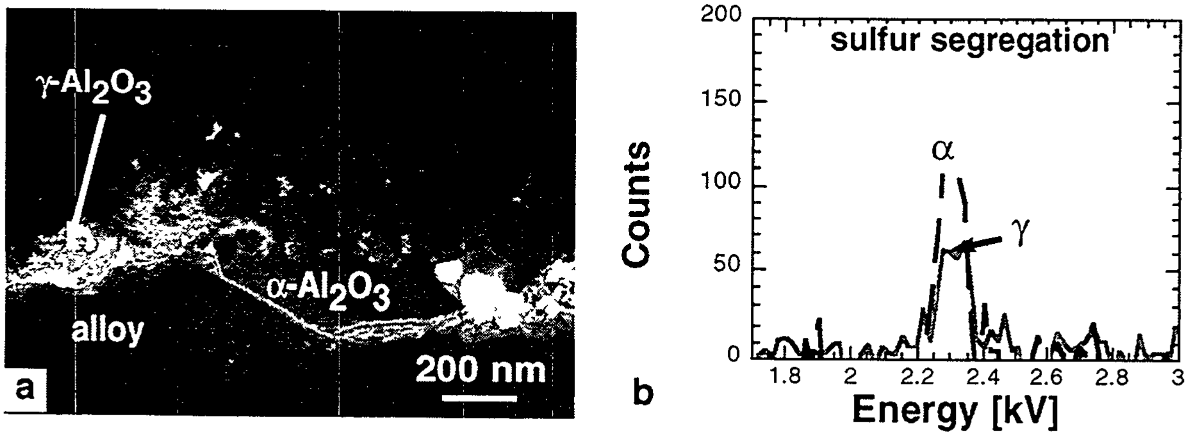

Fig. 4. a) STEM annular dark-field image of γ/alloy and α/alloy interface, b) EDS spectra showing segregation of sulfur at the γ/alloy and the α/alloy interface.

3. Influence of Alumina Coatings on Thermal Oxide Growth on Iron-Aluminides

To study the effect of an alumina coating applied prior to oxidation on the oxidation performance of iron-aluminides, FAL was coated on one side with a 0.1 µm alumina coating and oxidized in air at 1000°C for 96 h. On both the coated and the uncoated sides, oxide scales with a needle-like surface structure were formed (Fig. 5). Both oxide scales were adherent and did not spall. The recorded weight gain demonstrated that the coating increased the rate of oxidation. The oxide scale on the coated side was 1.5-2 µm thick, whereas on the uncoated side it was 0.8-1 µm (Fig. 6).

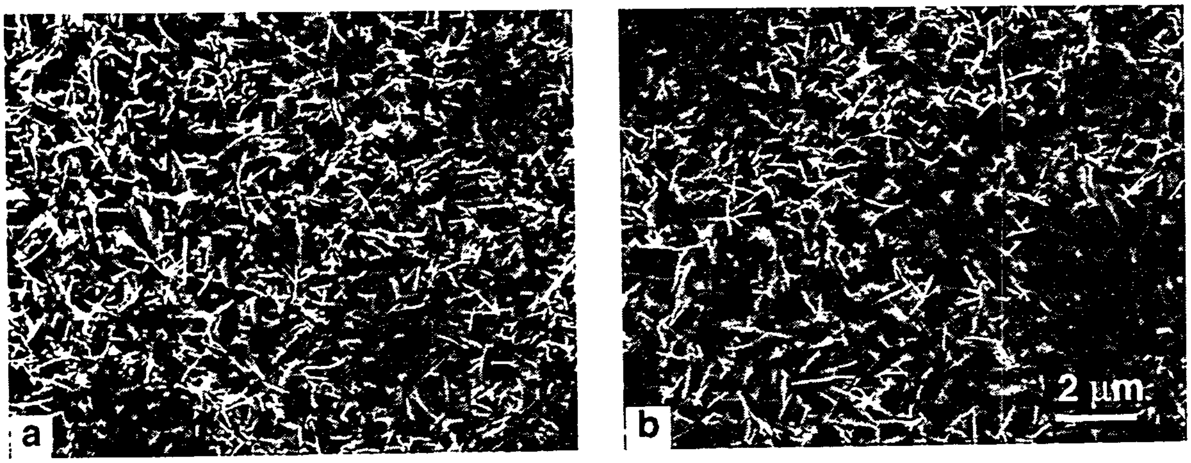

Fig. 5. SEM plan-view of oxidized surfaces exposed 96 h at 1000°C, a) FAL uncoated, b) FAL with 0.1 µm alumina coating.

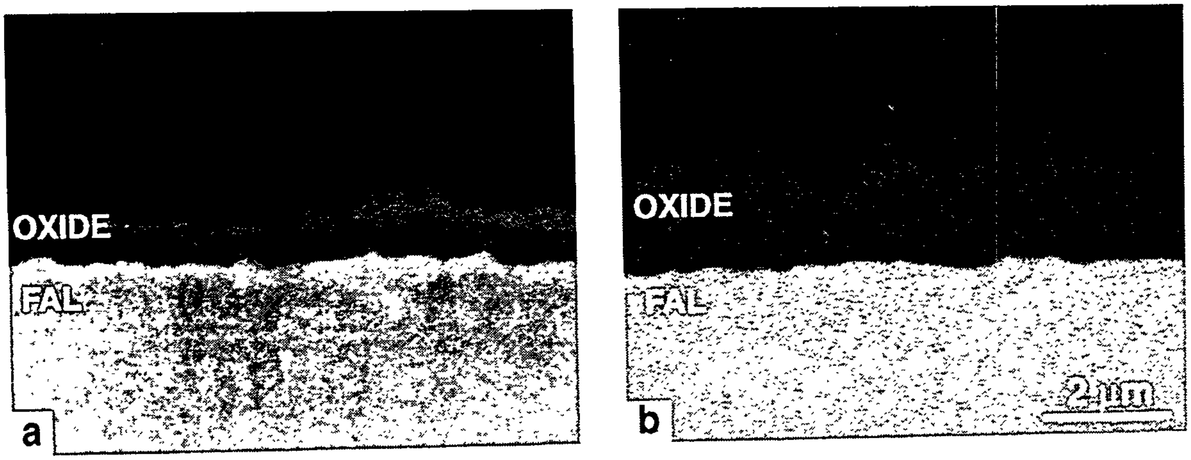

Fig. 6. SEM of polished cross-section after oxidation for 96 h at 1000°C, a) FAL uncoated, b) FAL with 0.1 µm alumina coating.

On the coated side, the original location of the coating can be discerned in the TEM cross-section shown in Fig. 7. The grain size in the area of the original coating is typically 100-150 nm. The grains were identified as nearly dense, equiaxed α-Al_2O_3. The thermally-grown oxide on top of the coating was also α-Al_2O_3 however, it had a much coarser grain structure. Selected-area diffraction showed all portions of the oxide scale, even the oxide needles at the scale/gas interface were α-Al_2O_3, consistent with the pseudomorphic transformation of the transient oxides to α-Al_2O_3 after 96h at 1000°C.

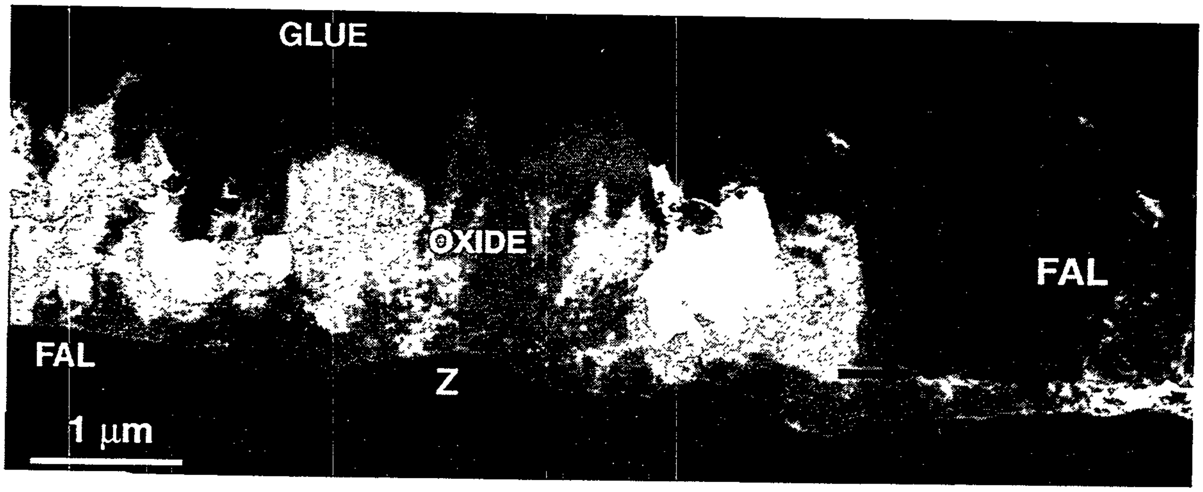

Fig. 7. STEM annular dark-field of coated-and-oxidized (96h at 1000°C) FAL. The location of the original coating is indicated by the arrow.

The identification of the original coating location in the bottom portion of the scale after oxidation implies that most of the scale growth on coated FAL occurred primarily by transport of aluminum through the coating. Although the scale/metal interface on the coated FALwas intact, it roughened during oxidation. This indicates that some transformation of α-Al_2O_3 at the metal/coating interface occurred (similar to that described in the previous section). On the coated surface, Zr-rich metallic particles (typical size: 0.5-1 μm) were found at the scale/metal interface (marked "Z" in Fig. 7). The particles at the scale/metal interface were, compared to the FAL alloy, rich in Zr but contained less Fe and Cr and no oxygen (as determined by STEM/EDS analysis). These particles were not observed at the scale/metal interface in the absence of the alumina coating. The fact that the Zr was not oxidized is consistent with the lack of inward diffusion of oxygen. It is proposed that the amorphous coating promotes the nucleation and growth of metastable alumina phases, resulting in slighly enhanced outwardly-growing oxidation and thicker scales. During the early stages of oxidation, the amorphous coating is therefore ineffective as a protective layer.

Fig. 8. Annular dark-field STEM image of cross-section through scale showing ZrO_2 particles within the scale.

Elemental analysis by EDS showed that zirconium segregated to oxide grain boundaries, both in the initial alumina coating and in the thermally-grown oxide. Segregation of zirconium at the scale/metal interface was also found, both in the coated and uncoated FAL. Auger analysis on metal/oxide interfaces exposed by scratching off the oxide in vacuo revealed the absence of sulfur at the metal/oxide interface.[14] In the portion of the scale near where the amorphous coating was originally located, ZrO_2 particles were found at grain boundaries as well as at the interface between the former coating and the thermally-grown oxide (Fig. 8). The formation of ZrO_2 particles within the oxide on coated-and-oxidized FAL must result from diffusion of zirconium into the coating and subsequent oxidation and/or formation of ZrO_2 during the growth of new oxide.

II. Oxidation Studies on NiCrAl-Alloys

Plan-view images of the three alloys after oxidation are shown in Fig. 9. Figure 10 shows the corresponding cross sections (polished or fractured). The oxide scale on René N5 (~5 µm) consists of columnar α-Al_2O_3 at the bottom (~4 µm) and a mixed layer of spinel (Ni, Co, Ta)(Al, $Cr)_2O_4$ and α-Al_2O_3 (~1 µm) at the top. The mixed oxide layer contains numerous precipitates of Ta,Y,Cr(Hf,Re)-oxides. These are concentrated at the interface between the columnar alumina and the mixed layer. This mixed layer of the scale is prone to spallation.

Similar oxide particles can also be found on the scale surface. Spallation of the complete scale exposing the bare alloy occurs only around particles in the alloy, which consist of Ta,Y,Cr(Hf,Re)-oxide in the center, surrounded by spinel (Ni, Co, Ta) (Al, $Cr)_2O_4$ and α-Al_2O_3. Using STEM/EDS analysis segregation of Ta and Y at oxide grain boundaries both in the alumina and in the spinel was found. Some oxide grain boundaries also exhibited segregation of Hf and Re.

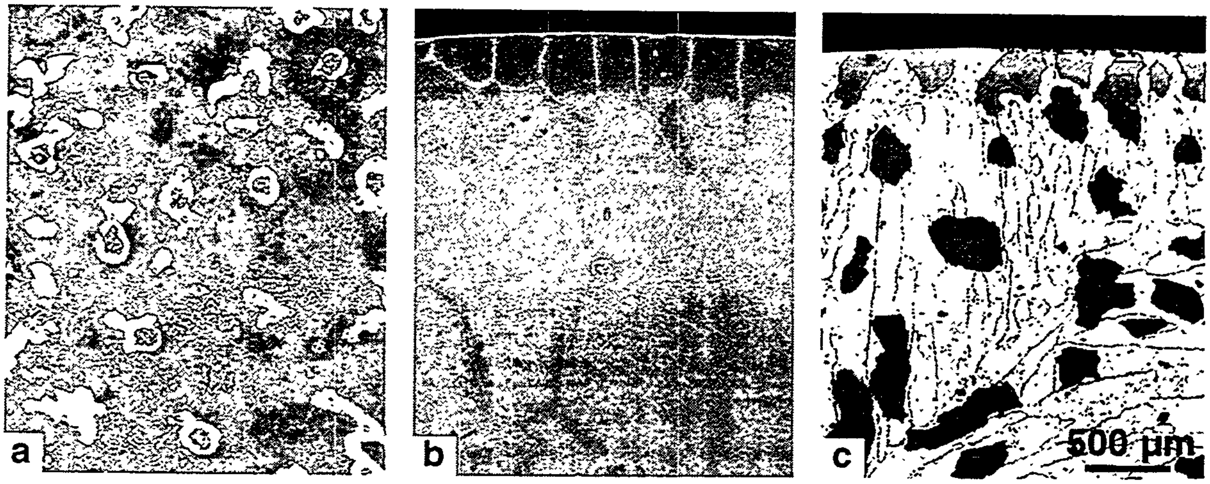

Fig. 9. SEM plan-view images of a) René N5, b) NCA-S and c) NCA-H after oxidation for 100 h at 1200°C.

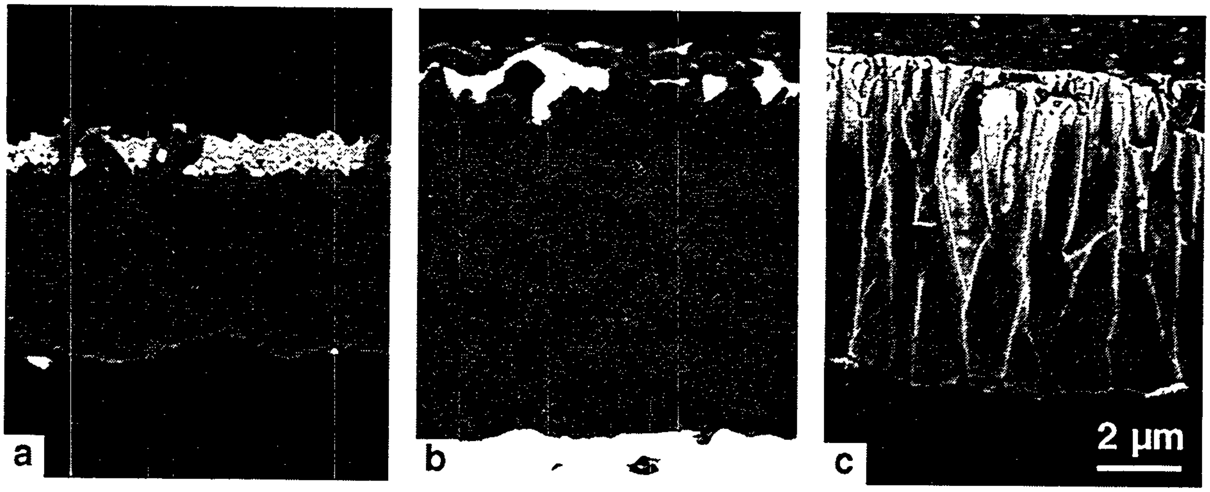

Fig. 10. SEM images of cross-sections of a) René N5, b) NCA-S and c) NCA-H after oxidation for 100 h at 1200°C.

On NCA-S, the scale (~9 µm) consists mainly of columnar Cr-doped α-Al_2O_3. The grain structure of the scale resembles that found on many reactive-element-doped alumina formers (e.g. - Refs. 6, 7, 18) and indicates alumina growth primarily by inward oxygen diffusion.[17] A thin, porous mixed layer of equiaxed spinel ($NiAl_2O_4$) and α-Al_2O_3, as well as some NiO formed on top of the alumina. Over time, NiO transforms to $NiAl_2O_4$ which eventually transforms to α-Al_2O_3; both transformations are pseudomorphic. Spallation of the scale occurred only in a few areas associated with the formation of Y_2O_3, $Y_3Al_5O_{12}$ (garnet) and α-Al_2O_3 at Y-rich alloy grain boundaries. Yttrium-rich oxide particles can be found on the scale surface. Using STEM/EDS analysis, yttrium was also found to be segregated at oxide grain boundaries and at the scale/metal interface.

The NCA-H alloy forms an oxide scale (~8 μm) that consists mainly of columnar Cr-doped α-Al_2O_3. Y-rich oxide particles can be found on the scale surface. The higher level of Y in this alloy results in the formation of Y-rich precipitates at all alloy grain boundaries. Preferential internal oxidation ultimately leads to the formation of Y_2O_3, $Y_3Al_5O_{12}$ (garnet) and α-Al_2O_3 at these grain boundaries. Due to the volume change and thermal mismatch associated with the formation of these phases, almost complete spallation of the oxide scale is initiated at these sites.

SUMMARY AND CONCLUSIONS

Alumina scales on iron-aluminides (Fe_3Al-based) and NiCrAl-based alloys were characterized in order to understand the relationship between the oxidation performance of alloys and the microstructure and microchemistry of their scales. Plasma-deposited amorphous alumina coatings on iron-aluminides were used to study phase transformations, transport processes in the scales and sulfur segregation to the scale/metal interface. It was found, that during heat treatment in the absence of oxidation, amorphous coatings first transform to γ-Al_2O_3 and eventually α-Al_2O_3 nucleates at the scale/metal interface. Sulfur from the Zr-free alloy segregates to the scale/metal interface during heat treatment. Thermally-grown scales on Zr-doped iron-aluminides were compared to those formed after oxidation of a specimen with an alumina coating. Microstructural and gravimetric results showed that the primarily amorphous alumina coating promoted the nucleation and growth of metastable alumina phases, which resulted in more rapid oxidation. The thermally-grown oxide was found on top of the coating. The NiCrAl-based alloys formed columnar alumina scales underneath a layer of mixed oxides. Segregation of alloying elements like Y, Hf and Ta was found at both oxide grain boundaries and scale/metal interfaces. The results from both alloy systems are consistent with previous results on primary alumina-formers. Reactive elements present in the alloy diffuse into the oxide scale and segregate to grain boundaries where they change the diffusion processes resulting in a columnar grain structure of the alumina scale.

ACKNOWLEDGMENT

The authors thank M. Howell for experimental support, B.A. Pint and I.G. Wright for technical discussions and E. A. Kenik for review of the manuscript. This research was sponsored by the Fossil Energy Advanced Research and Technology Development (AR&TD) Materials Program and the Division of Materials Science, U S. Department of Energy, DE-AC05-96OR22464 with Lockheed Martin Energy Research Corp. Research was performed in part with the SHaRE User Facilities at ORNL.

REFERENCES

1. J.G. Smeggil, A.W. Funkenbusch, N.S. Bornstein, Met. Trans. 17A (1986) 923.
2. E. Schumann, J.C. Yang, M.J. Graham and M. Rühle, Oxid. Met. 46 (1996) 37.
3. E. Schumann, Scripta Mater. 34 (1996) 1365.
4. C. Mennicke, E. Schumann, C. Ulrich and M. Rühle, Mat. Sci. Forum (1996) in press.
5. G.H. Meier, F.S. Pettit and J.L. Smialek, Mat. Corr. 46 (1995) 232.
6. B.A. Pint, Oxid. Met. 45 (1996) 1.
7. B.A. Pint and K.B. Alexander, submitted to J. Electrochem. Soc.
8. P.F. Tortorelli and K.B. Alexander, pp. 247-56 in *Proc. Ninth Annual Conf. Fossil Energy Materials*, N.C. Cole and R.R. Judkins (comp.), CONF-9505204, U. S. Department of Energy, August 1995.
9. P.F. Tortorelli and J.H. DeVan, pp. 257-70 in Processing, Properties, and Applications of Iron Aluminides, J.H. Schneibel and M.A. Crimp (eds.), The Minerals, Metals, and Materials Society, Warrendale, PA, 1994.
10. K.B. Alexander, K. Prüßner, P.Y. Hou and P.F. Tortorelli, 3rd Int. Conf. Microscopy of Oxidation, The Institute of Metals, London(1996) in press.
11. C.S. Giggins and F.S. Pettit, J. Electrochem. Soc. 118 (1971) 1782.
12. A. Kumar, M. Nasrallah and D.L. Douglass, Oxid. met. 8 (1974) 227.
13. I.G. Brown and Z. Wang, Proc. Ninth Annual Conf. Fossil Energy Materials, U.S. Department of Energy (1995) 239.
14. P.Y. Hou, Z. Wang, K. Prüßner, K.B. Alexander and I.G. Brown, 3rd Int. Conf. Microscopy of Oxidation, Cambridge (1996) in press.
15. P. Fox, D.G. Lees and G.W. Lorimer, Oxid. Met. 36 (1991) 491.
16. K. Prüßner, E. Schumann and M. Rühle, pp. 344-56 in Fundamental Aspects of High Temperature Corrosion, D. A. Shores, R. A. Rapp, and P. Y. Hou (eds.), Proc. Vol. 96-26, The Electrochemical Society, Pennington, New Jersey, 1997.
17. B. A. Pint, pp. 74-85 in Fundamental Aspects of High Temperature Corrosion, D. A. Shores, R. A. Rapp, and P. Y. Hou (eds.), Proc. Vol. 96-26, The Electrochemical Society, Pennington, New Jersey, 1997

MICROSTRUCTURAL AND MECHANICAL PROPERTY CHARACTERIZATION OF INGOT METALLURGY ODS IRON ALUMINIDE

V. K. Sikka and C. R. Howell

and

F. Hall* and J. Valykeo*

ABSTRACT

This paper deals with a novel, lower cost method of producing a oxide dispersion strengthened (ODS) iron-aluminide alloy. A large 250-kg batch of ODS iron-aluminide alloy designated as FAS was produced by Hoskins Manufacturing Company (Hoskins) [Hamburg, Michigan] using the new process. Plate and bar stock of the ODS alloy were the two major products received. Each of the products was characterized for its microstructure, including grain size and uniformity of oxide dispersion. Tensile tests were completed from room temperature to 1100°C. Only 100-h creep tests were completed at 800 and 1000°C. The results of these tests are compared with the commercial ODS alloy designated as MA-956. An assessment of these data is used to develop future plans for additional work and identifying applications.

INTRODUCTION

The Fe_3Al-based intermetallic alloys have been under development[1-5] at the Oak Ridge National Laboratory (ORNL) for a number of years. These alloys are attractive for coal gasification systems because of their excellent resistance[6] to high-temperature oxidation and sulfidation. To date, significant progress has been made in the development of alloy compositions with improved room-temperature ductility and high-temperature strength. However, the high-temperature strength at temperatures above 650°C continues to be a limiting factor in their applications to take full advantage of their excellent oxidation and sulfidation resistances. The oxide dispersion strengthening (ODS) is one possible method of improving the high-temperature strength of the iron aluminides. One method of producing the ODS materials is the attritor milling of alloy powder with Y_2O_3 powder, followed by consolidation, and grain-growth heat treatment. This method is the same as that used by Inco Alloys International, Inc. (Inco) [Huntington, West Virginia] to produce the commercial alloy MA-956. However, the cost

---

*Hoskins Manufacturing Company, 10776 Hall Road, Hamburg, Michigan.

of conventional processing of ODS materials is the limiting factor in their wide spread use. The purpose of this study was to ODS produce the Fe_3Al-based alloy by using an alternate low-cost method developed by Hoskins Manufacturing Company (Hoskins) [Hamburg, Michigan]. The low-cost method is designated as ingot metallurgy ODS iron aluminide. This paper will present the details of processing, microstructure, and properties of a heat of Fe_3Al-based alloy FAS that was ODS produced by Hoskins' method.

Processing

The Fe_3Al-based alloy FAS was chosen for this study. The FAS alloy consists of Fe-15.9 Al-2.2 Cr-0.01 B (weight percent) and has the best sulfidation resistance among the Fe_3Al-based alloys. A 500-kg heat of this alloy was prepared by air-induction melting at Hoskins. Table 1 is the chemical analysis of the heat which shows that it met the target composition extremely well. The alloy ingots were subsequently machined to remove any surface oxide and inert gas atomized to powder. The powder was blended with 0.5 wt % Y_2O_3 and processed by Hoskins' proprietary steps to billets that were subsequently processed to plate and bar. The plate was 15.9 mm thick, and the bar was 60.3 by 60.3 mm square with rounded corners. Figure 1 shows the plate and bar product received from Hoskins. The FAS + 0.5 wt % Y_2O_3 material is designated as 920 alloy, and its heat number is 21870.

A small section of the 15.9-mm plate was processed into 0.76-mm-thick sheet at ORNL. The processing steps consisted of hot rolling at 1100°C from 17.0 to 8.64 mm thickness, hot rolling at 800°C from 8.64 to 4.32 mm thickness, and warm rolling at 650°C from 4.32 to 0.76 mm thickness.

DISCUSSION OF CURRENT ACTIVITIES

The effort during this fiscal year continued to procure a large ingot metallurgy ODS iron-aluminide heat and characterize it for its mechanical and microstructural properties. The following activities were carried out and are briefly described below.

Testing Details

The 0.762-mm-thick sheet was die punched into 25.4-mm gage length tensile specimens. The specimens were tested after two heat treatments: 1 h at 700°C followed by oil quenching and 1 h at 1250°C in vacuum. Both sets of specimens were tensile tested from room temperature to 1000°C. Tensile specimens of 6.35 mm diam in the gage section were machined from the plate

Table 1. Comparison of target and check analyses of FAS alloy[a]

Element	Weight percent	
	Target	Powder
Al	15.9	16.0
Cr	2.2	2.17
B	0.01	0.010
C	--	0.014[b]
S	--	0.001[c]
Mo	--	0.01
Cb	--	<0.01
Zr	--	<0.01
N_2	--	0.005
O_2	--	0.030

[a] FAS alloy prepared by air-induction melting and used for oxide dispersion strengthening.

[b] Carbon was specified as 0.01 max.

[c] Sulfur was specified as 0.0020 max.

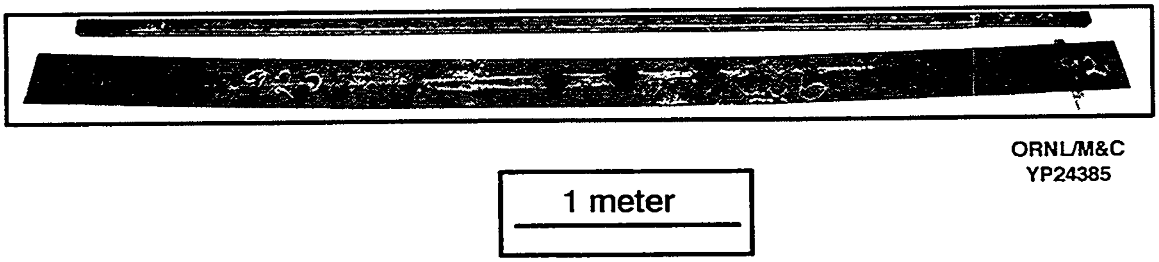

Figure 1. Hot-rolled plate and bar of 920 alloy. The plate is 15.9 mm thick by 210 mm wide, and the bar is 60.3 by 60.3 mm square with rounded corners.

and bar product. These were tensile tested in the as-hot rolled condition in the temperature range from room temperature to 1000°C. A limited number of creep tests were also conducted on the sheet, plate, and bar specimens. Optical and scanning electron microscopy were used to characterize the material.

Results

Tensile data on the sheet, plate, and bar are summarized in Table 2 and plotted in Figures 2 through 4. Data for the base FAS alloy is also included for comparison. These plots show the following:

1. The grain coursening treatment of 1250°C has a strong effect in reducing the room-temperature yield and ultimate tensile strengths. It also reduces the ductility by nearly 50%.
2. The large differences in yield strength between the grain coarsened sheet and the round specimens of plate and bar are associated with the specimen size.
3. The ultimate tensile strength, which is insensitive to the testing procedure, is more indicative of the true behavior. Data in Figure 3 shows that sheet has the highest strength in the fine-grained condition, which is reduced by the grain coarsening treatment of 1250°C for 1 h. The plate and bar of coarse-grained structure show even lower values at room temperature.
4. The yield and ultimate tensile strength properties are relatively unaffected by test temperatures of 600, 800, and 1000°C.
5. The room-temperature elongation is most affected by either grain coarsening treatment of the sheet or testing of coarse-grained hot-rolled plate and bar. It is interesting to note that the coarse-grained material has the highest ductility at temperatures $\geq$ 800°C and lowest at room temperature in comparison to fine-grained material that showed the highest ductility at room temperature and the lowest at $\geq$ 800°C. The elongation trends at intermediate temperatures of 600 and 800°C are not quite straightforward. In any event, the ductility at test temperatures of 600, 800, and 1000°C is sufficiently high to be of no concern.
6. At test temperatures of $\geq$ 600°C, the ODS produced material is consistently higher in strength than the base material. At 800°C, the yield and ultimate tensile strengths are higher by a factor of nearly two.

The creep rupture data for the sheet, plate, and bar are plotted as Larson Miller parameter in Figure 5 and shown in Table 3. Also included in this plot are the data for the base Fe_3Al alloys (FAS, FAL, and FA-129), a commercially produced mechanically alloyed MA-956 produced by Inco, and an ingot metallurgy Fe-Cr-Al-based ODS material (877) produced at Hoskins. This figure shows that while the Hoskins process significantly enhanced the creep properties of their Fe-Cr-Al alloy, it produced only a small effect for the FAS alloy. Note however that even though small, it is still a factor of nearly two improvement in creep rupture strength of the base FAS alloy.

Table 2. Tensile property data for 920 alloy (heat 21870) of FAS + 0.5 wt % Y_2O_3

Specimen no.	Test temperature (°C)	Heat treatment	Yield strength (MPa)	Tensile strength (MPa)	Total elongation (%)	Reduction of area (%)
2L[a]	23	Sheet Annealed 700°C/1 h OQ[b]	414	979	16.45	14.16
8L[a]	23	Sheet Annealed 1250°C/1 h Vacuum	370	775	7.37	8.84
14L[c]	23	Plate As rolled	515	578	2.18	2.23
22L[c]	23	Bar As rolled	491	572	1.91	3.34
4L[a]	600	Sheet Annealed 700°C/1 h Oq[b]	365	382	43.95	55.14
10L[a]	600	Sheet Annealed 1250°C/1 h Vacuum	356	402	42.00	62.80
15L[c]	600	Plate As rolled	394	399	46.53	70.04
23L[c]	600	Bar As rolled	386	393	59.84	77.76

Table 2. (Continued)

Specimen no.	Test temperature (°C)	Heat treatment	Yield strength (MPa)	Tensile strength (MPa)	Total elongation (%)	Reduction of area (%)
5L[a]	800	Sheet Annealed 700°C/1 h Vacuum	95	97	53.75	69.95
9L[a]	800	Sheet Annealed 1250°C/1 h	89	92	42.95	73.75
16L[c]	800	Plate As rolled	86	95	62.86	86.36
24L[c]	800	Bar As rolled	108	109	63.64	93.80
6L[a]	1000	Sheet Annealed 700°C/1 h OQ	17	20	79.30	81.99
11L[a]	1000	Sheet Annealed 1250°C/1 h Vacuum	18	18	102.10	71.80
17L[c]	1000	Plate As rolled	16	18	111.08	89.75
25L[c]	1000	Bar As rolled	17	18	111.20	--

[a] Strain rate: $3.33 \times 10^{-3} s^{-1}$.

[b] OQ = oil quenched.

[c] Strain rate: $2.67 \times 10^{-3} s^{-1}$.

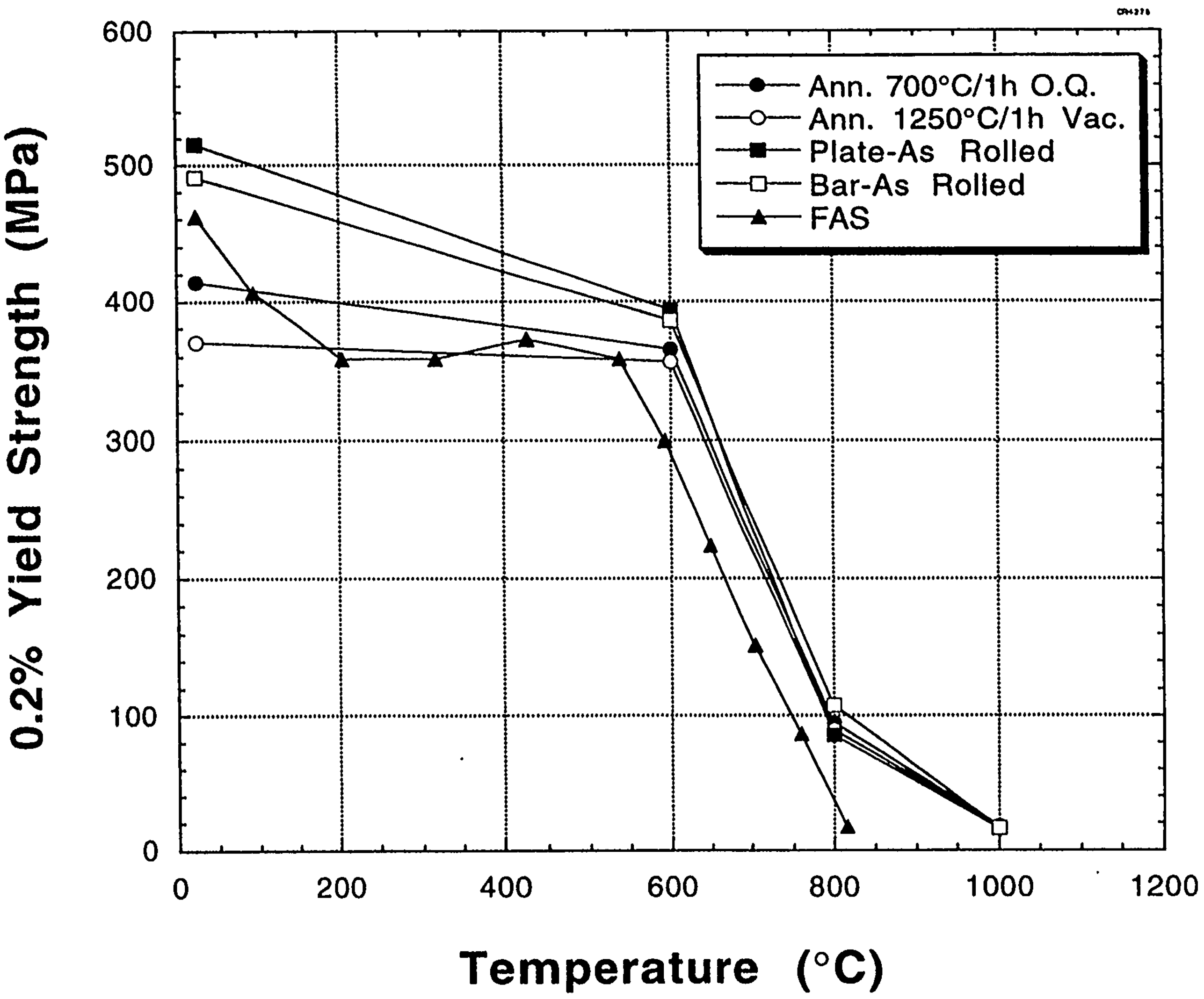

Figure 2. Yield strength (0.2% offset) as a function of test temperature for sheet, plate, and bar of 920 alloy.

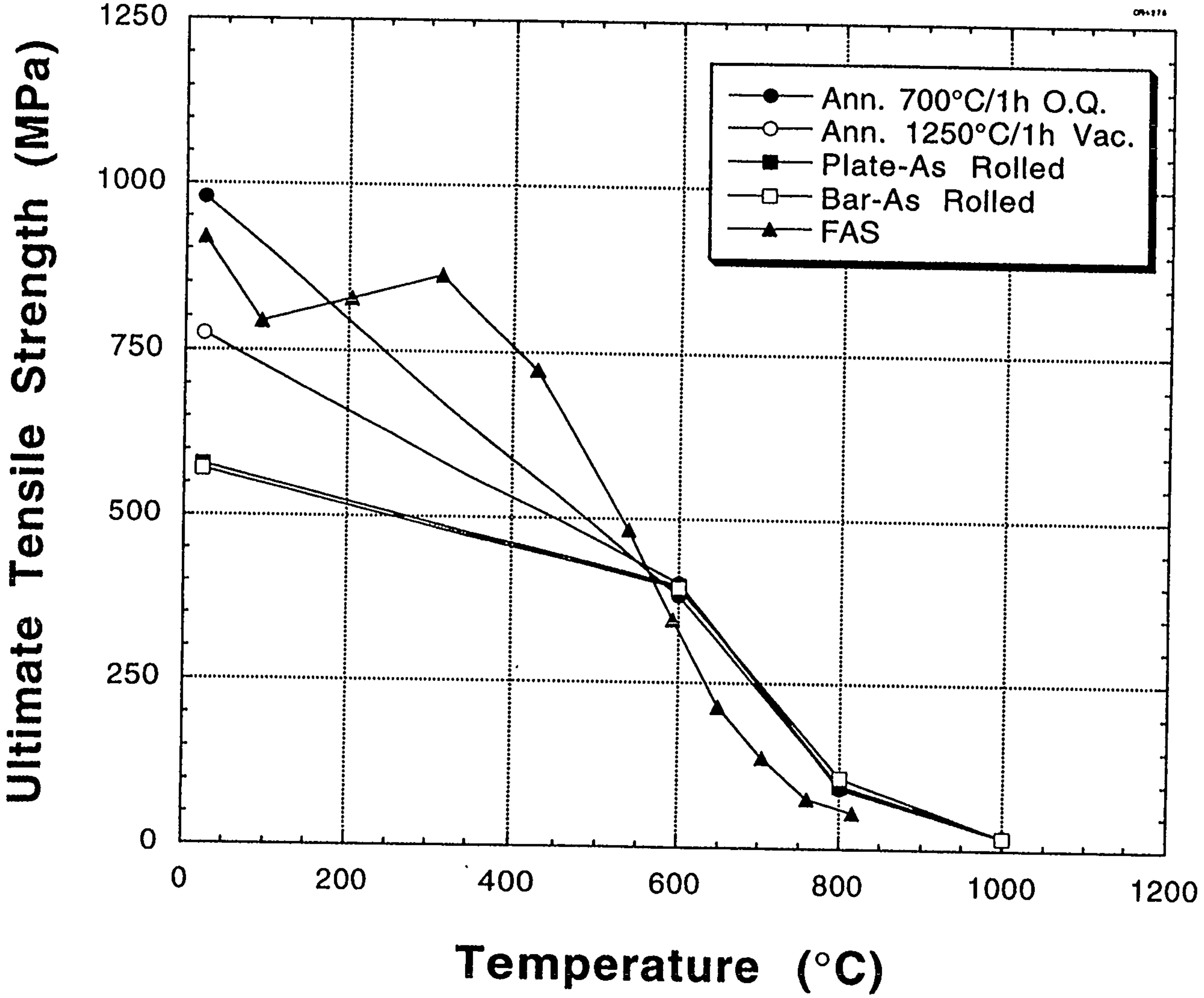

Figure 3. Ultimate tensile strength as a function of test temperature for sheet, plate, and bar of 920 alloy.

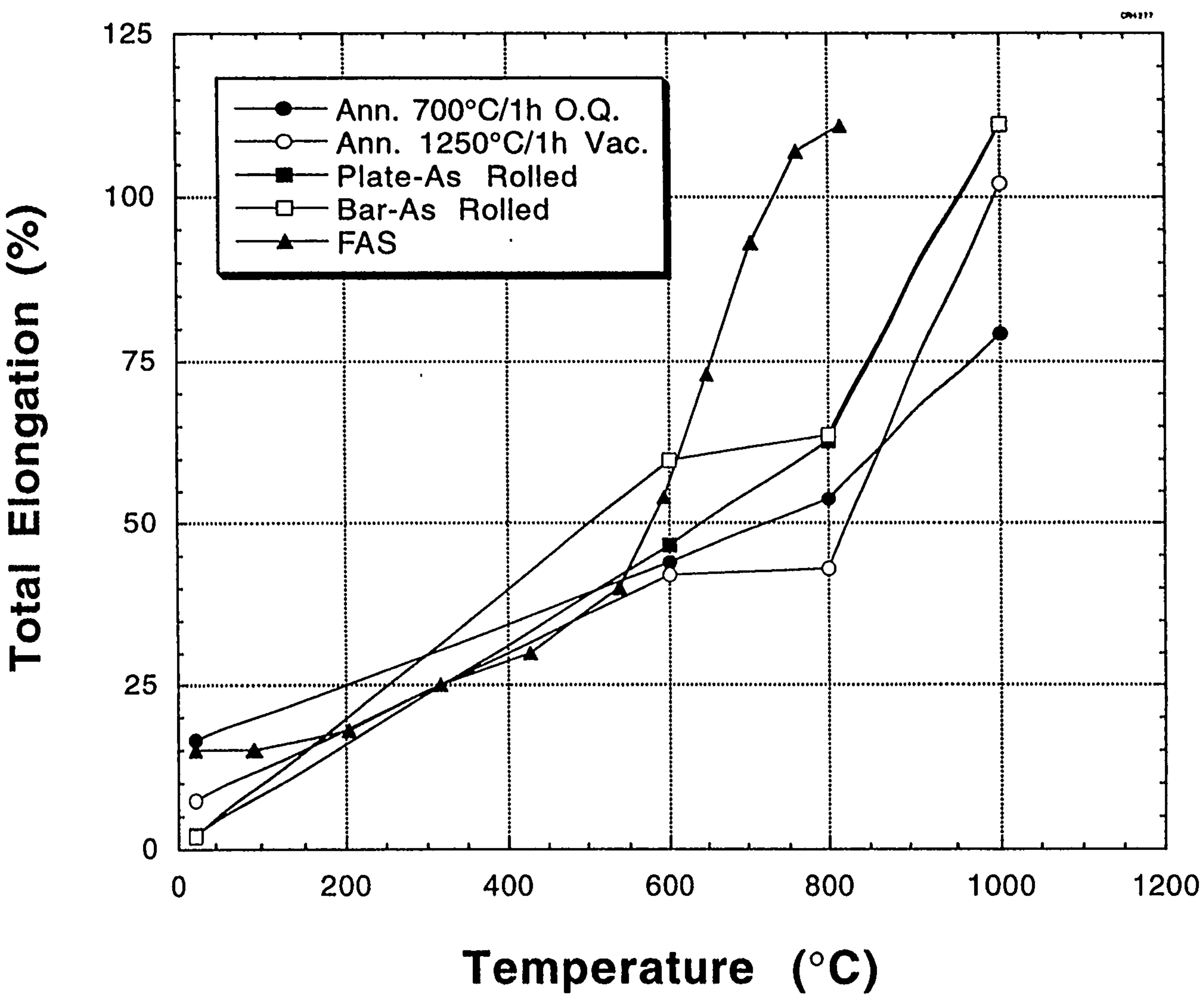

Figure 4. Total elongation as a function of test temperature for sheet, plate, and bar of 920 alloy.

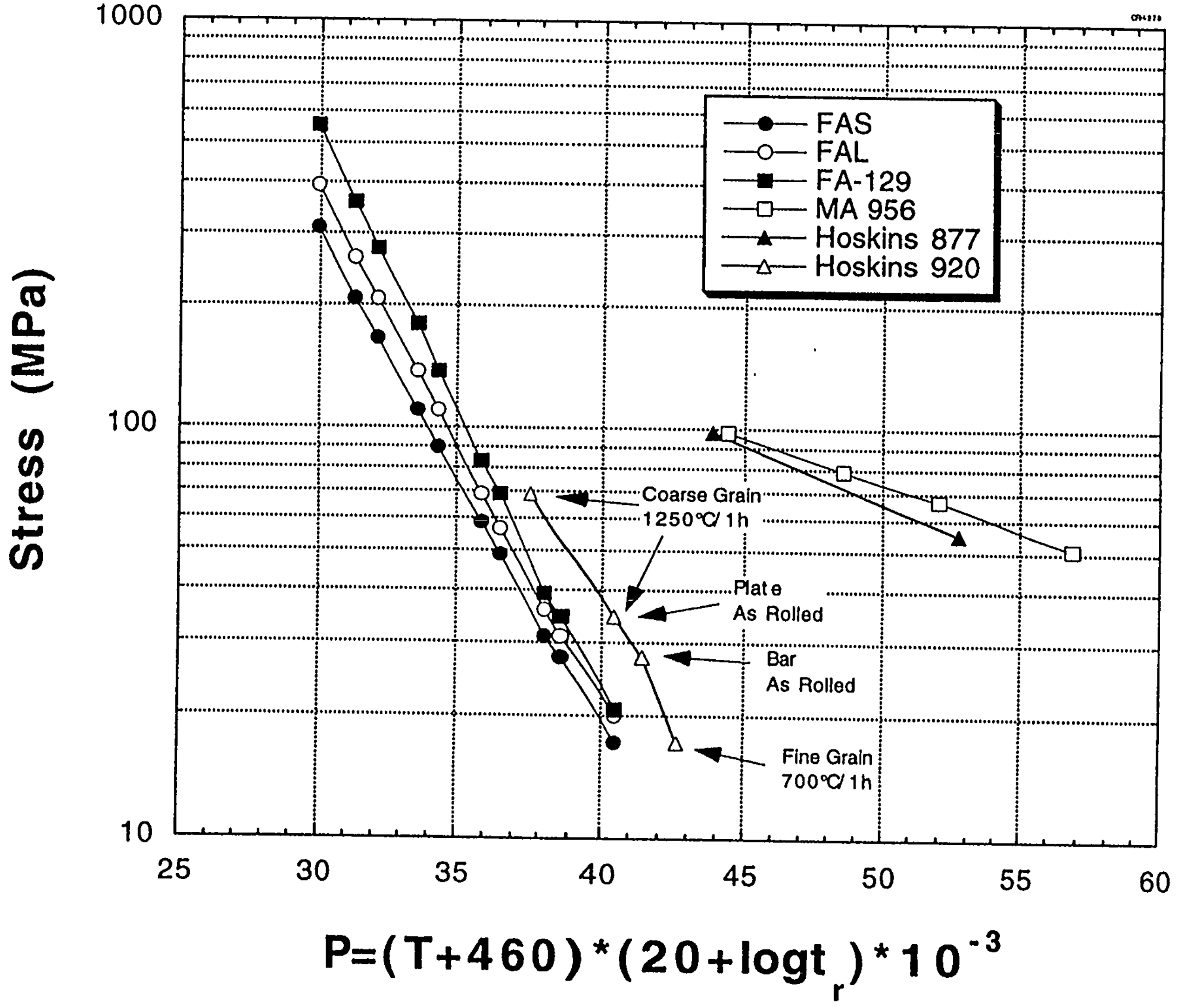

Figure 5. Larson Miller plot of creep rupture data for sheet, plate, and bar of 920 alloy.

Table 3. Creep property data for 920 alloy (heat 21870) of FAS + 0.5 wt % Y_2O_3

Specimen no.	Heat treatment	Test temperature (°C)	Stress (MPa)	Status[a]	Time (h)	Total elongation (%)	Reduction of area (%)
1L	Sheet Annealed 700°C/1 h OQ[b]	980	69	R	0.0	3.72	83.30
3L	Sheet Annealed 700°C/1 h OQ[b]	800	17	R	113.8	3.53	29.20
7L	Sheet Annealed 1250°C/1 h Vacuum	800	35	R	11.7	62.50	61.50
12L	Sheet Annealed 1250°C/1 h Vacuum	700	69	R	29.9	71.40	63.97
13L	Plate As rolled	800	35	R	6.0	126.37	85.33
21L	Bar As rolled	800	28	R	27.5	99.76	86.88

[a] R = ruptured.

[b] OQ = oil quenched.

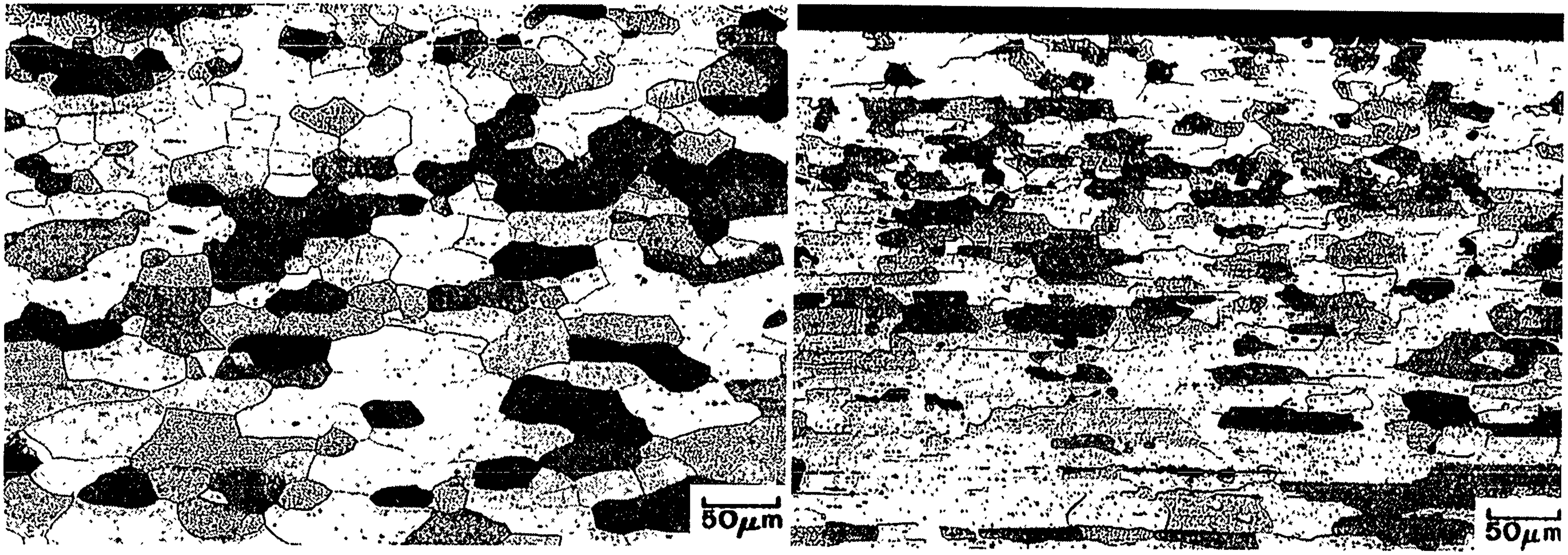

(*a*) 97-0524-10

(*b*) 97-0700-2

Figure 6. Optical microstructure of the longitudinal section of a 0.76-mm-thick sheet of ingot metallurgy oxide dispersion strengthened FAS alloy: (*a*) air annealed for 1 h at 700°C followed by oil quenching, and (*b*) vacuum annealed for 1 h at 1250°C. The magnification for both (*a*) and (*b*) is 200×.

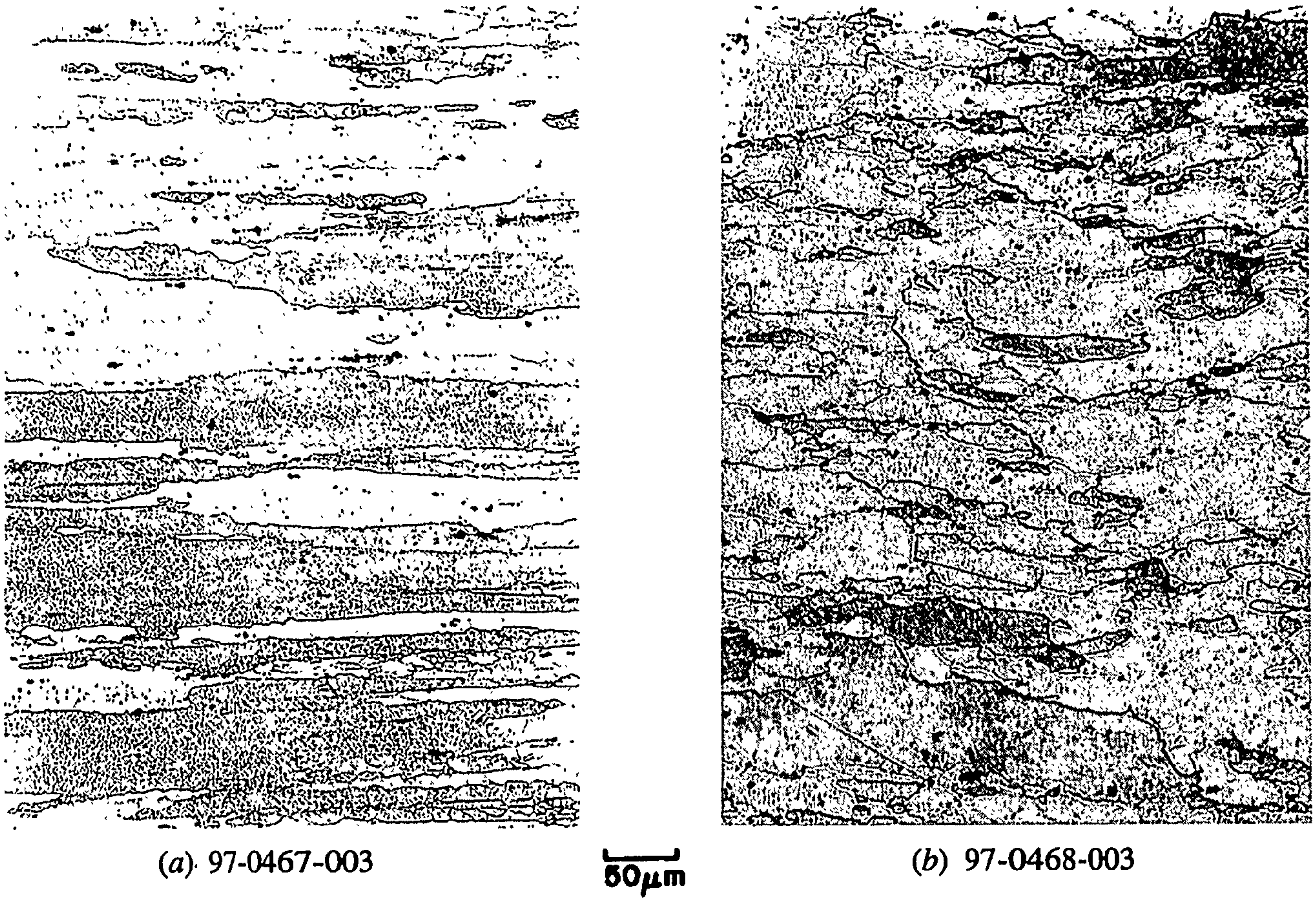

(*a*) 97-0467-003

(*b*) 97-0468-003

Figure 7. Optical micrographs of etched 15.9-mm-thick plate of ingot metallurgy oxide dispersion strengthened FAS alloy: (*a*) longitudinal and (*b*) transverse. The magnification for both (*a*) and (*b*) is 200×.

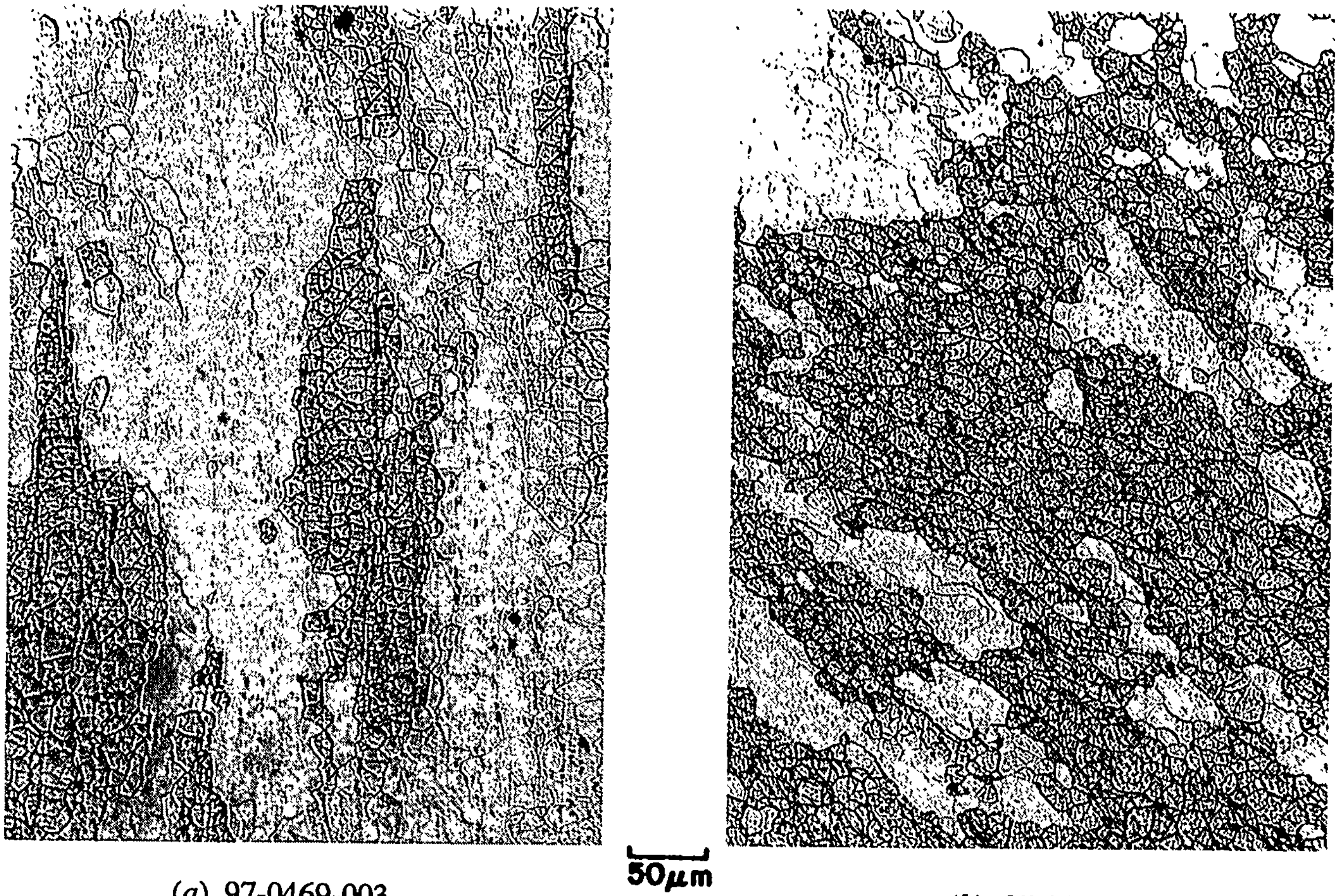

(*a*) 97-0469-003

(*b*) 97-0470-003

Figure 8. Optical micrographs of etched 60.3 mm rounded corner bar of ingot metallurgy oxide dispersion strengthened FAS alloy: (*a*) longitudinal and (*b*) transverse. The magnification for both (*a*) and (*b*) is 200×.

The optical microstructures of the sheet in the fine- and coarse-grained heat-treated conditions are shown in Figure 6. The microstructures of the plate and bar are shown in Figures 7 and 8. The sheet and plate show elongated grains in the rolling direction, and the microstructure is uniform across the thickness. The bar showed a inhomogeneous microstructure that consisted of large grains and large grains with colonies of fine grains, which may have resulted from the dynamic recrystallization process.

The backscattered electron micrographs of transverse sections of the plate and bar are shown in Figure 9. The low magnification micrographs show a fairly uniform distribution of Y_2O_3 particles. The higher magnification micrographs show the Y_2O_3 particles to be clusters. The porosity observed in the high magnification micrographs is a result of Y_2O_3 particle drop-out during metallographic specimen preparation.

Elemental mapping was carried out on one of the large particle areas to determine their composition (Figure 10). It is clear from these maps that the large particles consist of yttrium and oxygen and have no iron or aluminum associated with them.

DISCUSSION

The ingot metallurgy method for ODS, developed by Hoskins, has worked effectively for creep strengthening of their Fe-Cr-Al alloy. However, the same method when applied to the ORNL-developed Fe_3Al-based alloy FAS showed less benefit in improvement of creep strength. Detailed metallography has revealed that the primary cause for less improvement in the FAS material is the presence of Y_2O_3 agglomerates rather than the finer distribution that is required for strengthening. Even though the full property enhancement was not observed, the Y_2O_3-treated FAS alloy still showed nearly two times higher creep rupture strength values than the untreated material. The Y_2O_3-treated alloy also showed nearly a factor of two higher yield and ultimate tensile strengths at temperatures $\geq 600°C$. A second heat of the alloy is planned to check if Y_2O_3 distribution can be refined to produce a finer uniform distribution.

The sheet produced by rolling the plate was used to determine if grain growth treatment resulted in further improvement of creep strength. Metallography of the sheet specimens with 700 and 1250°C treatments showed that the later treatment did not produce a significant increase in grain size. Work is currently under way to look at heat-treatment temperatures of 1350 and 1400°C for 1 h. The specimens heated for grain growth will be subjected to creep testing to determine the resulting strength improvement.

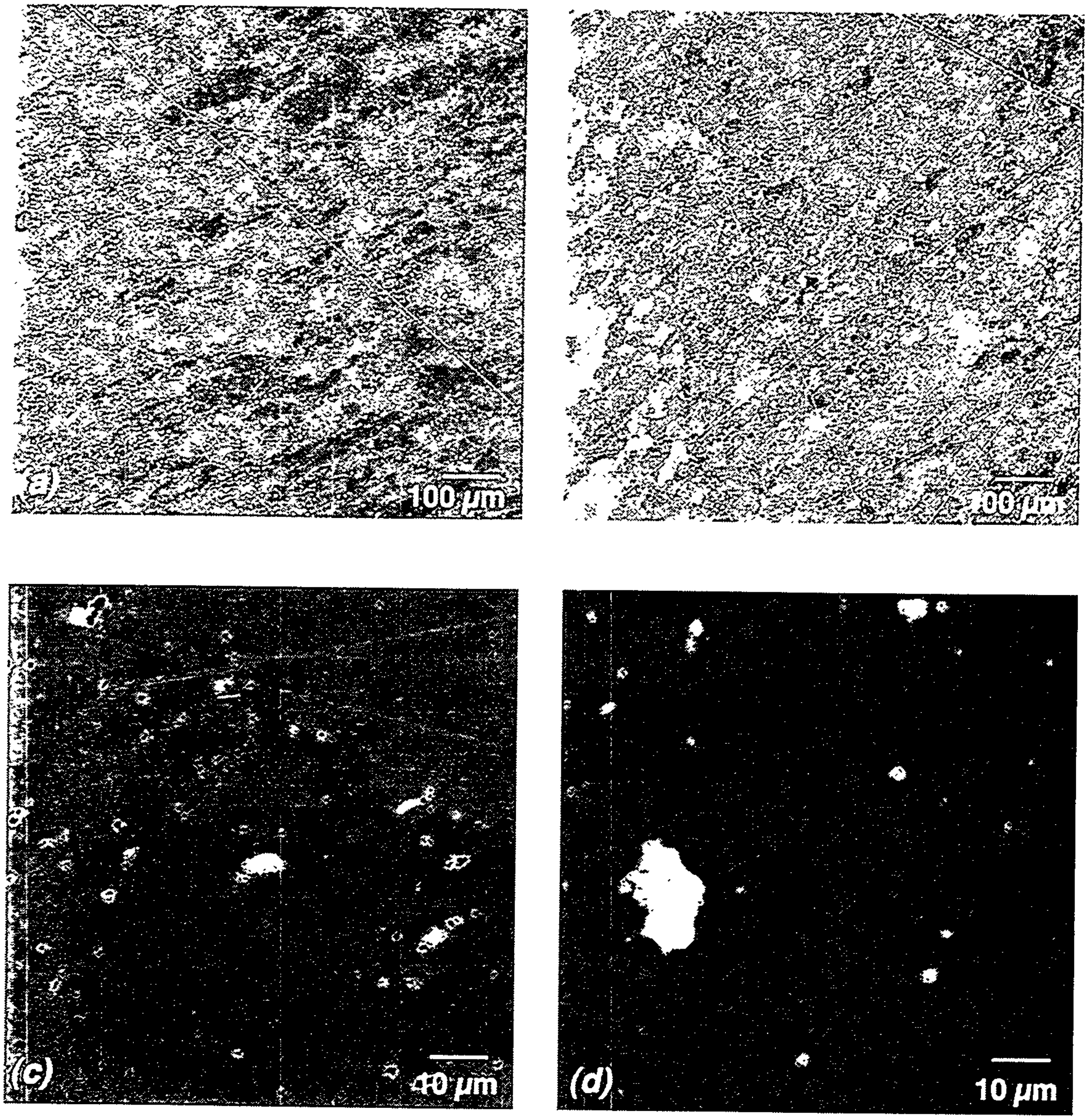

Figure 9. Scanning electron micrographs of transverse sections of plate and bar products of ingot metallurgy oxide dispersion strengthened FAS alloy: (*a*) plate and (*b*) bar are low magnification, and (*c*) plate and (*d*) bar are high magnification.

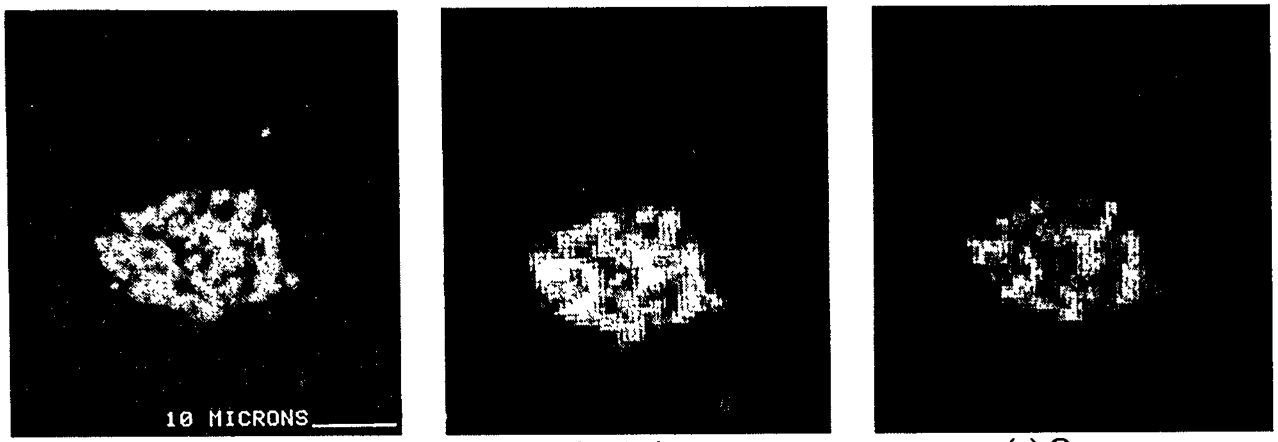

(*a*) Backscattered electron image (*b*) Yttrium (*c*) Oxygen

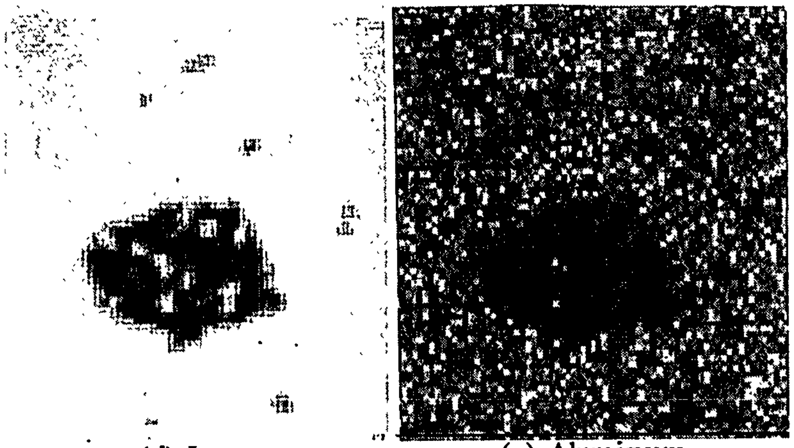

(*d*) Iron (*e*) Aluminum

Figure 10. Scanning electron micrographs showing: (*a*) backscattered electron image of the particles in ingot metallurgy oxide dispersion strengthened FAS. Elemental maps of yttrium, oxygen, iron and aluminum are shown in (*b*), (*c*), (*d*), and (*e*), respectively.

SUMMARY AND CONCLUSIONS

A lower cost method developed by Hoskins was used to produce an ODS heat of Fe_3Al-based alloy FAS. The alloy contained 0.5% Y_2O_3 and was processed into plate, bar, and sheet. Tensile, creep, and metallography were carried out on all three products. To date, data have shown only moderate improvement in creep properties as opposed to Y_2O_3-free material. It is also shown that the Hoskins process works for a Fe-Cr-Al alloy (877). It is believed that Y_2O_3 particle clusters are the cause for limited improvement observed in creep properties. A second heat of FAS is being planned by Hoskins' method.

ACKNOWLEDGMENTS

The authors thank Dave Harper and Ken Blakely for cutting and processing the ingots, Hu Longmire for optical metallogjraphy, Larry Walker for scanning electron microscopy work, and Millie Atchley for preparing the manuscript.

Research for this work was sponsored by the U.S. Department of Energy, Office of Fossil Energy, Advanced Research and Technology Development Materials Program [DOE/FE AA 15 10 10 0, Work Breakdown Structure Element ORNL-2(H)], under contract DE-AC05-96OR22464 with Lockheed Martin Energy Research Corp.

REFERENCES

1. C. G. McKamey, J. H. DeVan, P. F. Tortorelli, and V. K. Sikka, *J. Mater. Res.*, **6**, 1779-805 (1991).
2. V. K. Sikka, S. Viswanathan, and S. Vyas, *High Temperature Ordered Intermetallic Alloys V*, Vol. 288, p. 971, Materials Research Society, Pittsburgh, Pennsylvania, 1993.
3. V. K. Sikka, S. Viswanathan, and C. G. McKamey, *Structural Intermetallics*, p. 483, The Minerals, Metals and Materials Society, Warrendale, Pennsylvania, 1993.
4. C. G. McKamey and D. H. Pierce, *Scr. Metall. Mater.*, **28**, 1173-6 (1993).
5. P. G. Sanders, V. K. Sikka, C. R. Howell, and R. H. Baldwin, *Scr. Metall. Mater.*, **25**, 2365-9 (1991).
6. K. Natesan and P. F. Tortorelli, *International Symposium on Nickel and Iron Aluminides: Processing, Properties, and Applications*, p. 265, ASM International, Materials Park, Ohio, 1997.

SIMULTANEOUS ALUMINIZING and CHROMIZING of STEELS to FORM $(Fe,Cr)_3Al$ COATINGS and Ge-DOPED SILICIDE COATINGS of Cr-Zr BASE ALLOYS

Minhui Zheng, Yi-Rong He and Robert A. Rapp

Department of Materials Science and Engineering
The Ohio State University
Columbus, Ohio 43210 (U.S.A.)

A halide-activated cementation pack involving elemental Al and Cr powders has been used to achieve surface compositions of approximately Fe_3Al plus several percent Cr for low alloy steels (T11, T2 and T22) and medium carbon steel (1045 steel). A two-step treatment at 925°C and 1150°C yields the codeposition and diffusion of aluminum and chromium to form dense and uniform ferrite coatings of about 400μm thickness, while preventing the formation of a blocking chromium carbide at the substrate surfaces. Upon cyclic oxidation in air at 700°C, the coated steel exhibits a negligible 0.085 mg/cm^2 weight gain for 1900 one-hour cycles. Virtually no attack was observed on coated steels tested at ABB in simulated boiler atmospheres at 500°C for 500 hours. But coatings with a surface composition of only 8 wt % Al and 6 wt% Cr suffered some sulfidation attack in simulated boiler atmospheres at temperatures higher than 500°C for 1000 hours.

Two developmental Cr-Zr based Laves phase alloys (CN129-2 and CN117(Z)) were silicide/germanide coated. The cross-sections of the Ge-doped silicide coatings closely mimicked the microstructure of the substrate alloys. Cyclic oxidation in air at 1100°C showed that the Ge-doped silicide coating greatly improved the oxidation resistance of the Cr-Zr based alloys.

INTRODUCTION

Recent papers, e.g. by DeVan et al.[1,2] show that the alloy compositions based on Fe_3Al are very resistant to sulfidation and oxidation at high temperatures, but that a low Cr content is also required to provide resistance to room temperature aqueous corrosion (leading to hydrogen embrittlement) and resistance to high temperature hot corrosion by fused salt deposits, e. g. coal fly ash. Natesan and Johnson[3] reported that a threshold Al content in excess of 10 wt% is needed in Fe-Al alloys for adequate corrosion resistance in sulfur-containing atmospheres, while the Cr content in the alloy played a critical role for corrosion resistance in HCl-containing environments.

Geib and Rapp[4,5] and Miller et al.[6] codeposited Cr-Al diffusion coatings on low-alloy steels and stainless steels, respectively, using a 85Cr-15Al masteralloy powder as a pack component. The surface composition sought by those studies was Fe-20Cr-4.5Al. That process specified the use of a Cr-Al masteralloy powder which is expensive and probably cannot be recycled or rejuvenated. A preferred pack cementation process would use a mixture of pure elemental powders, which are less expensive than masteralloy powders, and would incorporate a thermal processing schedule that would not impair the strength of the metal. The current study describes a pack cementation process which develops an Al-Cr coating on carbon-containing steels by a two-step temperature program. To avoid the formation of a chromium carbide blocking layer, the steel substrate is aluminized first at a lower temperature and then is chromized at a higher temperature. In this regard, the process is similar to that for codepositing Cr and Si diffusion coatings onto steels.[7,8]

The demand for higher strength and high service temperatures of structural materials had led to the consideration of Laves phase-based alloys.[9,10] A Laves phase compound with the AB_2 stoichiometry shows either the hexagonal C14 structure, the cubic C15 structure, or the hexagonal C36 structure. The complex crystal structures of the Laves phase make the compound inherently strong but brittle. In binary refractory-metal chromium systems such Cr-Ti, Cr-Zr, Cr-Hf, Cr-Nb and Cr-Ta, these Laves phases are in equilibrium with Cr via eutectic reactions. For the Cr-Zr binary system, the eutectic temperature is about 1630°C; the melting point of Cr_2Zr is about 1675°C. The Laves phase Cr_2Zr undergoes a polymorphic transformation from a low-temperature C14 structure to the high-temperature C15 structure at about 1000°C.[11]

Recently, two Cr-Zr based alloys (CN117(Z) and CN129-2) have been prepared and studied at Oak Ridge National Laboratory(ORNL) as possible advanced high-temperature structural materials. Preliminary isothermal oxidation tests at 950°C and 1100°C at ORNL show that the alloys exhibit only fair to poor isothermal oxidation resistance. Also, the CN129-2 alloy catastrophically failed a 6 cycle, 120 hour screening test at 1100°C. These results indicate the need for a protective coating of the alloys for high temperature applications. A previous study at OSU showed that a Ge-doped silicide coating can protect Cr-Nb based alloys from significant oxidation and from pesting under cyclic and isothermal oxidation conditions.[12] Therefore, the goal of this research is to develop a Ge-doped silicide coating on the Cr-Zr based alloys by the pack cementation technique, to characterize the coating, and to test its oxidation resistance.

THERMODYNAMIC CONSIDERATIONS

To understand the chemical reactions taking place during the pack cementation process, the equilibrium vapor pressures of the halides generated by the pack powder mixtures at 1200K and 1400K were calculated using the PC-compatible STEPSOL computer program modified by Morris et al. from the ITSOL program.[13,14] The program calculates the equilibrium vapor pressures in the pack by minimizing the Gibbs energy of the system. In fact, the activity of Al and the AlCl vapor pressure must drop during the deposition process, not only because of Al uptake by the substrate, but especially due to alloying of Al with the Cr powder. The dominant deposition species are AlCl and $CrCl_2$. For a fluoride-activated pack, the effective deposition species is AlF, and the partial pressures for the Cr fluorides are too low for Cr deposition, so a chloride activator is always needed to chromize. Kung and Rapp[15] presented such calculations for coatings involving a single component. He, Wang and Rapp[16] examined the use of various mixed activator salts for Cr-Si codeposition.

The deposition and diffusion of Cr into a steel which contains carbon is often limited by the formation of chromium carbide. Menzies and Mortimer[17] classified the coating structures into two groups: those for steels with carbon contents below 0.2 wt% C, which exhibited carbide formation along grain boundaries and as precipitates within the grains of the ferritic coating, and steels containing more than 0.2 wt% C, which usually formed a continuous chromium carbide layer at the surface of the coating. Since the solubility of Al in austenite is restricted to a low wt%, introducing Al into a steel substrate produces a ferrite layer with very low carbon solubility at the surface. Therefore carbon is rejected into the austenite core. This process is illustrated schematically in Fig.1. After forming a low-carbon Al-rich ferrite case at a low temperature, the codeposition of Cr becomes possible at a higher temperature, especially because the Al powder has been depleted upon alloying with the Cr powder and the substrate.

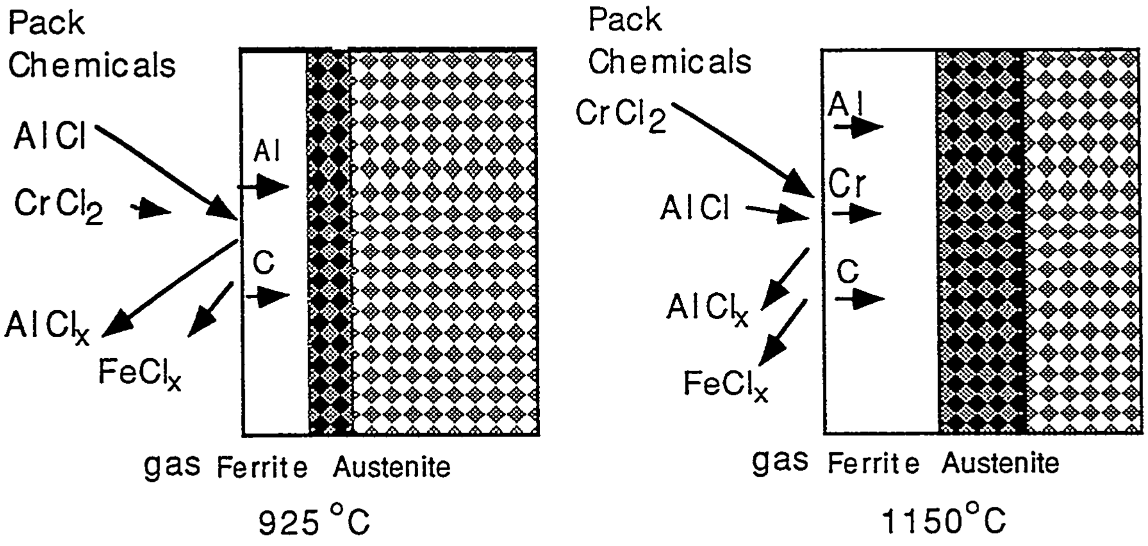

Fig. 1 Schematic of two-step pack cementation coating process. Longer arrows correspond to higher vapor pressures. The darkened area represents a zone of carbon enrichment in austenite. Microstructure of T11 steel coated in pack with 2Al-18Cr, $2CrCl_2$ at 925°C for 4 hours then at 1150°C for 3 hours.

From the STEPSOL program, the thermodynamic equilibria in the Cr-Al system containing various halide activators have been calculated. The presence of $CrCl_2$ is too low for significant transport at 1200K, but is much higher at 1400K. All chloride activators and their combinations generate higher AlCl vapor pressure and much lower vapor pressures for $CrCl_2$. Thus, a steel substrate will be aluminized preferentially at 1200K. Then upon raising the temperature to about 1400K, the substrate can gain chromium delivered by the $CrCl_2(g)$ species.

EXPERIMENTAL PROCEDURES

Coupons of T11 steel with composition Fe-1Cr-0.5Mo-0.15C or T2 steel with composition Fe-0.5Cr-0.5Mo-0.15C were cut from tubes or plates. The surface areas were about 1.5 cm^{2}. These coupons were ground through 600 grit SiC paper, cleaned, dried and weighed. The coupons were placed in an alumina crucible in contact with a mixed powder containing elemental Al and Cr powders, a chloride activator salt(s) and an inert alumina filler powder plus 2wt% cerium oxide. The alumina crucible was closed with an alumina lid using an alumina-base cement and then placed in a horizontal electric furnace purged with prepurified Ar. The furnace was heated to a desired temperature (±5°C) and held for the prescribed duration; for the current experimentation, an isothermal hold at 925°C for several hours was followed by a further hold at 1150°C. After cooling in the furnace, the crucible was opened and the coated substrates were cleaned and reweighed. The surface phase was identified with X-ray diffraction (XRD) using a SCINTAG diffractometer. An optical microscope was used to observe and photograph the coating cross-section. A scanning electron microscope (SEM) with an energy dispersive X-ray spectrometer (EDS) was used to determine the concentration profiles across the coating cross-section. Some coating compositions were also analyzed with a wave length dispersive X-ray spectrometer (WDS) to verify the reliability of the composition analyses.

Alloys of CN117(Z) and CN129-2 were used as the substrates. These alloys contain approximately 5-8 at.% Zr, and minor alloying additions of several other elements at concentrations less than 5 at.%. The EDM sliced CN117(Z) and CN129-2 alloys were prepared to a 600 grit finish. The as-cast CN129-2 coupons contained cracks. The cementation pack consisted of pure elemental powders of Si and Ge, NaF activator and Al_2O_3 inert filler. The detailed procedure for pack cementation was described in the previous study.[12] A 1-h cycle in air at 1100°C consisting of 45 min heated and 15 min cooled was used for cyclic oxidation study.

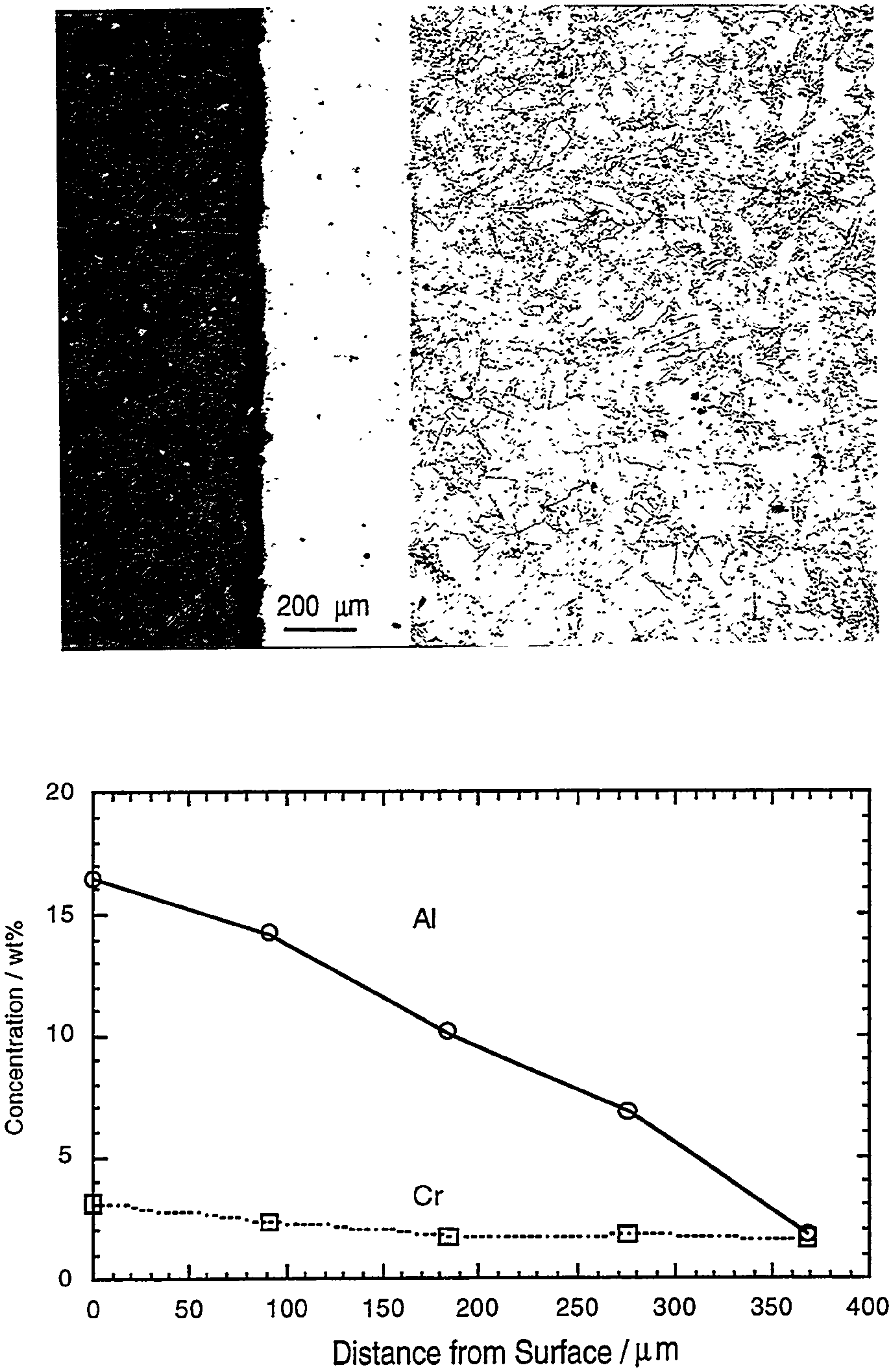

Fig. 2 Coating microstructure and EDS composition profile for T11 steel sample (NH_4F and $MgCl_2$ dual activators, heating sequence: 925°C for 8 hours, then at 1150°C for 4 hours).

RESULTS AND DISCUSSION

For the T11 steel samples, the phase transformation from ferrite to austenite occurs at about 888°C. Preliminary coating tests showed that at a temperature lower than about 920°C most T11 substrates lost weight by $FeCl_2$ evaporation and formed a porous coating. Thus, the temperature for the first-step treatment was set at 925°C. Other prior coating tests showed that a one-step treatment at 1150 °C resulted in chromium carbide layers on the substrates, accompanied by decarburization.

Figure 2 presents a representative coating microstructure and the corresponding composition profile for a T11 steel sample. A dual activator of 1 wt% NH_4F and 2 wt% $MgCl_2$ were used with Al_2O_3 plus 2 wt% CeO_2 as the filler. A two-step heating schedule consisted of 925°C for 8 hours followed by 4 hours at 1150°C. A dense ferrite layer of about 400μm thickness was formed, and the inward diffusion of carbon insured the absence of any denuded zone of decarburiztion. The surface composition was about 16 wt% Al, 3 wt% Cr. For all of the coatings produced in this work, the compositions at the external surface ranged from 13-17 wt% Al and 3-6 wt% Cr. Stoichiometric Fe_3Al has 13.8 wt% Al. Upon rather slow cooling from the 1150°C coating temperature, the ferrite grains of the coating grow inward to eliminate the coating/core interface which existed at the high temperature. Thus, the ferrite grains of the coating extend into the prior austenite core of the substrate, providing an excellent bond of the coating to the substrate. Indeed, after cooling, no interphase interface exists, only a discontinuity in the composition.

Table 1 presents the coating characteristics for some example packs with a mixture of elemental Al and Cr powders using single or dual activators and similar heating schedules. The surface compositions were consistently around 12-17 wt% Al and 6-3 wt% Cr. The cementation packs using NH_4Cl or NH_4F generally resulted in slightly higher aluminum content in the coatings. Although thermodynamic calculations indicate that CeO_2 can be partially reacted to form $CeCl_3$ (v), no Ce has been detected by EDS or WDS in the coatings produced using packs containing CeO_2 powder. Apparently the amount of Ce deposited into the coating was too small to be detected by the mentioned methods.

OXIDATION/CORROSION TESTING OF $(Fe, Cr)_3Al$ COATED STEELS

A coated T11 coupon, with surface composition of 15.9 wt% Al and 2.8 wt% Cr was tested in cyclic oxidation in air at 700°C for 1900 one-hour cycles, and a quite negligible weight gain of 0.085 mg/cm^2 was recorded, with an absence of scale spallation. Therefore, this coating composition forms a very adherent, very slow growing alumina scale in air oxidation.

Table 1 Contents of Example Cementation Packs and the Resulting Surface Concentrations of Diffusion Coatings.

Substrate Steels	Activator (wt%)	Metal Source (wt%)	Surface Comp. (wt%)	Coating Depth (μm)
T11	$1NH_4F-2MgCl_2$	2Al-18Cr	16.5Al-3.1Cr	400
T2	$1NH_4Cl-1.5MgCl_2$	2Al-18Cr	13.2Al-5.6Cr	440
T11	$1NH_4Cl-1.5MgCl_2$	2Al-18Cr	16.3Al-4.3Cr	400
T11	$2MgCl_2$	2Al-18Cr	12.4Al-3.8Cr	420
1045	$1NH_4Cl-1.5MgCl_2$	3.5Al-17Cr	18.9Al-2.8Cr	580

Table 2 ABB Corrosion Test Environments.

Oxidizing Gas				Reducing Gas			
1000 ppm	SO_2	2.44 %	H_2	1000 ppm	H_2S	2 %	H_2
12.3 %	CO_2	0.68 %	O_2	7 %	CO_2	N_2	balanced
8.6%	CO	N_2	balanced	13%	CO	(embedded in mid-western bituminous coal, 3.5 % S)	

Similarly coated T11 steel samples, with a surface composition of 12.4 wt% and 2.8 wt% Cr, were tested under oxidizing and reducing conditions of a low NO_X coal combustion environment at 500°C for a period of 500 hours at the ABB Power Plant Labs in Windsor, CT; and the gas compositions used for these tests are listed in Table 2.

Weight change measurements and microstructural observations showed that the Al-Cr coatings were virtually unattacked after 500 hour exposures to either the reducing or oxidizing testing conditions at 500°C. Some coatings with only 8 wt% Al and 6 wt% Cr at the surfaces were also tested at ABB in atmospheres containing higher hydrogen sulfide contents for longer times and the coatings showed attack. No preferential corrosion along grain boundaries was observed. The results show that the coatings with aluminum contents lower than that of Fe_3Al but with an increased amount of Cr are less resistant to sulfidation.

X-ray diffraction analysis of the coupon surface revealed only the $CrSi_2$ phase for both coated alloys. Figure 3(a) shows the surface morphology of a CN117(Z) alloy coated at 1050°C for 12 hours in a pack containing 12Si-12Ge (wt.%). EDS analysis showed the flat area (spot A) was composed of 71Si, 28Cr and 1Ge (at.%), indicating the formation of $Cr(Si,Ge)_2$. The nodule phase (spot B) consisted of 47O, 19Si, 17Al, 10Na, 7F, i.e., a residue from the pack coating process. Figure 3(b) presents the cross-section of Fig. 3(a). EDS results show that the dark phase has the composition of 29Cr, 1X1, 68Si, 1Ge, suggesting the formation of $(Cr,X1)(Si,Ge)_2$. The bright phase is composed of 34Cr, 2X2, 15Zr, 44Si, 5Ge, indicating the existence of (Cr,Zr,X2)(Si,Ge) monosilicide. The gray phase, which formed adjacent to the coating/substrate interface, consists of 53Cr, 1X2, 3X1, 41Si and 2Ge, i.e., $(Cr,X1,X2)_3(SiGe)_2$. Figure 4 shows the cross-section of a coated CN129-2 alloy using the same treatment. EDS analyses again revealed the formation of $(Cr,X1)(Si,Ge)_2$, $(Cr,Zr,X2)(Si,Ge)$ and $(Cr,X1,X2)_3(Si,Ge)_2$ in the coating. X1 and X2 represent proprietary alloying elements added in the Cr-Zr based alloys.

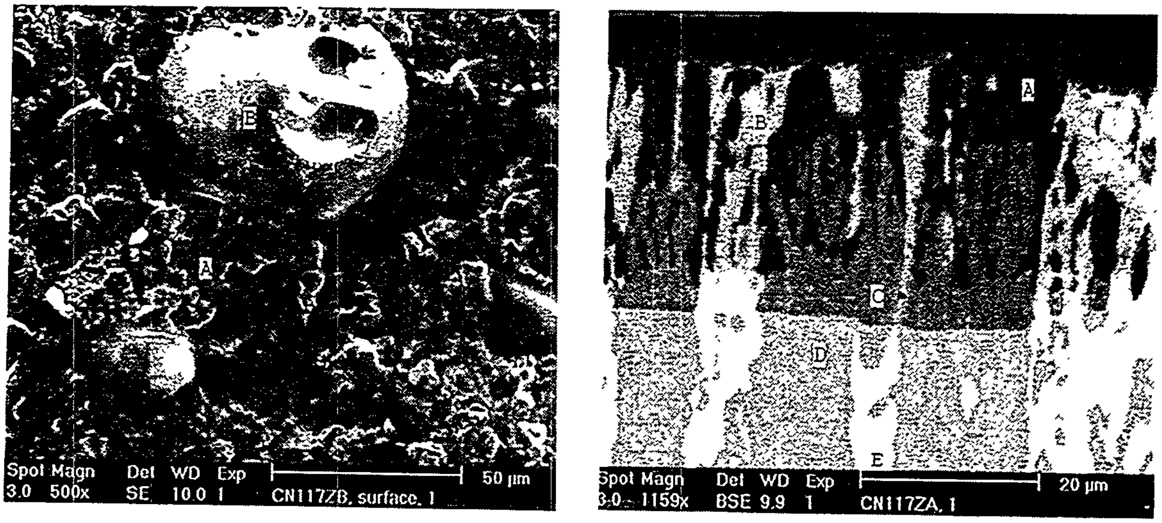

(a) (b)

Fig. 3(a) Surface morphology, 3(b) Cross-section of a CN117(Z) alloy coated at 1050°C for 12 hours in a pack containing 12Si-12Ge (wt.%)

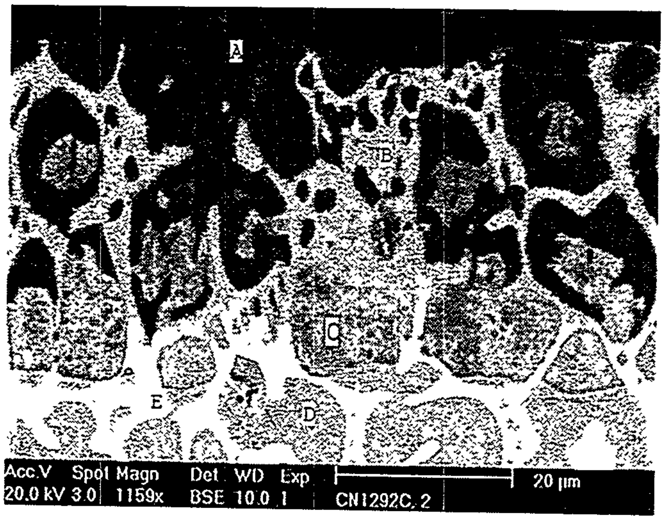

Figure 4 Cross-section of a CN129-2 alloy coated at 1050°C for 12 hours in a pack containing 12Si-12Ge (wt.%)

In each case, the microstructure of the coatings closely mimics the microstructure of the alloys, without any voids in the coating. Thus, the growth of the coating occurred the inward diffusion of Si and Ge. But the Ge content was not uniformly distributed among the three phases in the coating; the highest Ge concentration was found in the (Cr,Zr,X2)(Si,Ge) monosilicide phase. This is in consistent with the findings of previous study on Cr-Nb based alloys.[12]

Fissures were observed in the Ge-doped silicide coating on both alloys. These are generally the most significant defects in silicide coatings.[18] Because the silicides have a higher thermal expansion coefficient than the substrate, the thermal mismatch produces tension in the adherent coating upon cooling, which results in the inherent fissures. Then, for effective protection from oxidation, the coating must form oxides with sufficient fluidity to flow into fissures and exhibit a self-healing capability. The studies by Fitzer et al.[19] and Schlichting and Neumann[20] show that GeO_2 solute in a protective silica scale formed upon oxidation increases its fluidity and thermal expansion coefficient. Therefore the addition of Ge in the silicide coating is expected to help the healing of these fissures during isothermal and cyclic oxidation.

The cyclic oxidation studies underway at 1100°C already show the effectiveness of the Ge-doped silicide coatings in protection of CN117(Z) and CN129-2 alloys from significant oxidation. After 11 cycles, the average weight gains for the uncoated and coated CN117(Z) coupons are 8.9 and 1.5 mg/cm^2, respectively. The average weight gains for the uncoated and coated CN129-2 coupons are 12.5 and 1.6 mg/cm^2, respectively. These results clearly demonstrated that the Ge-doped silicide coating can greatly improve the cyclic oxidation resistance of the Cr-Zr based alloys, even when there are cracks in the substrate or coating.

CONCLUSIONS

A single-step halide-activated Cr-Al pack cementation process at 1150°C for low alloy steels produces a blocking chromium carbide layer and decarburization at the surface. A two-step process involving a first treatment at 925°C and a second at 1150°C results in a dense ferrite coating of composition $(Fe, Cr)_3Al$ which is very oxidation and corrosion resistant under both oxidizing and sulfidizing conditions. The reproducibilities of the composition and thickness of the coatings have been demonstrated.

Two Cr-Zr based Laves phase alloys were silicide/germanide coated using pack cementation technique. The microstructure of the Ge-doped silicide coatings closely mimicked the microstructure of the substrate alloys. Cyclic oxidation in air at 1100°C showed that the Ge-doped silicide coating greatly improved the oxidation resistance of the Cr-Zr based alloys.

ACKNOWLEDGMENTS

The authors wish to acknowledge the financial support from DOE, Oak Ridge National Laboratory (R. R. Judkins, project monitor), contract FWP-FEAA028. The earlier studies by Ge Wang led to the prospect for the aluminizing-chromizing process reported here. The oxidation testing in simulated combustion gas atmospheres was conducted by Juan Nava Paz of ABB Power Plant Labs.

REFERENCES

1. J. H. DeVan, *Oxidation of High-Temperature Intermetallics* (T. Grobstein and J.Doychak, Eds.), (1989), p.107.
2. P. F. Tortorelli, G. M. Goodwin, M. Howell, and J. H. DeVan, *Heat-Resistant Materials II* (K. Natesan, P. Ganesan and G. Lai, Eds.), ASM Intern., Materials Park, OH, (1995), p.585.
3. K. Natesan and R.N. Johnson, *Heat-Resistant Materials II* (K. Natesan, P.Ganesan and G. Lai, Eds.), ASM Intern., Materials Park, OH, (1995), p.591.
4. F. D. Geib and R.A. Rapp, *Processing and Manufacturing of Advanced Materials for High Temperature Applications* (V.A. Ravi, and T.S. Srivastan, Eds.) TMS, Warrendale, PA, (1991), p. 347.
5. F. D. Geib and R.A. Rapp, *Oxid. Metals*, 40, 213 (1993).
6. D. M. Miller, S. C. Kung, S. D. Scarberry and R.A. Rapp, *Oxid. Metals*, 29, 239 (1988).
7. R. A. Rapp and M. A. Harper, U. S. Patent No. 5,364,659, Nov. 1994.
8. R. A. Rapp, G. Wang and E. Pangestuti, U.S. Patent No. 5,492,727, Feb. 1996, and 5,589,220, Dec. 1996.
9. G. Sauthoff, *Z. Metallkde*, 79 (1988), 337.
10. K. S. Kumar and C. T. Liu, *JOM*, (1993), 28.
11. M. Hansen, K. Anderko, *Constitution of Binary Alloys*, Metallurgy and Metallurgical Engineering Series, McGraw-Hill Book Co., (1958), 573.
12. Y-R. He, R. A. Rapp and P. F. Tortorelli, *Materials Science and Engineering*, 222A (1997), 109
13. H. Flynn, A.E. Morris and D. Carter, Version 4.0, Released February, 1990.
14. H. Flynn, A.E. Morris and D. Carter, *Proc. of 25th Conference of Metallurgists*, TMS-CIM, Toronto, Ontario, 1996.
15. S-C Kung and R.A. Rapp, *Oxid. Metals*, **32**, 89 (1989).
16. N. He, G. Wang and R.A. Rapp, *High Temp. Materials Science*, **34**, 117 (1995).
17. I. A. Menzies and D.Mortimer, *Corr. Sci.*, **5**, 539 (1965).
18. C. M. Packer, *Oxidation of High-Temperature Intermetallics*, T. Grobstein and J. Doychak (eds.), TMS, (1988), 235.
19. E. Fitzer, H. Herbst and J. Schlichting, *Werkst. Korros.*, 24 (1973), 274.
20. J. Schlichting and S. Neumann, *J. Non-Cryst. Solids*, 48 (1982), 185.